University of California
Los Angeles

Injection of Tunnel Ionized Electrons into Laser-Produced Wakes

A dissertation submitted in partial satisfaction
of the requirements for the degree
Doctor of Philosophy in Electrical Engineering

by

Arthur Pak

2010

The dissertation of Arthur Pak is approved.

Warren Mori

Pietro Musumeci

Chris Neimann

Chandrashekhar Joshi, Committee Chair

University of California, Los Angeles

2010

To Julie, I couldn't have done it without you.

To my parents Ed and Raylene, your encouragement and support gave me this opportunity and made all of this possible.

Table of Contents

List of Figures

List of Tables

Acknowledgments

I would like to thank Ken Marsh for the incredible amount of time and effort that he spent helping me perform this work and for teaching me almost everything I know about working in a lab. I would also like to thank Sam Martins and Joana Martins for running many simulations for me. Thank you Wei Lu and Warren Mori for all of the insight that you both provided into the physics and theory of this work. Finally I would like to thank my advisor Chan Joshi, for all of his support, guidance and for all he has taught me throughout the years.

Vita

1982	Born, Los Altos, California, USA.
2004	B.S. (Optical Science Engineering), University of California Davis, Davis, California
2006	M.S. (Electrical Engineering), University of California Los Angeles, Los Angeles, California.
2004-2010	Graduate student researcher at UCLA, department of electrical engineering.

Publications

A. Pak, K. A. Marsh, S. F. Martins, W. Lu, W. B. Mori, and C. Joshi
Injection and trapping of tunnel-ionized electrons into laser-produced wakes, Physical Review Letters,**10**,025003(2010)

C.E. Clayton, J.E. Ralph, F. Albert, R.A. Fonseca, S.H. Glenzer, C. Joshi, W. Lu, K. A. Marsh, S.F. Martins, W.B. Mori, A. Pak, F.S. Tsung, B.B. Pollock, J.S. Ross, L.O. Silva, and D.H. Froula
Self-guided laser wakefield acceleration beyond 1 Gev using ionization-induced injection, Accepted to Physical Review Letters,(2010)

J. E. Ralph, C. E. Clayton, F. Albert, B. B. Pollock, S. F. Martins, A. E. Pak, K. A. Marsh, J. L. Shaw, A. Till, J. P. Palastro, W. Lu, S. H. Glenzer, L. O.

Silva, W. B. Mori, C. Joshi, and D. H. Froula,
Laser Wakefield acceleration at reduced density in the self-guided regime,
Physics of Plasmas,**17**,056709(2010)

D. H. Froula, C. E. Clayton, T. Döppner, K. A. Marsh, C. P. J. Barty, L. Divol1, R. A. Fonseca, S. H. Glenzer, C. Joshi, W. Lu, S. F. Martins, P. Michel, W. B. Mori, J. P. Palastro, B. B. Pollock, A. Pak, J. E. Ralph1, J. S. Ross, C. W. Siders, L. O. Silva, and T. Wang
Measurements of the critical power for self-injection of electrons in a laser wakefield, Physical Review Letters,**103**,215006(2009)

A.E. Pak, C. Joshi, K.A. Marsh, S. Martins, W.B. Mori
Investigation of ionization induced trapping in a laser wakefield accelerator, PAC conference proceedings (2009)

J. E. Ralph, K. A. Marsh, A. E. Pak, W. Lu, C. E. Clayton, F. Fang, W. B. Mori, and C. Joshi
Self-guiding of ultrashort,relativistically intense laser pulses through underdense plasmas in the blowout regime, Physical Review Letters,**102**,175003(2009)

F. Fang, C.E. Clayton, K.A. Marsh, A.E. Pak, J.E. Ralph, N.C. Lopes, and C. Joshi
Pump depletion limited evolution of the relativistic plasma wave-front in a force laser wakefield accelerator, Plasma Physics and Controlled Fusion,**52**,024003(2009)

A. E. Pak, K. A. Marsh, J. E. Ralph, W. Lu, C. E. Clayton, and C. Joshi

Indication of Local Laser Pump Depletion via Transmitted Self-Guided Laser Light, AIP Conf. Proc. 1086, 202 (2009)

A. E. Pak, K. A. Marsh, J. E. Ralph, W. Lu, C. E. Clayton, and C. Joshi
Indication of Local Laser Pump Depletion via Transmitted Self-Guided Laser Light, AIP Conf. Proc. 1086, 202 (2009)

A. Pak, G. Gregori, J. Knight, K. Campbell, D. Price, B. Hammel, O. L. Landen, and S. H. Glenzer
X-ray line measurements with high efficiency Bragg crystals, Review of Scientific instruments,**75**,3747(2004)

Abstract of the Dissertation

Injection of Tunnel Ionized Electrons into Laser-Produced Wakes

by

Arthur Pak

Doctor of Philosophy in Electrical Engineering

University of California, Los Angeles, 2010

Professor Chandrashekhar Joshi, Chair

The injection of electrons via tunneling ionization into a laser driven wakefield accelerator has been studied with experiments, theory and simulations. In this work the large difference in ionization potentials between successive ionization states of trace atoms, is used as the mechanism for injecting electrons into a laser driven wakefield. Here a mixture of helium and trace amounts of either nitrogen or methane (CH_4) gas was used. Electrons from the K shell of either nitrogen or carbon were tunnel ionized near the peak of the laser pulse and injected directly into the wake. The wake was created by electrons from majority helium atoms with contributions, depending on which gas mixture was used, from the either the L shell of nitrogen or the hydrogen and the L shell of carbon.

Using the helium nitrogen gas mixture, the threshold intensity at which trapping was observed to occur corresponded to the intensity required to ionize the 6th electron from nitrogen(i.e. the first electron within the K shell). This indicates ionization of the K-shell of nitrogen triggers injection, and the subsequent trapping and acceleration of electrons. The electron energy spectrum was observed to be quasi-continuous for a laser $a_o \geq 2$. This spectral shape is a result

of the continuous ionization and injection which occurs as long as the magnitude of the laser field remains above that required to ionize the K-shell of the nitrogen. The relative amount of charge accelerated, the intensity threshold, and spectral shape of accelerated electrons were found to be in good agreement with 3-D particle in cell code simulations which modeled the interaction.

The trapping of electrons into a wakefield was studied theoretically using a 3-D Hamiltonian description of an electron within a electromagnetic field. From this description, a constant of motion can be found which relates the scalar and vector potentials of the wake and laser to the momentum of an electron. In this manner the required potential difference that an electron must experience to become trapped can be solved for. This estimate of the required potential difference for trapping to occur was found to be in good agreement with that observed in 2-D particle in cell code simulations.

Using the 3-D scaling laws for the laser wakefield accelerator in the blowout regime, it was found injecting electrons directly into the wakefield, as they are when injected via ionization, significantly increases the potential difference, or the amount of energy available to the electron, to become trapped. This increase in available potential can in turn be used to lower the absolute wake amplitude necessary for trapping to occur. This reduction in wake amplitude means that electrons can be trapped into wakes with lower amplitudes driven by lasers with lower peak powers.

The acceleration of electrons at reduced laser powers using ionization injection has been confirmed experimentally. Using the helium nitrogen or helium methane gas mixtures, accelerated electrons have been routinely observed using laser powers 2-4 times lower that what has been required to accelerate electrons from plasmas created from pure helium gas at similar densities.

CHAPTER 1

Introduction

Highly energetic electron beams have many uses, from providing a way to study the building blocks of matter, to generating the ultra-short, coherent sources of x-rays used to explore the structure of biological molecules [1, 2] . However, the machines required to create and accelerate electron beams to these high energies measure kilometers in length and cost billions of dollars to build and maintain. In addition the next generation of particle colliders will require electron beams with up to ten times more energy than obtained at LEP, the highest energy e^+e^- collider to date. This requirement makes using conventional accelerator technology based on microwaves prohibitively expensive. In 1979, Tajima and Dawson proposed a new method of accelerating electrons to high energies using a plasma-based accelerator [3]. The accelerating field in a plasma can be ~ 1000 times larger than those in conventional accelerators. This feature could allow for GeV-class beams from conventional accelerators to be further accelerated to energies on the order of TeV over a very short distance and for a relatively small cost. At the same time, uses for electron beams with moderate energies are expanding, from potential medical applications [4] to novel light sources, including free electron lasers [5]. The large accelerating gradients of plasma accelerators can be created with smaller laser facilities allowing the entire accelerator facility to be miniaturized. This reduction in accelerator size could reduce the cost and increase the accessibility of such facilities. Comparing a conventional accelerator

to a plasma-based accelerator, one can see that the essential architecture is the same, but the scale of the accelerating gradient and the size of the accelerating structure are radically different. In a conventional accelerator, a iris loaded copper waveguide is used to support a radio frequency (RF) mode that has a longitudinal electric field component that propagates at the phase velocity of light. The longitudinal electric field of the RF mode can be used to give energy to electrons, accelerating them to relativistic energies with a gradient of $\sim$ 100 MeV / m. The maximum acceleration gradient is limited by the power of the RF mode that the waveguide can support without arcing. This limitation determines the overall length of a conventional accelerator. For example, the Stanford Linear Accelerator (SLAC) can accelerate and electron bunch to $\sim$ 50 GeV in 3200 meters.

Tajima, Dawson and Chen [3, 6] proposed that an analogous acceleration process can occur within a plasma using a space-charge density wave rather than a TM mode as in a waveguide. As illustrated in Fig. 2.1, a highly relativistic charged particle beam or an intense laser pulse driver first enters a quasi-neutral plasma. On a short time scale, the heavier positively charged ions of the plasma cannot react to the impulse of the driver, while the lighter electrons are displaced around the driver. The displaced electrons are attracted back towards the ion column and end up oscillating around the center of the ion column on a time scale of electron plasma frequency ω_p. This oscillation creates an electron density plasma wave known as a wake. The separation between the static ions and the oscillating electrons creates an electric field which, just like the conventional waveguide, has a longitudinal electric field component that propagates at a phase velocity that is approximately equal to the group velocity of the drive pulse ($\sim$c) and therefore can be used to accelerate electrons to high energies. Examining the on axis lineout of the longitudinal accelerating field created by the laser pulse in

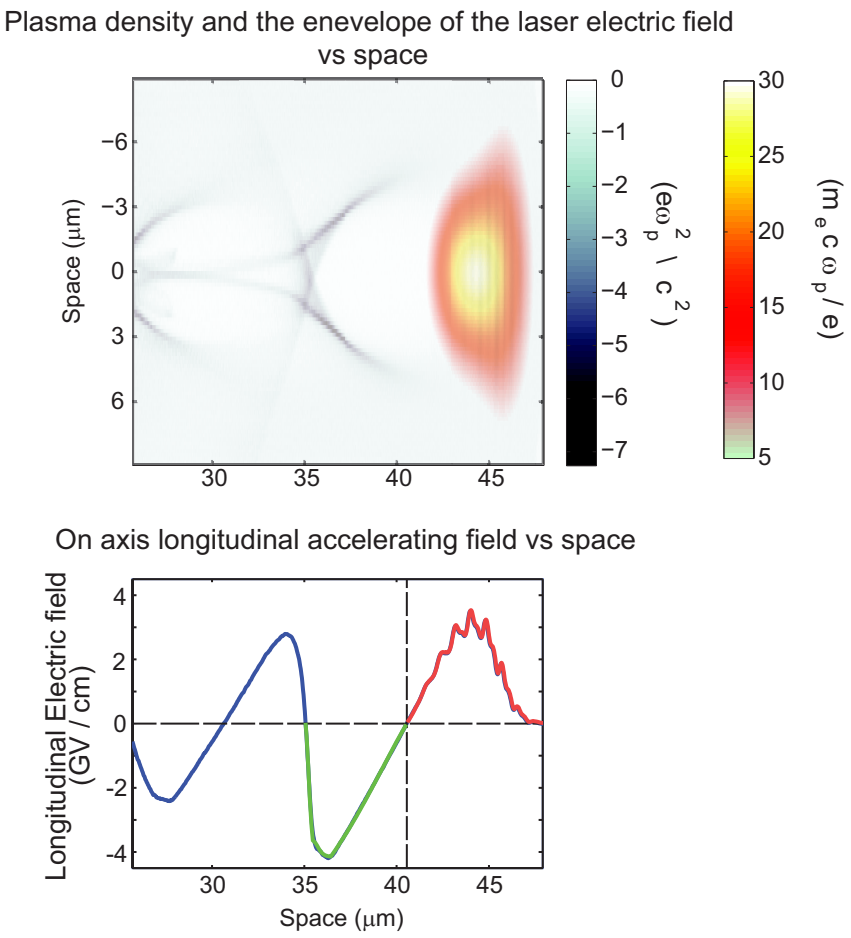

Figure 1.1: The plasma charge density shown (grey) driven by a laser pulse (color) which is propagating to the right. The plasma density and the envelope of the laser electric field have been plotted vs space. The on axis longitudinal accelerating electric field from the wake created (solid line) has been plotted below. The accelerating phase of the first period of the wake has been highlighted in green while the decelerating phase of the first period has been highlighted in red. Here ω_o/ω_p is 10.96.

Fig. 2.1, it can been seen that an electron injected into the first period of the wake will be accelerated towards the middle of the first period where the electric field is zero. Therefore, within a wakefield there is an *acclerating* phase (shown in green) and a *decelerating* phase (shown in red), where an injected electron will either be accelerated in the co-propagating or counter-propagating direction of the driver respectively.

The accelerating gradient of these so-called wakefield accelerators can be approximated as $E = (v_\phi m \omega_p / e)\epsilon$. Here v_ϕ is the phase velocity of the plasma wave, and ϵ is the ratio of the plasma wave density, δ_n, to the background plasma density, n_p. Assuming $v_\phi \approx c$ and $\delta_n = 1$, the electric field in the plasma wake can be written E (eV / m) $\approx 96.2 \sqrt{n_p(\mathrm{cm}^{-3})}$. Over the range of plasma densities from 10^{17} - 10^{19} cm^{-3}, this simple scaling gives an accelerating gradient of $\sim$ 30-300 GeV / m, which is approximately 1000 times more than can be achieved in a conventional accelerator. This means that the energy gained by an electron beam in 1 meter of a plasma wakefield accelerator is equivalent to the energy gained from 1000 meters of a conventional accelerator beam line.

Plasma-based accelerators are also different from conventional accelerators in that they can easily create and accelerate ultra-short electron bunches. As shown in Fig. 2.1, the accelerating field of each wake extends over half a plasma wavelength. In many instances, most of the accelerated charge originates from the first period of the wake. This property allows plasma-based accelerators to create ultra-short electron bunches with pulse widths on the order of the plasma wavelength λ_p which is typically tens of femtoseconds. Ultra-short electron bunches created by plasma-based accelerates are already being used in conjunction with magnetic undulators, to create ultra-short sources of light at a wavelength of 10-20 nm [7].

To understand the many difficulties confronting the realization of a plasma-based accelerator, it is instructive to look to prior efforts and accomplishments that make current work possible. While the following overview is selective, its purpose is to briefly introduce some of the major concepts and challenges currently facing the field. These ideas will in turn provide the motivation for the work presented in this thesis.

When the idea of plasma-based acceleration was first proposed, a single, sufficiently powerful laser driver necessary to drive a wake was not available. It was recognized by Dawson that two laser pulses, each with slightly different frequencies, could be mixed together and interfere to create a beat wave [8]. The frequency of the beat wave was set to equal the plasma frequency. A plasma wave could then be resonantly excited by the ponderomotive force of the successive laser pulses of the beat wave. In the first beat wave experiments, an externally generated electron beam was injected into the plasma wave and a portion of the electron beam was observed to both gain and lose energy [9]. Some electrons were shown to be trapped by the plasma wave with a longitudinal field of $> 3\text{GeV/m}$ [10].

Concurrent to the first beat wave accelerator experiments, another scheme, known as the plasma wakefield accelerator (PWFA), was proposed as a method for accelerating electrons [6]. In a PWFA, the Colomb force of a relativistic electron bunch is used to drive an accelerating wakefield. Not long after the PWFA was proposed, the concept was successfully demonstrated using an intense 21 MeV electron beam to drive a wake through a pre-ionized plasma [11]. The drive beam was followed by a 15 MeV witness beam, and the delay between the drive beam and witness beam was adjustable. The energy centroid of the witness beam was observed to increase and decrease as a function of delay between the witness

and the drive beam. The energy fluctuation in the witness beam, as a function of delay, correlated to the expected accelerating and decelerating fields of the beam-driven wake. While the accelerating gradient of the wakefield measured in this experiment was only $\sim$ 1 MeV / m, the concept of a PWFA was clearly demonstrated. Since the initial demonstration of a PWFA, progress in the field has been remarkable. In the most recent and successful PWFA experiments conducted at the Stanford Linear Accelerator (SLAC), a wakefield with a greater than 40 GeV / m accelerating gradient was demonstrated [12].

Part of the initial appeal of PWFA was the fact that the electron beam drive source, while not ideal, was an available technology, whereas creating a beat wave laser source was pushing the technological frontier at the time. Additionally, laser plasma instabilities as well as the difficulty in tuning the beat wave frequency to the plasma frequency made beat wave accelerators challenging to realize. While tremendous accelerating gradients have been demonstrated using the PWFA scheme, they still require a large conventional accelerator to create the electron beam that drives the interaction. To exploit the compactness of plasma wakefield acceleration, a compact driver and electron beam source was needed.

Developments in laser technology, specifically the invention of the chirped pulse amplification technique, enabled the creation of short intense laser pulses capable of directly exciting wakes [13]. Initially, CPA laser systems were limited to producing laser pulses that were hundreds of femtoseconds long with intensities of $\sim 10^{18}$ W/cm^2. Early experiments showed that using this class of laser pulses, large amplitude plasma waves could be driven through the Raman forward scattering instability [14]. Furthermore, it was observed that background plasma electrons could become trapped into these wakes and accelerated to tens of MeV [15]. While the electron beams created in these experiments had large

energy spreads, these results confirmed two important ideas. First, that a new type of laser system could provide a driver for wakefield acceleration, and second, that a source of injected electrons into these wakes can come directly from the plasma itself [16].

Laser technology continued to advance, and eventually a new CPA laser system, which used a titanium-sapphire (Ti:Sapph) crystal as a ultra-broad bandwidth gain medium, became available and was found to be even better suited for laser driven wakefield experiments. Able to fit into a small room on a few table tops, a CPA Ti:Sapph laser can produce ultra-short ($\sim$ 50 fs) laser pulses that contain 10's of terawatts of power. The ultra-short nature of Ti:Sapph laser pulses allows for the large ponderomotive force required to drive a wakefield to be created with a relatively small amount of energy ($\sim$ 1 J). Unlike the longer laser pulse widths that were previously used, the length of a Ti:Sapph laser pulse can be made to be on the order of or less than a plasma wavelength, making it less susceptible to the forward Raman scattering instability. This allows for a short intense Ti:Sapph laser pulse to drive the laser wakefield interaction in a more stable manner. Accelerating wakefields that are driven by a single short laser pulse are known as a laser wakefield accelerators (LWFA) [17].

While Ti:Sapph laser systems are capable of producing a multi-terawatt laser pulse, in order reach the intensities required to drive large amplitude wakes, the pulse must be focused down to a spot size of $\sim$ 10 μm. As a consequence of being focused tightly, the Raleigh length of the laser pulse, Z_R, is on the order of $\sim$ 100 μm. This means that the laser pulse will diverge and lose the intensity required to drive a strong wake after only a few Z_R. Without a mechanism to keep the spot size of the laser pulse from increasing as it diverges through the plasma, the total length of a LWFA, and thus the total energy an electron can

gain, is limited.

To overcome this limitation, a radial plasma density profile can be created such that the diffraction of the laser pulse is minimized. This allows the spot size of the laser pulse to remain small, or 'guided', over longer distances, and extends the length of a LWFA. Two methods have been developed to create such a guiding density profile. In the first method, an electrical discharge is struck across a tube, or capillary, of hydrogen gas creating a plasma. The electron temperature close to the capillary wall is lower than that near the center of the discharge. Therefore over a short amount of time ($\sim$ 100 ns), hotter electrons located on axis of the discharge will diffuse radially, creating an appropriate density channel that can guide a laser pulse [18]. A second method, known as self-guiding, relies on matching the ponderomotive force of the laser which expels the plasma electrons to the space-charge attraction force that the plasma ions exert on the expelled electrons, such that the wake that is driven by the laser pulse also serves to guide the laser pulse [19]. Both of these techniques have been used to extend the length of a LWFA from hundreds of microns to centimeter scale lengths [20, 21]. Extending the length of acceleration is an important step in achieving higher accelerated energies, however the total energy gain of a LWFA in many instances is not limited solely by the accelerator length.

To see this, again consider Fig. 2.1, and notice that there is an accelerating and decelerating phase of the longitudinal electric field in the wake. In order for electrons to be accelerated by the longitudinal electric field of a LWFA, they must remain within the accelerating phase of the plasma wave. Ideally, as the electron beam and wake travel through the plasma together, the electron bunch would remain at the same relative phase location within the wake, so as to experience a constant accelerating field. Unfortunately, in a LWFA, the phase velocity of

the wakefield is the group velocity of the laser drive pulse, $v_g = c(1 - \frac{1}{2}\frac{n_e}{n_c})$ in the plasma and for current lasers is not the same as the velocity of a relativistic electron beam (∼c). This difference in velocity causes a relative slip in position between the electron beam and the accelerating phase of the wakefield. Eventually the electron beam will slip into the decelerating phase of the wakefield and begin to lose energy. The length over which the electron beam can gain energy from the accelerating phase of the wakefield is known as the dephasing length. This length limits the maximum energy gain that an electron experiences in a LWFA. An important difference between the LWFA driven by current lasers where $\omega_o/\omega_p \approx$ on the order of 10-100 and the PWFA that uses an ultra-relativistic electron beam is that dephasing does not limit the energy gain in a PWFA, until the drive particles loose almost all their energy, as there is no appreciable difference in velocity between an electron beam driver and the trailing beam. In a plasma the group velocity of a laser, or phase velocity of the wake is $\propto 1/n_p$. This is why as the plasma densities are lowered, the phase velocity and thus the dephasing length will increase, allowing electrons to gain more energy from the wake [22].

Just as important as extending and optimizing the length of acceleration in a LWFA is the injection of electrons into these accelerating wakefields. Understanding the injection and trapping of electrons is a critical step for creating high quality reproducible electrons beams necessary for use in high energy physics, free electron lasers and medial applications. Electrons can either be externally injected from an electron beam source into a LWFA or they can be injected from the background plasma into the LWFA.

External injection of an electron beam into a LWFA is challenging for many reasons. First, in order for the external electron beam to experience a uniform

accelerating field the beam must be ultra-short and transversely small on the order of a plasma wavelength. Again, while electron beams with these parameters are obtainable, they require a large and complex conventional accelerator to be achieved. Another challenge for external injection is synchronizing the electron beam with the phase of the accelerating field in the laser driven wake. To date, external injection of an electron beam into a LWFA has not been demonstrated.

The most straightforward method of injection in the LWFA is the so called self-trapping of background plasma electrons into the wake. Electrons are considered trapped when they gain enough energy from the wakefield such that their velocity is equal to the phase velocity of the wakefield. Self-trapping can occur when a strong wake is driven and a large electron density spike forms at the back of the first period of the wakefield. As more and more electrons are drawn back to the end of the plasma period, this large density spike can deflect some of the electrons and inject them into the large longitudinal electric field at the back of the wake. Here, they are quickly accelerated by the wakefield to the phase velocity of the wake. These electrons are trapped and can continue to gain further energy from the wakefield.

In 2004, three groups, all using CPA Ti:Saphh laser systems, demonstrated that self-trapping and acceleration of electrons in this manner could lead to the generation of an electron beam with a relatively narrow energy spread [23, 24, 25]. Even though each experiment was conducted using slightly different laser powers, plasma densities, and plasma lengths, each group observed a quasi-monoenergetic electron beam with $\sim$100 pC of charge, at a peak energy greater than 70 MeV with a beam energy spread of $\pm$ 2-12 %. 3-D OSIRIS particle in cell simulations indicated that despite differences in experimental parameters, similar physics lead to an evolution of the laser pulse in each experiment, which in turn triggered the

self-trapping of electrons and production of a monoenergetic electron beam [26]. These initial results created a lot of interest and excitement as they showed that electron beams with useful amounts charge, and energy, and with much smaller energy spreads that previously observed could be created from a LWFA [27]. However, there was no theory or framework to follow on how to control or optimize the self-trapping and acceleration processes.

To address these issues, a phenomenological theory was developed which indicates the optimal laser and plasma parameters for self-guiding and self-trapping to occur [28]. In the regime where this theory is satisfied, experimental results have shown that stable self-trapping exists and the properties of electron beams are in agreement with those predicted [29, 30, 31]. However this regime requires a very intense laser pulse capable of fully cavitating all the electrons from the wake [19]. As plasma densities are lowered to achieve higher electron energies, the energy of the laser pulse required to blow out all the electrons from the wake increases to beyond current commonly available laser systems. In this regime, the largest energy that electrons have been accelerated to is $\sim$ 800 MeV using $\sim$ 200 TW of laser power to drive an accelerating wakefield and self-trap electrons at a plasma density of 5.5 x 10^{18} cm^{-3} [31].

Alternatively, a method of injecting electrons into laser driven wakefields using multiple lasers pulses, know as colliding pulse injection, was proposed and demonstrated [32, 33]. In current colliding pulse experiments, a single injection pulse, collides at a small angle with a stronger counter propagating drive pulse. The collision between the two laser pulses initiates the injection of electrons in the following manner. The drive laser pulse first creates a wakefield, but does not drive the wake strongly enough such that self-trapping occurs. The weaker injection pulse, has the same frequency and is polarized in the same direction as

the drive laser pulse. When the two pulses collide, they interfere with one another and briefly create a standing wave with a large ponderomotive force. It is this ponderomotive force which accelerates background plasma electrons within the wake up to the phase velocity of the wake causing them to be injected and trapped.

Recent experiments have demonstrated that using 40 TW of laser pulse split into the drive and injection pulses, electrons could be injected and accelerated in wakefields at plasma densities as low as $\sim$ 6 x 10^{18} cm^{-3}. In these experiments electrons with energies up to 250 MeV have been created with energy spreads as low as 5 % [34]. An advantage of this technique is that the energy of the electron beam can be controlled and varied by limiting the acceleration length through controlling the collision timing between the drive and injection pulse. In recent experiments the energy was varied from 50 to 250 MeV by simply changing the collision timing. For a constant delay between the injection and drive pulse, the standard deviation in the peak energy of the electron beam was found to be $\sim$ 6%.

Reaching accelerated energies far beyond 250 MeV using colliding pulse injection is challenging as the intensity of the drive laser pulse is not sufficient to self-guide the laser pulse over many Rayleigh lengths. Furthermore, because the drive and injection pulse must counter propagate and cross at an angle to one another, implementing a capillary discharge plasma to guide the laser pulse is also very challenging and to date has not be achieved. The relatively short acceleration distance has thus limited the energy gain of electrons which have been injected via the colliding pulse technique.

Transitions from higher to lower plasma densities have also been used to inject electrons into wakefield accelerators. If the transition from higher to lower

density is many plasma wavelengths long, then as the wakefield moves from a region of higher density to lower density, electrons which were not trapped in the first plasma wavelength can be more easily trapped in the subsequent slower moving plasma periods [35]. The electron beam energy and energy spread will be determined by the length of the density ramp. Experiments to investigate this density down ramp injection were conducted using a 50 TW laser focused onto a short $\sim$ 300 micron density transition from 1 x 10^{19} cm^{-3} to vacuum [36]. Limiting the acceleration distance to that of a short density down ramp, electron beams with low peak energies of $\sim$ .76 MeV but with narrow absolute energy spreads of .17 MeV were created in these experiments. In order to reach higher energies, these electron beams need to be injected into a second acceleration stage. Ideally this second acceleration stage would preserve the electron energy spread while increasing the peak energy of the electron beam. Additionally a sharp decrease in plasma density on a length scale that is on the order of a plasma wavelength can be used to inject and trap electrons into the accelerating phase of a wakefield [37]. As the plasma density decreases, the plasma wavelength increases and injected electrons are 're-phased' within the plasma wave such that they are able to gain enough energy from the accelerating phase of the wakefield as to be trapped. This idea has be experimentally demonstrated, where a pre-pulse was used to create a pre-plasma which then diffused to a lower density before the main pulse arrived [38]. The drive pulse propagated transversely to the pre-pulse. The pre-pulse was focused down to $\sim$4 μm at a time 4 ns before the arrival of the pump pulse. The background plasma density was $\sim$2x10^{19} cm^{-3} and when the pre-pulse was used the number of accelerated electrons above 100 KeV was found to increase by 25% when the pre-pulse was used to trigger injection.

While both the colliding pulse and density transition injection schemes have been shown to create stable electron beams with good beam qualities, they are

also the most technically challenging to execute and are so far have produced limited electron energy gains. The self-trapping of electrons has produced the highest energy electrons beams in a LWFA and is the most straightforward injection scheme. However, it will be shown later, as the plasma density is lowered to achieve higher accelerated electron energies, the power required to self-trap electrons becomes larger than the most powerful laser systems available today. A simple injection scheme, able to inject electrons at lower densities while using less power, would be very desirable. Additionally, to simplify the acceleration process, it would be beneficial if the injection mechanism could be preformed within the main accelerator and would not require the need for multiple accelerator stages.

Recently it was shown that in a beam driven wakefield experiment, that electrons could be injected into a wakefield via ionization [39]. In these experiments a column of lithium vapor was created using a heat pipe oven. The lithium vapor was confined within the oven at both ends with a buffer of pure helium gas. This buffer caused the lithium vapor density to taper off through the neutral helium gas before reaching the ends the oven. In this density ramp, the space charge of the SLAC beam was sufficient to ionize the 1st electron from the outer shell of the lithium vapor but was not strong enough to ionize the 1st helium electron. The free lithium electrons were pushed out around beam setting up a wakefield. The electron beam driver was then focused by the radial fields of the wake. Due to this focusing, the space charge electric field of the electron beam was increased such that it became large enough ionize the more tightly bound 1st electron of helium. The electrons from helium were ionized and injected directly into the wakefield created from the lithium electrons. Additionally, electrons from aluminum and oxygen containments in a hydrogen filled capillary discharged plasma were also thought to be injected into a laser driven wakefield through ionization [40]. While ionization injection in the PWFA regime has been previously stud-

ied, the benefits of using such an injection technique had not been studied or understood in the LWFA regime.

This thesis investigates the controlled injection of electrons via tunneling ionization into a LWFA. A physical picture, along with the scaling laws for a laser wakefield accelerator operating in the matched blowout regime will be presented. It will then be shown how tunneling ionization can be used to inject electrons directly into a LWFA. The wake potential required for the trapping of electrons injected via ionization will be determined using a Hamiltonian approach. The available wake potential in the matched blowout regime is then approximated, and the influence than ionization injection has on the trapping condition and final energy gain of the electrons will be discussed. It is found that this injection scheme permits the trapping of electrons using lower laser powers than have currently been demonstrated. The analytical model developed for the trapping of injected electrons is found to be in good agreement with simulations. The setup and methods used to experimentally investigate the trapping of electrons which have been injected via ionization will then be discussed. Results from these experiments indicate that electrons can indeed be injected into a laser driven wakefield via ionization. Additionally experimental results show that tunneling ionization injection reduces the amount of laser power required to trap electrons as compared to self-trapping. Accelerated electron spectra, divergence, and charge measurements are presented and found to be in good agreement with those observed in 3-D OSIRIS simulations. Using these results as a basis, refinements to the ionization injection scheme and suggestions for future work, as well as recent experimental results will be discussed. In principle, the injection of electrons via tunneling ionization should allow for a simple, high efficiency plasma-based accelerator with the ability to trap electrons at the low plasma densities required for achieving GeV class electron beams necessary for many high energy physics

applications.

CHAPTER 2

Laser Wakefield Acceleration in the Blowout Regime

The accelerating electric field of a LWFA is created from the charge separation of plasma electrons and ions within the wake. It is the ponderomotive force of a focused laser pulse which creates the charge separation in a LWFA. The ponderomotive force is a time averaged force that a charged particle experiences as it moves through a electro-magnetic (EM) field which has a gradient. To illustrate how a spatial gradient of a oscillating electric field can impart a force, first consider an electron in an infinite and uniform oscillating electric field. The electron will oscillate back and forth due to the force of the electric field. Since the field is uniform and infinite in space, the electron will oscillate in space symmetrically around its initial location. Taking the time average of such a motion would indicate that there is no net force on the electron as the time average location of the electron is its initial location. If the field instead of being uniform is given a spatial gradient, now as the electron oscillates in space it no longer experiences a uniform electric field. Since the field is no longer uniform in space, the electron is unable to oscillate around its initial location and instead will move in the direction of the gradient of the field. The force associated with the time averaged movement of an electron in the direction of the gradient of the electric field is known as the ponderomotive force.

Analytically, the ponderomotive force on a non-relativistic electron ($v_{osc} \ll c$) has been derived in the following manner [41, 42]. First, consider the electric field of plane wave with a spatial gradient in $\vec{r}$ given by,

$$\vec{E} = \vec{E}(r)cos(\omega_o t - k_o z) = \vec{E}(r)Re\{e^{i(\omega_o t - k_o z)}\} \tag{2.1}$$

where ω_o and k_o are the laser angular frequency and wave number, respectively and $E(r)$ is the radial envelope of the plane wave. To describe the motion of an electron in such a field, the equation of motion of an electron in an EM field is used,

$$m\frac{d\vec{v}}{dt} = -e(\vec{E} + \vec{v}X\vec{B}) \tag{2.2}$$

where m and e are the mass and charge of an electron, $\vec{v}$ is the velocity of the electron and $\vec{B}$ is the magnetic field. The relationship between the electric and magnetic field is given by,

$$-\frac{\partial \vec{B}}{\partial t} = \vec{\nabla}X\vec{E} \tag{2.3}$$

and for a plane wave with constant amplitude this gives,

$$\begin{aligned} i\omega Re\{B\} &= ik_o E_o Re\{e^{i(\omega_o t - k_o z)}\} \\ B &= \frac{n}{c}E_o Re\{e^{i(\omega_o t - k_o z)}\} \end{aligned} \tag{2.4}$$

where n is the index of refraction, which for vacuum is equal to 1 and c is the speed of light. Using the relationship given by 2.4, it can be seen that for non-relativistic electrons ($v \ll c$) the $\vec{v}X\vec{B}$ component of the equation of motion is small compared to the force of the electric field. To first order, the equation of motion is then,

$$m\frac{d\vec{v}_1}{dt} = -e\vec{E}(r)Re\{e^{i(\omega_o t - k_o z)}\} \tag{2.5}$$

this equation can be successively integrated to solve for the first order velocity and position,

$$\vec{v}_1 = -\frac{e}{mi\omega_0}\vec{E}(r)Re\{e^{i(\omega_o t - k_o z)}\} \tag{2.6}$$

$$\vec{r_1} = \frac{e}{m\omega_o^2}\vec{E}(r)Re\{e^{i(\omega_o t - k_o z)}\} \tag{2.7}$$

These equations indicate that the first order motion is in the direction of electric field polarization. To see how the gradient of electric field gives rise to the ponderomotive force, the equation of motion needs to be expanded to the second order. To do this the equation of motion is again solved using the 2nd order of the Taylor expanded electric field, using the first order quantities of $\vec{r}$ and $\vec{v}$ and including the $\vec{v}X\vec{B}$ force. The second order force equation is given by,

$$F_2 = -eRe\{(\vec{r_1}\cdot\nabla\vec{E}(r) + \vec{v}_1 X\vec{B})e^{i(\omega t - kz)}\} \tag{2.8}$$

The magnetic field can be rewritten in terms of the electric field using eqn. 2.3 as

$$\vec{B} = -Re\{\frac{1}{i\omega_o}\vec{\nabla}X\vec{E}\} \tag{2.9}$$

Substituting this relation and the first order quantities $\vec{v}_1$ and $\vec{r}_1$ into eqn. 2.8, the second order force equation can be rewritten as,

$$\begin{aligned} F_2 &= Re\{-e[\frac{e}{m\omega_o^2}(\vec{E}\cdot\vec{\nabla})\vec{E} + \frac{-e\vec{E}}{mi\omega_o}X(\frac{-\vec{\nabla}X\vec{E}}{i\omega_o})]\} \\ F_2 &= \frac{-e^2}{m\omega_o^2}Re\{(\vec{E}\cdot\vec{\nabla})\vec{E} - \vec{E}X\vec{\nabla}X\vec{E}\} \end{aligned} \tag{2.10}$$

Using the vector identity,

$$\vec{A}X(\vec{\nabla}X\vec{B}) = \vec{\nabla}(\vec{A}\cdot\vec{B}) - (\vec{A}\cdot\vec{\nabla})\vec{B} - (\vec{B}\cdot\vec{\nabla})\vec{A} - \vec{B}X(\vec{\nabla}X\vec{A}) \tag{2.11}$$

the second order force equation can be rewritten as,

$$\begin{aligned} F_2 &= \frac{-e^2}{2m\omega_o^2}Re\{\vec{\nabla}(\vec{E}\cdot\vec{E})\} \\ F_2 &= \frac{-e^2}{2m\omega_o^2}\vec{\nabla}\{E(r)^2 cos(\omega_o t - k_o z)^2\} \\ F_2 &= \frac{-e^2}{2m\omega_o^2}\vec{\nabla}\{E(r)^2\frac{1}{2}[1 + cos(2(\omega_o t - k_o z))]\} \end{aligned} \tag{2.12}$$

The ponderomotive force is found by time averaging the second order force, which gives

$$F_P = \frac{-e^2}{4m\omega_o^2}\vec{\nabla}\{E^2\} \tag{2.13}$$

For a focused laser pulse which is finite in time, there is a gradient in the electric field in the radial and longitudinal directions. This gradient causes the ponderomotive force of the laser to push electrons in the forward and radial directions out around the pulse envelope. The displaced electrons are then attracted back, by the Coulombic force, towards the more positively charged region space located around the laser axis. The electrons will overshoot the axis and oscillate, creating the electron plasma wave known as a wake. The ponderomotive force for a relativistically intense focused laser pulse, where the force of the electric field is on the order of the $\vec{v}$ X $\vec{B}$ force due to $v_{osc} \approx c$, has also been solved for in [43]. The relativistically correct ponderomotive force, as with non-relativistic ponderomotive force, was found be directed the direction of the gradient of the field and proportional to the square of the electric field. Simulations preformed in [43] indicate that at relativistic laser intensities, the ponderomotive force of a focused laser pulse still acts to push electrons out in the forward direction and symmetrically in the radial direction.

In a plasma, electrons which are displaced by the ponderomotive force of the laser will be attracted back towards their initial location on the timescale of the plasma frequency ω_p given by,

$$\omega_p = \sqrt{\frac{n_p e^2}{\epsilon_o m}} \tag{2.14}$$

Here, n_p is the background plasma density, and ϵ_o is the vacuum permittivity. Electron plasma waves or wakes are created by the charge separation between plasma electrons which are pushed out by the laser, and the stationary ions which are ~ 2000 times more massive and do not respond on the ultra-fast time

scale ($\sim$ 100 fs) of the laser pulse. Electrons displaced by the laser pulse will respond with a corresponding plasma wavelength $\lambda_p = 2\pi c/\omega_p$.

When a short intense laser pulse interacts with a plasma to drive a wakefield, there are a few useful parameters and concepts which can be quickly used to infer how strong of an interaction will take place between the laser and plasma. A very important parameter is the normalized vector potential of the laser pulse, a_o, given by,

$$a_o = \frac{eE_o}{mc\omega_o} \simeq 8.6x10^{-10}\sqrt{I_o(W/cm^2)}\lambda(\mu m) \tag{2.15}$$

where I_o is the peak average laser intensity, and λ is the laser wavelength. The parameter a_o is often used to quickly infer the magnitude of the wake being driven by the laser pulse. *Linear* wakes are driven at lower laser intensities, when the laser $a_o < 1$ and *non-linear* wakes are driven at larger laser intensities with $a_o > 1$. There are so many differences in the properties of linear and non-linear wakes, and how they interact with a laser field, that two distinct regimes of study have been created. One important difference between the linear and non-linear regime is the wake amplitude defined as $\delta n/n_p$, here $\delta n = n_p - n$ where n is density within the wake. In the linear regime, $\delta n/n_p \ll 1$ and a sinusoidal plasma wave is created that can be described in 3-D by the cold fluid equations [44]. When a large normalized vector potential $a_o \geq 1$ is used, a non-linear wake is driven with a saw toothed longitudinal electric field profile and a $\delta n/n_p \sim 1$ is created [45]. Analytically, the properties of non-linear wakes driven by a laser with $a_o > 1$ have been described in 1-D assuming a non-evolving and spatially broad driver ($2\pi W_o/\lambda_p \gg 1$) [46]. The magnitude and shape of the wake amplitude are important in determining the focusing and accelerating fields of the wakefield. In this work, $a_o \gtrsim 2$ and laser pulse widths on the order of λ_p are used. The properties of wakes created with these laser parameters will be described in

detail below. While the a_o of the laser determines the wake amplitude, one must consider that the plasma can in turn modify the radial and longitudinal profile of the laser pulse. This can change the a_o of the laser pulse and thus the wake amplitude that is driven, which in turn can change the dynamics of the LWFA.

When an intense laser enters a underdense plasma, the plasma can act as a lens to focus the spot size of the laser. This is known as relativistic self-focusing and is caused by two effects that increase the index of refraction on axis of the laser pulse [47]. The index of refraction can be increased on axis due to the ponderomotive force of the laser which, by pushing out electrons radially, lowers the plasma density on axis. Additionally, electrons oscillating in a relativistically intense field will have a corresponding relativistic mass increase. This mass causes the index of refraction on axis to become larger. Since the magnitude of the laser electric field is larger on axis, the relativistic mass increase also causes the index of refraction to become larger on axis. The laser pulse can be transversely focused due to experiencing a larger index of refraction on axis and a smaller index of refraction off axis. Relativistic self-focusing of the laser pulse occurs when the power of the laser pulse exceeds P_c, the critical power for self-focusing given by,

$$P_c(GW) \simeq 17.4\frac{\omega_o^2}{\omega_p^2} \tag{2.16}$$

The laser pulse will continue to focus until all the electrons are expelled from within the spot size of the laser and there is no longer a gradient in the index of refraction in the radial direction. The ratio of the laser power, P, to P_c gives a good indication of how strongly the laser pulse will be focused by the plasma.

The laser pulse can also be compressed longitudinally in time by the density gradient of a wake via photon acceleration and deceleration [48, 49]. The plasma density within a wakefield varies in an approximate sinusoidal manner. Relative to the background plasma density, the local electron density at the front of the

wake is decreasing, while at the back of the wake where electrons are being pulled back, the electron density is increasing. These local time dependent changes in plasma density, at the front and back of the wake, cause the local index of refraction to change with time. Due to this effect, the frequency of the laser pulse can be increased and decreased locally within the wake. In the middle of the wake, the local plasma density is approximately constant, and therefore locally the laser pulse will move at a constant un-shifted group velocity. As the frequency of the laser changes, the local group velocity also changes, causing laser light at the back of the wake to move faster and light at the front of the wake to move slower than the un-shifted group velocity of the laser pulse. This effectively compresses the laser field in time within each wake. If the laser pulse width is on the order of one plasma wavelength the entire pulse will be compressed and this can lead to an increase the the laser intensity and subsequent a_o [50]. However if the laser pulse width is much greater than a plasma wavelength, the laser pulse will be compressed within each wake driving a LWFA in the self-modulated regime.

In the work discussed here, laser intensities on the order of $\sim 10^{19}$ W/cm^2 with $a_o \gtrsim 2$ and pulse widths $\sim \lambda_p$ were used to create a LWFA in the blowout regime. This so called blowout regime occurs when the laser intensity becomes large enough such that the ponderomotive force of the laser is strong enough to fully expel all of the electrons from within the wake that is created, leaving behind an ion channel. An advantage of operating in this regime is that there exits a matched self-guiding condition, in which the intensity, spot size and pulse width of the laser pulse are matched to the plasma density, such that the driven wake serves to minimize the diffraction of the laser pulse [19]. This allows a strong and stable wake to be sustained over many Rayleigh lengths and can increase the interaction length between trapped electrons and the accelerating field of the

wake. The matched self-guiding condition is valid when the laser $a_o \gtrsim 2$ and the pulse width of the laser electric field is on the order of half a plasma wavelength. When these conditions are met, the matching condition is given by,

$$k_p W_o \simeq k_p R_b = 2\sqrt{a_o} \tag{2.17}$$

where $k_p = 2\pi/\lambda_p$ is the plasma wave number, W_o is the spot size of the laser and R_b is the blowout radius of the wake. Remarkably, even when the spot size and or pulse width are not precisely matched to the plasma density, simulations and experiments have shown that the laser pulse will evolve within the plasma towards the matched spot size and pulse width, via relativistic self-focusing and longitudinal pulse compression [51].

While the change in index of refraction allows the part of the laser pulse that resides within the wake to be transversely guided, the very front of the laser pulse, which creates the wake, is not guided and continuous to expand because of diffraction. The rate at which the front of the laser pulse is *etched* away by a non-linear wakefield was estimated in 1-D to be given by $v_{\text{etch}} = c\omega_p^2/\omega_o^2$ [52]. The etching of the front of the laser pulse will eventually cause the pulse to lose so much energy that it can no longer support the necessary wake amplitude to remain self-guided. The minimum density depression necessary for guiding the pulse is given by,

$$\left(\frac{\delta n}{n}\right) \geq \frac{4}{(k_p W_o)^2} \tag{2.18}$$

which leads to the condition $k_p W_o = \sqrt{2}$. The length over which the laser pulse can remain self-guided before losing so much energy that this condition can no longer be satisfied is known as the pump depletion length and is given by,

$$L_{PD} = \frac{c}{v_{\text{etch}}} c\tau = (\frac{\omega_o}{\omega_p})^2 c\tau \tag{2.19}$$

where τ is some characteristic pulse width of the laser, often chosen to be the FWHM of the electric field in time [28]. It seems that τ should depend on the intensity of the laser pulse, as τ should be the width of the pulse starting from where the intensity of the laser pulse is strong enough to create the sufficient wake amplitude to self guide the pulse. Indeed as Lu et al. point out the etching velocity was found to agree with velocity observed in many OSIRIS simulations over a range $2 \lesssim a_o \lesssim 2\sqrt{\frac{n_c}{n_p}}$.

Figure 2.1 is taken from a 2-D OSIRIS simulation, and details the wake created in a plasma by a Ti-Sapph laser pulse at a density of 1.4x10^{19} cm^{-3} using a laser pulse with an a_o of 2.5, a matched spot size and pulse width of $\sim$4.5 μm and $\sim$15 fs, respectively. As shown in fig. 2.1 b) the round wake creates an approximately linear accelerating field, E_z, in the direction of laser propagation within the first period of the wake. Electrons which are injected into the wake will be accelerated by the longitudinal and radial fields towards the center of the wake. Electrons that are injected into the back half of the wakfefield are in the *accelerating* phase of the wake as they can gain energy and move in the direction of laser propagation. Electrons injected into the first period of the wake are considered trapped if they can gain enough energy to reach the phase velocity of the wake v_ϕ. Eventually, trapped electrons will gain so much energy, that they begin to move faster that v_ϕ and enter into the front half of the wake. This region is known as the *decelerating* phase of the wake, as the longitudinal field in this region attracts the electrons back towards the center of the wake, in the opposite direction of laser propagation. As detailed in [28], the entire wake is traveling at a phase velocity v_ϕ which is equal to the linear group velocity of the laser field in the plasma, minus the etching velocity of the laser pulse by the wake and is

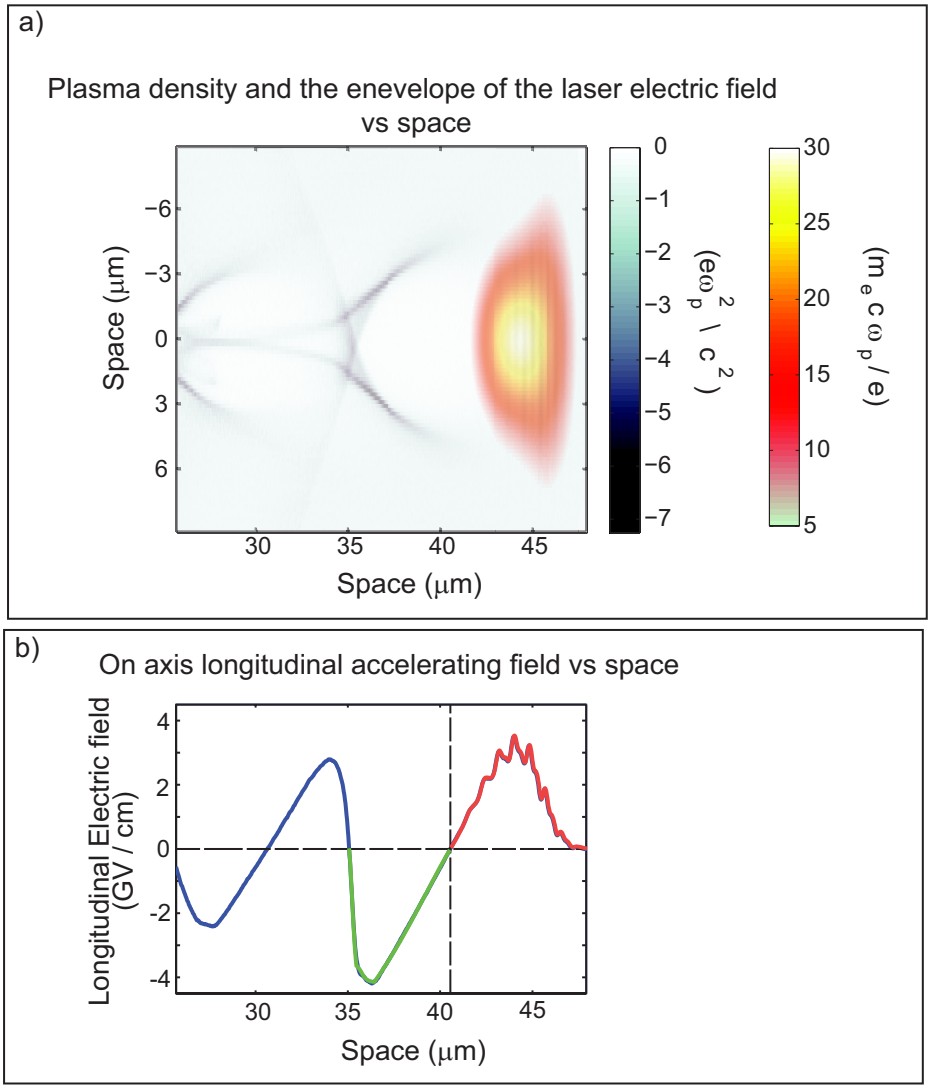

Figure 2.1: a) The electron charge density from helium (grey) driven by a laser pulse (color) which is propagating to the right with an a_o of 2.5, pulse width of electric field was 15 fs and spot size is 4.5 μm. b) The longitudinal accelerating electric field from the wake created. Here the accelerating and decelerating phase of the first period of the wakefield have been shaded in green and red respectively. $\omega_o/\omega_p = 10.96$.

given by,

$$v_\phi = v_g - v_{\text{etch}} \approx c(1 - \frac{1}{2}\frac{\omega_p^2}{\omega_o^2}) - c\frac{\omega_p^2}{\omega_o^2} = c(1 - \frac{3}{2}\frac{\omega_p^2}{\omega_o^2}) \tag{2.20}$$

Assuming that trapped electrons move at a velocity of c, and are injected at the back of the wakefield, a distance R_b from the center, the length over which trapped electrons can remain in the accelerating phase of the wake is known as the dephasing length and is given by,

$$L_d \simeq \frac{R_b}{c - v_\phi} c \simeq \frac{2}{3}\frac{\omega_o^2}{\omega_p^2} R_b \tag{2.21}$$

[28]. The dephasing length is the maximum distance over which electrons can gain energy from the wakefield before moving into the decelerating phase, while the pump depletion length is the maximum length over which the laser pulse can drive a sufficiently large wake for self-guiding to occur. While these lengths are approximate, they have been shown to give good agreement with simulations and experiments and should be used to determine the appropriate experimental parameter space when operating in the blowout regime.

In the blowout regime all the electrons have been expelled leaving behind a positively charged wake in a approximate spherical shape. From Gauss's law, the magnitude of the electric field within a positively charged sphere is known to increase linearly with the radius. The peak electric field of the wake, E_{max}, will occur at the maximum radius of the wake, R_b. The maximum normalized electric field $\overline{E}_{max}$ at R_b can be written in terms of a_o by using the matching condition eqn. 2.17 and is given by [28] as,

$$\begin{aligned} E_{max} &\propto \frac{e n_e}{\varepsilon_o} R_b \\ \frac{e E_{max}}{m} &\propto \omega_p^2 \frac{\sqrt{a_o}}{k_p} \\ \frac{e E_{max}}{m c \omega_p} &= \overline{E}_{max} = \sqrt{a_o} \end{aligned} \tag{2.22}$$

Using the linear dependence of the electric field and knowing E_{max}, the on axis longitudinal electric field of the wake, $E(z)$, from $z = -R_b$ to $\sim 3/4R_b$, can now be estimated as,

$$E(z)\hat{\mathbf{z}} = E_{max}\frac{z}{R_b}\hat{\mathbf{z}} \tag{2.23}$$

This approximation for longitudinal electric field is shown to agree with that obtained from 3-D OSIRIS particle in cell simulations [28] in the matched self-guided regime. The amount of energy gained by an electron from the longitudinal electric field of the wake can be found by integrating the force, $eE_z(z)$, in space from the back of the wakefield to the center, where $E_z = 0$. While there is a *spike* in the electric field at the back of the wakefield, the amount of energy gained from this feature is small as it only exists over a small region of space. Therefore, because the *useful* accelerating electric field is approximately linear, the average electric field from the back of the wake to the center is equal to $E_{max}/2$. Using this approximation, the energy gained by an electron injected at the back of the wakefield can be approximated as,

$$\begin{aligned}
\Delta E &= e\frac{E_{max}}{2}L_d \\
\Delta E &= e(\sqrt{a_o}\frac{mc\omega_p}{2e})\frac{2}{3}\frac{\omega_o^2}{\omega_p^2}R_b \\
\Delta E &= \frac{2}{3}a_o\frac{\omega_o^2}{\omega_p^2}mc^2 \\
\Delta E(\text{MeV}) &\approx \frac{1}{3}a_o\frac{\omega_o^2}{\omega_p^2}
\end{aligned} \tag{2.24}$$

Equation 2.24 indicates that for a fixed laser frequency and a_o the energy gain will increase as the plasma density is decreased. Energy gain increases with decreasing plasma density because v_ϕ becomes larger at lower plasma densities allowing for a longer dephasing length. However, the matching condition indicates that as the plasma density is lowered, for a fixed a_o the matched spot size must increase.

To keep a fixed laser a_o while increasing the laser spot size, more and more laser power must be used for the self-guiding condition to be valid. Additionally, phenomenological theory indicates that a normalized blowout radius, $k_p R_b$, must be equal to 4-5 for consistent injection and self-trapping of electrons into the first period of the wakefield [28]. This condition dictates that in the matched self-guiding regime, a laser a_o of 4-6.25 must be used to self-trap electrons from the background plasma into the wakefield.

Figure 2.2 a) shows that the matched power for self-guiding rapidly increases as the plasma density is lowered. Additionally it shows that in the matched regime, at a particular density, significantly less power is required to self-guide as the laser a_o is lowered from 4 to 2. Comparing Fig. 2.2 a) and b) it is seen that in order to self-trap electrons at a plasma density of $\sim$2x10^{18} cm^{-3} in order to reach accelerated energies of $\sim$ 1 GeV, a laser a_o of 4 would be needed and would require $\sim$100 TW of coupled laser power within the matched spot size. Currently there are only a handful of laser facilities in the world capable of delivering this amount of power. While an a_o of 4 is required to self-trap background plasma electrons, it has been shown in simulations and experiments that is possible to self-guide a laser pulse and drive a wake over tens' of Rayleigh lengths with $a_o \gtrsim 2$ [20, 28]. Therefore, it is the required laser power to self-trap at low densities that has so far limited the electron energy gain to $\sim$ 1 GeV in LWFA experiments. In this dissertation tunneling ionization was used as a mechanism of injecting electrons into a laser driven wakefields. We will show that injecting electrons in this manner lowers the necessary wake amplitude and thus laser a_o required to trap and accelerate electrons. This injection mechanism can be used to inject electrons at lower laser powers that are sufficient for self-guiding, but not for self-injection. This has allowed for the injection of electrons at plasma densities below 2x10^{18} cm^{-3} enabling energy gains of above 1 GeV [53].

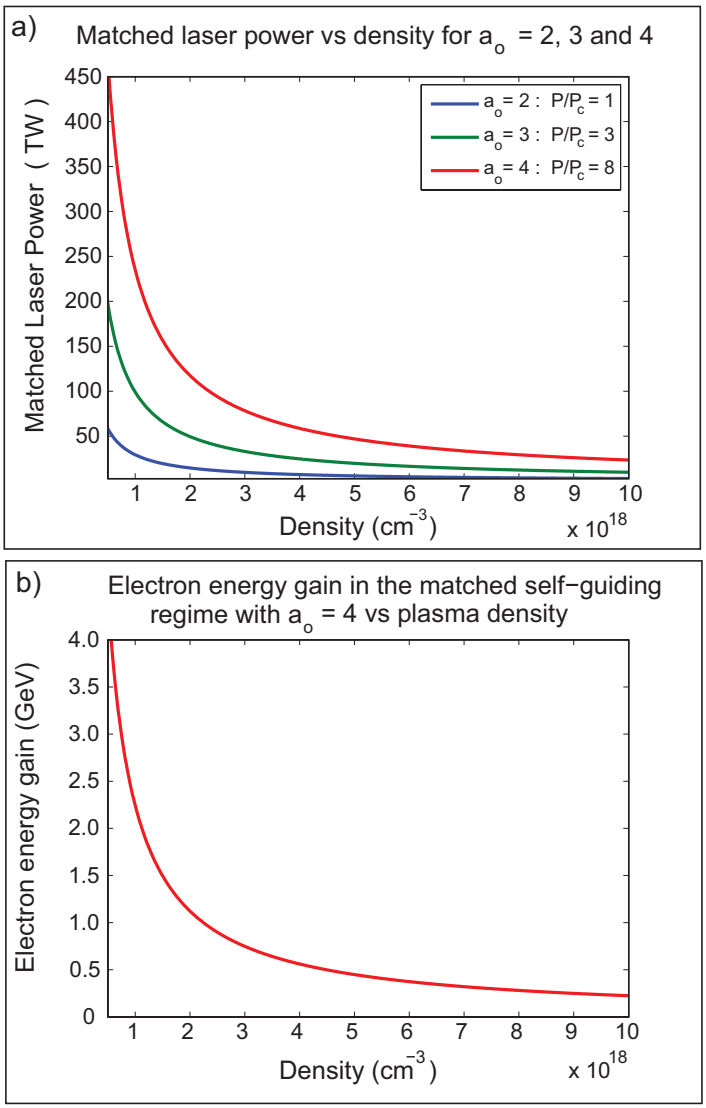

Figure 2.2: a) The power required for self-guiding vs plasma density. The power was calculated using the matched spot size and pulse width at each density for a laser a_o of 2, 3 and 4. Phenomenological theory indicates that in the matched self-guided regime an $a_o \geq 4$ is required for self-trapping. b)The electron energy gain in the matched self-guided regime with an $a_o = 4$ vs plasma density.

CHAPTER 3

Theory and Simulations

3.1 Electron Trapping in 3-Dimensional Wakefields

The trapping of an electron into a LWFA is defined to occur when the electron has gained enough energy from the wakefield to move at the phase velocity, v_ϕ, of the wakefield. Electrons gain energy from the potential Ψ of the LWFA, where Ψ is composed of the scalar Φ and vector potentials A of the wake and laser. A trapping condition can be derived by considering how large a potential difference must be created for an electron to gain enough energy to move at v_ϕ. In this chapter, an analytical theory estimating the wake potential that is required for trapping will be developed. Then, the potential of wakes created in the matched blowout regime will be estimated from simple scaling laws and compared to the required wake potential for trapping. Finally, the analytical potential required for trapping will be compared to the potential difference that trapped electrons experience in 2-D OSIRIS simulations.

In early work an estimated 'wave frame' trapping condition was obtained in 1-D for an externally injected electron into a linear wakefield [22]. This was achieved by recognizing that in the frame moving at the phase velocity of the wake v_ϕ, if the potential Φ becomes as large or larger than the kinetic energy of the injected electron, then the electron can become trapped and oscillate within

the potential of the wake. This trapping condition can be written as,

$$q\Delta\Phi' \geq KE' \tag{3.1}$$

where the $'$ denotes the quantities in the moving frame v_ϕ, q is the charge of the electron and KE is the relativistic kinetic energy of the electron. This condition can also be used to estimate the wake potential required to trap an initially stationary electron injected into the wake, as would be the case for electrons injected via tunneling ionization. An electron born at rest in the frame moving at v_ϕ has a lorentz factor of $\gamma_\phi = (1-(v_\phi/c)^2)^{-1/2}$. Substituting this into eq. 3.1, the trapping condition for an electron can be rewritten as,

$$-e\Delta\Phi' \geq (\gamma_\phi - 1)mc^2 \tag{3.2}$$

where the charge $q = -e$ and m refers to the rest mass of an electron. The scalar potential of the wake can then be transformed into the lab frame, and normalized to give a trapping condition.

$$\frac{e}{mc^2}\Delta\Phi = \Delta\bar{\Phi} \leq \frac{1}{\gamma_\phi} - 1 \tag{3.3}$$

Physically this condition states that when the potential of the wake becomes large enough an electron injected into the wake at rest can gain enough energy to move at the phase velocity of the wake and become trapped.

This trapping condition is valid only in 1-D and does not include the transverse effects of the radial potential. To do this, I will follow a more general approach detailed in Wei Lu's Ph.D. dissertation, which starts with the equation of motion of an electron and utilizes the Hamiltonian of an electron in an electromagnetic field to arrive at a 3-D trapping condition. The momentum of the electron can be related to electric and magnetic fields through the relativistic equation of motion given by,

$$\vec{F} = \frac{d\vec{p}}{dt} = q(\vec{E} + \vec{v} \times \vec{B}) \tag{3.4}$$

where $\vec{p} = \gamma m \vec{v}$ is momentum of the electron and the electric field $\vec{E}$ and magnetic field $\vec{B}$ can be related to the scalar and vector potential $\vec{\Phi}$ and $\vec{A}$ respectively by,

$$\vec{E} = -\vec{\nabla}\Phi - \frac{\partial \vec{A}}{\partial t} \tag{3.5}$$

and

$$\vec{B} = \vec{\nabla} \times \vec{A} \tag{3.6}$$

The Hamiltonian for a charged particle in an electromagnetic field is given by

$$H = \gamma m c^2 + q\Phi \tag{3.7}$$

and is comprised of the kinetic and rest mass energy of the electron and Φ, the scalar potential of the wake and laser. The Hamiltonian represents the total energy of the system. As Lu points out, if the electromagnetic fields do not depend on time, then the Hamiltonian H is conserved i.e. $dH/dt = 0$. In the frame moving at the phase velocity of the wake v_ϕ, the fields of the wake and laser can be approximated as static or time invariant. Therefore in the moving frame, $dH/dt = 0$. Time invariant quantities can be extremely useful, as taken together with boundary conditions can be used to determine important properties of a closed system without explicitly solving for the equations of motion. For this reason, a time invariant quantity is known as a constant of the motion and here will be used to determine a 3-D trapping condition in the stationary or lab frame. While $dH/dt = 0$ in the frame moving at v_ϕ, the Hamiltonian is not lorentz invariant and thus in the stationary lab frame $dH/dt \neq 0$. The time derivative of the Hamiltonian in the lab frame is given by,

$$\frac{d}{dt}H = \frac{d}{dt}\gamma m c^2 + \frac{d}{dt}q\Phi \tag{3.8}$$

Here $d/dt(\gamma m c^2)$ is the rate of change of energy with time and is equal to the power of the electron. Power can be also be written as the dot product of the

velocity and force. Using equations 3.4, 3.5, and the relation of the total time derivative $(d/dt)\alpha = (\partial/\partial t)\alpha + v \cdot \nabla\alpha$, equation 3.8 can be rewritten as

$$\begin{aligned}
\frac{d}{dt}H &= \vec{v} \cdot \frac{d\vec{p}}{dt} + \frac{d}{dt}q\Phi \\
\frac{d}{dt}H &= q\vec{v} \cdot (-\vec{\nabla}\Phi - \frac{\partial}{\partial t}\vec{A} + \frac{\vec{v} \times \vec{B}}{c}) + \frac{d}{dt}q\Phi \\
\frac{d}{dt}H &= q(\frac{d}{dt}\Phi - \vec{v} \cdot \vec{\nabla}\Phi) - q\vec{v} \cdot \frac{\partial}{\partial t}\vec{A} \\
\frac{d}{dt}H &= q(\frac{\partial}{\partial t}\Phi - \vec{v} \cdot \frac{\partial}{\partial t}\vec{A})
\end{aligned} \tag{3.9}$$

This indicates that for non-static potentials in the lab frame $dH/dt \neq 0$, however if a quantity Q can be found such that,

$$\frac{d}{dt}H - \frac{d}{dt}Q = 0 \tag{3.10}$$

then a constant of the motion in the lab frame can be found and used to relate the momentum of the electron to the potentials of the wake and laser. To find such a quantity Q, Lu utilizes the total time derivative of the Canonical momentum, P. The Canonical momentum is the total momentum of the system and is given by

$$\vec{P} = \vec{p} + q\vec{A} \tag{3.11}$$

and is comprised of the momentum of the electron and of the fields of the system. Using the vector identity,

$$\vec{v} \times (\vec{\nabla} \times \vec{A}) = (\nabla\vec{A}) \cdot \vec{v} - (\vec{v} \cdot \nabla)\vec{A} \tag{3.12}$$

the time derivative of $\vec{P}$ can be written as,

$$\frac{d}{dt}\vec{P} = \frac{d}{dt}(\vec{p} + q\vec{A}) = q(\nabla\vec{A} \cdot \vec{v} - \nabla\Phi) \tag{3.13}$$

At this point one can also notice that the fields and potentials of the wake / laser system are approximated to move at a constant velocity v_ϕ and have the form

$\alpha(\vec{r}_\perp, z - v_\phi t)$. Therefore in the direction of the moving frame space and time can be related to one another via v_ϕ and it follows that,

$$(\frac{\partial}{\partial t} + v_\phi \frac{\partial}{\partial z})\alpha = 0 \tag{3.14}$$

Using this relation,$(d/dt)H$ (Eqn. 3.9) can be rewritten as,

$$\frac{d}{dt}H = -qv_\phi(\frac{\partial}{\partial z}\Phi - \vec{v}\cdot\frac{\partial}{\partial z}\vec{A}) \tag{3.15}$$

Multiplying the z component of equation 3.13 by v_ϕ and subtracting this from the time derivative of the Hamiltonian above, a constant of motion is formed and is given by

$$\frac{d}{dt}(H - v_\phi P_z) = 0 \tag{3.16}$$

the argument of this time derivative can be rewritten to give,

$$\begin{aligned}
\text{constant} &= \gamma mc^2 + q\Phi - v_\phi p_z - v_\phi q A_z \\
\text{constant} &= \gamma - \frac{v_\phi}{c}\frac{p_z}{mc} - \frac{e}{mc^2}(\Phi - v_\phi A_z) \\
\text{constant} &= \gamma - \frac{v_\phi}{c}\frac{p_z}{mc} - \frac{e}{mc^2}\Psi \\
\text{constant} &= \gamma - \frac{v_\phi}{c}\frac{p_z}{mc} - \overline{\Psi}
\end{aligned} \tag{3.17}$$

here the a potential Ψ has been defined as $\Psi = (\Phi - v_\phi A_z)$ and has been normalized to e/mc^2. A 3-D trapping condition can now be found by evaluating the constant of motion at the initial condition at which an electron is ionized and at the final condition at which it is trapped. An electron is initially ionized at a potential $\overline{\Psi}_o$ and at rest (i.e. $\gamma = 1$ and $v_z = 0$). The electron is defined to be trapped when it obtains a longitudinal velocity equal to v_ϕ which will occur at some final potential $\overline{\Psi}_f$. Evaluating the constant of motion for the initial injection and final trapped conditions, the potential difference required to trap and electron can be found,

$$1 - \overline{\Psi}_o = \gamma_f - \gamma_f \frac{v_\phi^2}{c^2} - \overline{\Psi}_f$$

$$\begin{aligned} \overline{\Psi}_f - \overline{\Psi}_o &= \gamma_f(1 - \frac{v_\phi^2}{c^2}) - 1 \\ \Delta\overline{\Psi} &= \frac{\gamma_f}{\gamma_\phi^2} - 1 \end{aligned} \tag{3.18}$$

here γ_f is the lorentz factor of the trapped electron. Equation 3.18 is the 3-D trapping condition and indicates the minimum potential difference which must be experienced by the electron in order for it to gain enough energy to move at the phase velocity of the wake and become trapped. As Eqn. 3.18 indicates the normalized potential difference required to trap is inversely proportional γ_ϕ^2. This is because when the wake is moving slowly, γ_ϕ is smaller and electrons need to gain less energy to be trapped. Additionally the required potential difference to trap depends on the γ_f of the electron which is given by $\gamma_f = (1 - \frac{v_{\perp f}^2 + v_\phi^2}{c^2})^{-1/2}$ where $v_{\perp f}$ is the final transverse velocity of the trapped electron. This is where the 3-D nature of trapping is apparent in Lu's derivation. As opposed to 1-D, where the trapping condition only depends on the longitudinal velocity of the electron and wakefield, in 3-D the transverse and longitudinal fields of both the wake and laser are coupled. The coupled nature of the 3-D fields means that the longitudinal electron velocity will be a function of perpendicular electron velocity. This means, as indicated by the dependence of the trapping potential on γ_f, that electrons with larger perpendicular velocities will also have larger longitudinal velocities and thus require a smaller wake potential to reach v_ϕ and become trapped. The lorentz factor of the trapped electron in Eqn. 3.18 can be rewritten using the relativistic equation for total energy,

$$\begin{aligned} \gamma_f^2 mc^2 &= mc^2 + P^2c^2 \\ \gamma_f^2 &= 1 + \frac{\gamma_f^2 v_\phi^2}{c^2} + \frac{\gamma_f^2 v_{\perp f}^2}{c^2} \\ \gamma_f^2(1 - \frac{v_\phi^2}{c^2}) &= 1 + \frac{p_{\perp f}^2}{(mc)^2} \end{aligned}$$

$$\gamma_f = \sqrt{1 + \frac{p_{\perp f}^2}{(mc)^2}}\gamma_\phi \tag{3.19}$$

This equation can in turn be substituted back Eqn. 3.18 such that the trapping condition can be rewritten as function of the final perpendicular momentum of the electron and lorentz factor of the wake [54] given by,

$$\Delta\overline{\Psi} = \frac{\sqrt{1 + \frac{p_{\perp f}^2}{(mc)^2}}}{\gamma_\phi} - 1 \tag{3.20}$$

An electron can gain perpendicular momentum from the transverse focusing fields of the wake, and from the residual energy gain resulting from being tunnel ionized within the laser field. It can be seen that if the final velocity of the electron is made to be purely longitudinal ($v_\perp = 0$) then $p_{\perp f} = 0$ and the 3-D trapping condition Eqn. 3.20 reduces to a the 1-D trapping condition given by Eqn. 3.3.

The relationship between the longitudinal and perpendicular momentum that electrons gain via ionization under the assumption that canonical momentum is conserved was given by Eqn. 3.27. If the electron is created on axis, such that the wake focusing forces are negligible, and the electron is trapped at a location within the wakefield that does not overlap the laser electric field, then the trapping condition can again be rewritten using Eqn. 3.27 as,

$$\Delta\overline{\Psi} = \frac{\sqrt{1 + a_{oi}^2}}{\gamma_\phi} - 1 \tag{3.21}$$

This Eqn. indicates that electrons which were created via tunnel ionization at large initial values of a_{oi} will require a smaller wake potential to become trapped as they gain and retain larger amounts of longitudinal momentum from the $\vec{v}x\vec{B}$ force of the laser electric field. It should be noted that the amount of momentum gained via ionized depends on the phase at which the electron is born within the electric field. As previously discussed, the probability of ionization increases

with electric field strength, which is out of phase with the vector potential A of the laser. Therefore the probability of an electron being created via ionization at a phase where the instantaneous a_{oi} is peaked is considerably lower than the probability of an electron being created where the electric field is peaked and the a_{oi} of the field is small. Nevertheless, the probability of tunnel ionizing over a range of electric field phases is finite and any amount of momentum gained in the longitudinal direction can reduce the necessary wake potential for an electron to be trapped within a wakefield.

Equation 3.18 is an estimate of the potential difference or energy gain required by an electron to move at v_ϕ and become trapped. To determine how much energy an electron actually gains within the first period of wakefield, one can estimate the potential of the wakefield and calculate how much energy an electron gains from the wake in the matched blowout regime.

An electron is accelerated in the direction of laser propagation by the longitudinal electric field created by the charge separation within a wakefield. Therefore the magnitude of the wake potential created depends on the density of the plasma and how large of a charge separation the driver can sustain. In the work discussed here, large laser intensities, with normalized vector potentials $a_o \geq 2$, were used to drive non-linear wakefields in the blowout regime. While the pulse width of the laser electric field was larger than $\lambda_p/2$ in this work, it will be assumed that the matching condition given by Eqn. 2.17 is approximately valid and can be used to estimate the properties of the wakefield which is created. This matching condition is extremely useful in estimating the potential of the wakefield as it relates the vector potential a_o of the driver, to the longitudinal accelerated electric field, through R_b the radius of the spherical wake created. First the normalized potential can be related to the electric field using the relation given by Eqn. 3.14

together with the definition of the electric field given by 3.5,

$$\begin{aligned}
\vec{E} &= -\vec{\nabla}\Phi - \frac{\partial \vec{A}}{\partial t} = -\vec{\nabla}\Phi + v_\phi \frac{\partial \vec{A}}{\partial z} \\
\vec{E} &= -(\frac{\partial}{\partial x}\hat{\mathbf{x}} + \frac{\partial}{\partial y}\hat{\mathbf{y}})\Phi - \frac{\partial}{\partial z}(\Phi - v_\phi A_z)\hat{\mathbf{z}} \\
\vec{E} &= -(\frac{\partial}{\partial x}\hat{\mathbf{x}} + \frac{\partial}{\partial y}\hat{\mathbf{y}})\Phi - (\frac{\partial}{\partial z}\Psi)\hat{\mathbf{z}}
\end{aligned}$$

In the matched blowout regime, the the approximate electric field of the wake in the longitudinal or z direction, is given by Eqn. 2.23. Substituting this into the above equation, the potential difference that an electron experiences and it travels back through the wake can be solved as,

$$\begin{aligned}
(\frac{\partial}{\partial z}\Psi)\hat{\mathbf{z}} &= (-E_z)\hat{\mathbf{z}} \\
\Delta\Psi &= -\int_{z_i}^{z_f} E_{max}\frac{z}{R_b}d_z
\end{aligned} \tag{3.22}$$

where z_i and z_f refer to the longitudinal location at which the electron is injected and trapped, respectively. Since the longitudinal electric field of the wake is approximately linear, the potential of the wakefield will be approximately parabolic in shape.

To develop a physical picture of the trapping process, one can view the potential of the wakefield as a symmetric parabolic potential well as is the case for a linear wake. Injected electrons can be thought to be dropped into the potential well with some initial velocity. Because the well is symmetric, electrons injected in the front half of the well, at some initial location $z = z_i$, and some initial potential $\Psi = \Psi_i$, will roll down and back up through the well to a location $z_2 = -z_i$ and where the electron will again be at the initial potential Ψ_i it was injected at. Now if the remaining potential difference, $\Delta\Psi$, between the top of the potential well, where $\Psi = \Psi_{\max}$, and Ψ_i is greater than the initial kinetic energy of the

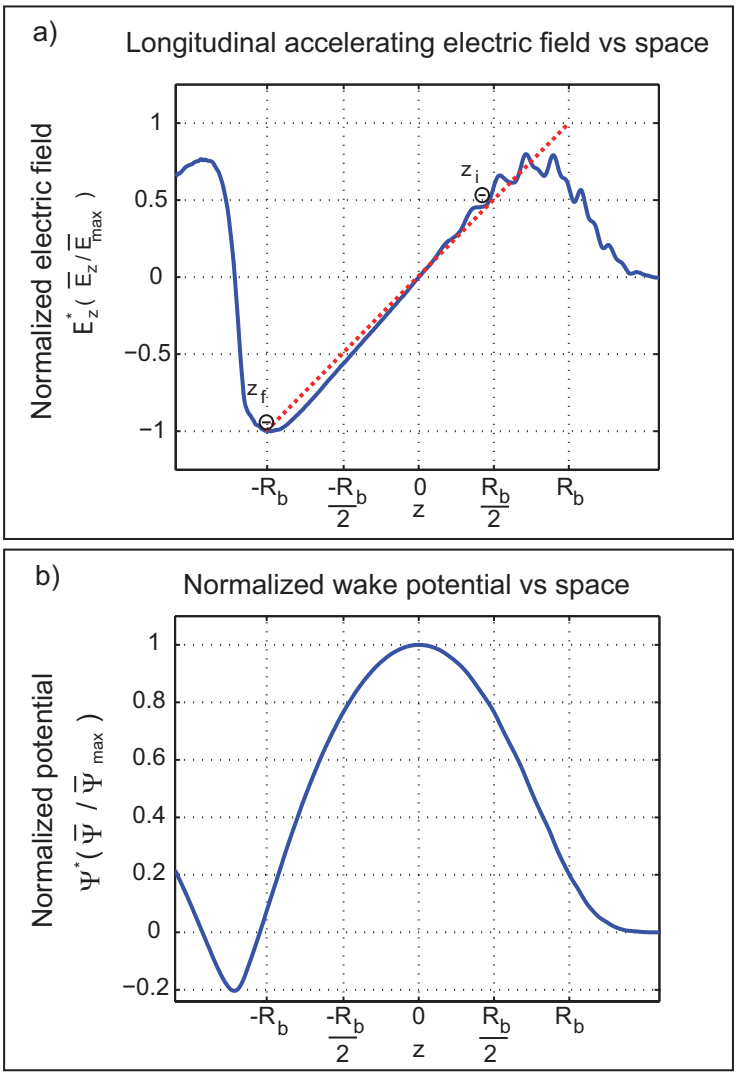

Figure 3.1: a) The on axis longitudinal electric field of a wake vs z location. The dashed red line indicates that the electric field can be approximated as linear from $\sim -R_b$ to $3/4R_b$. The circles represent an electron that has been tunnel ionized and injected by the laser field at a location z_i and trapped by the wakefield at a location z_f. b) The normalized wake potential plotted vs space.

injected electron, then the electron will be trapped within the well. From this physical picture it can been seen that electrons which are injected at the very front of the symmetric well with some initial velocity will never be trapped, as the $\Delta\Psi = 0$. It can also be seen that injecting electrons closer to the bottom of the potential well increases the $\Delta\Psi$ between the injection location and top of the well and thus increases potential difference which is available to trap the electron.

Before continuing on with the discussion of dynamics of ionization injection and trapping, a brief aside will be taken to qualitatively discuss self-trapping. From the aforementioned physical picture of a symmetric potential well, it was argued that electrons which are injected at the very front of the potential well, as is the case for self-trapped electrons, will never experience a sufficient potential difference to become trapped. The question then to answer is, how does self-trapping occur and what are the dominant mechanisms that cause it? Two conditions or events are required for self-trapping to occur. Firstly, the normalized potential difference that an electron experiences must be sufficient to accelerate it to the phase velocity of the wakefield. This required potential difference was analytically estimated to be $\Delta\overline{\Psi} \approx -1$. Secondly, the trapped electron must some how be injected into this potential well.

Figure 3.1 shows the on axis longitudinal electric field and potential of a wakefield. The wake was created in the matched self-guiding regime by a laser pulse with an $a_o = 2$ and a matched spot size and pulse width of 4.42 μm and 15 fs, respectively.. The fields shown in this figure were generated from a 2-D OSIRIS simulation and have been normalized to their respective maximum values. If a symmetric potential cannot trap an background plasma electron, then it follows that in order for an electron to gain energy and become trapped, the longitudinal accelerating field and potential cannot be symmetric. Figure

3.1 b) shows that the wake potential is not symmetric as it dips below zero at the back of the wake at $z \approx -R_b$. Electrons injected at the front of the wake, $z > R_b$, can gain energy from this dip in potential at the back of the wakefield. If electrons can gain enough energy such that $\Delta\overline{\Psi} = -1$ then they will be trapped. In the matched blowout regime, the laser ponderomotive force pushes out all the electrons within a matched matched spot size. These electrons are pushed together forming a dense sheath around the spherical ion bubble. As these sheath electrons return back and cross the laser axis at the back of the wakefield, they create the dip in the potential at $z \approx Rb$. It is this the dip in the potential, that is associated with the sheath of electrons, which provides the necessary potential difference to self-trap electrons from the background plasma. The phenomenological theory developed by Lu. et al., indicates that such a potential difference for self-trapping exists when a large nonlinear plasma with normalized blowout radius of $k_p R_b = 4 - 5$. The magnitude and shape of the dip in the potential is proportional to the sheath thickness and density which in turn is dependent on how strongly the wake is driven. Theories which do not accurately model the contribution to the potential from the sheath result in an un-physical trapping condition, where the normalized blowout radius of the wake must equal γ_ϕ of the wakefield [55]. While the evolution of the wake radius can trigger self-injection [35, 37], trapping theories [56] which are derived from inaccurate descriptions of the wake and require evolving wakefields for self-trapping to occur should not be considered strictly accurate. Simulations using non-evolving beam drivers and wake potentials have shown that electrons can be self-trapped into the wakefield [57]. The exact shape and magnitude of the dip in the potential at the back of the wake field is sensitive to the wake and driver shape and evolution making an exact threshold for self-trapping which depends only on laser a_o or P/P_c difficult. However in many experiments and

simulations, preformed over a range of nearly matched laser parameters, self-trapping of background plasma electrons has been achieved with an ultrashort laser pulses, with an $a_o \gtrsim 4$ with a $P/P_c > 3$ [58, 59, 60].

As previously mentioned, for trapping to occur, an electron must be able to experience or be injected into the potential of the wakefield. In the blowout regime, all of the electrons within the matched spot size of the laser are pushed out by the ponderomotive force of the laser, leaving behind a bare ion bubble. The pushed out electrons initially pile up around the envelope of the laser pulse forming the previously mentioned dense electron sheath, before returning and crossing the laser axis roughly a plasma period later. As electrons return back to the laser axis, some the electrons which either originate further from the axis, or were pushed outwards earlier in the laser pulse, cross the sheath. It is these electrons which are injected into the wake and can experience the required potential to be trapped. An analytic model for the radial electron trajectory response to a relativistic beam driver is detailed in Lu's thesis [61]. The model shows that electrons with a larger initial distance from the driver axis are the ones which *cross* trajectories are end up being injected into the wakefield.

3.2 Tunnel Ionization Injection of Electrons into a LWFA

To understand how tunneling ionization can be used to inject electrons into a wake the process of tunneling ionization in the context of the work preformed here will first be discussed.

Ionization is the process of separating a bound electron from the positively charged nucleus of an atom. A laser pulse can ionize the atoms or molecules in a neutral gas in a number of ways, but in the experiments and theory discussed

here the focus will be on tunneling ionization. Tunneling ionization occurs when the laser pulse is intense enough to perturb the bound electron such that its atomic orbit is modified. When this occurs the binding potential between the electron and positively charge nucleus is lowered to a point where the probability of an initially bound electron *tunneling* through the potential well to become free becomes large. In this work, this process not only creates the plasma, but also is the mechanism that injects electrons into the wakefield.

There are several analytical tunneling ionization models, but here the Ammosov-Delone-Krainov, or so called ADK model will be used [62]. As shown by Bauer and Mulser [63] and discussed by Bruhwiler et. al [64], the ADK model has be shown to give good agreement with the time dependent Schrödinger equation, when modeling the effects of an external electric field superimposed on top of the columbic potential of a hydrogen atom. The agreement between the two models was found to be good as long as the applied electric field remains below a critical value,

$$\mathrm{E_{crit}} = (\sqrt{2} - 1)[\zeta_i]^{3/2} \tag{3.23}$$

where ζ_i is the unperturbed ionization potential of the electron. Here $\mathrm{E_{crit}}$ and ζ_i are in atomic units; the following conversions for the electric field and ionization potential used in eqn. 3.23 are 5.14x10^{14} V/m and 27.2 eV respectively and have been taken from reference [64]. While the time dependent Schrödinger equation gives a much more exact answer, it quickly becomes intractable when modeling atoms with multiple bound states. The ADK model allows a prediction of the ionization rate for atoms with multiple ionization states as long as the applied electric field is less than $\mathrm{E_{crit}}$ for the ionization state of interest. In this work the rate at which electrons are ionized from the K-shell of nitrogen is of particular interest. To ensure that the ADK model can be used to accurately describe the

results, the maximum electric field used to ionize K-shell electrons must be lower than E_{crit}. The maximum electric field that was used in this work can be found from the measured cycle averaged intensity using the relationship,

$$I_{avg} = \frac{1}{2}\frac{E^2}{\mu_o c} \tag{3.24}$$

where μ_o is the magnetic susceptibility and c is the speed of light. The maximum electric field then for the maximum average intensity that was used ($\sim 1.3\text{x}10^{19}$ W/cm^2) is 9.98x10^{12} V/m.

Species	Z	Ionization Potential (eV)
N^{1+}	1	14.53
N^{2+}	2	26.60
N^{3+}	3	47.45
N^{4+}	4	77.47
N^{5+}	5	97.89
N^{6+}	6	552.06
N^{7+}	7	667.03
He^{1+}	1	24.58
He^{2+}	2	54.42

Table 1: Ionization potentials for nitrogen and helium.

As shown in Table 1, the 6th electron of nitrogen has an ionization potential of 552.057 eV and the critical electric field for this state is 19.5x10^{12} V/m as given by eqn. 3.23. This is almost twice as large as the maximum electric field used

and indicates that the ADK model can be used to predict the ionization rates in the work presented here.

The ADK ionization probability rate depends on the magnitude of the applied electric field, the ionization potential of state, and the effective principle quantum number, and is given by

$$\mathrm{W}(\mathrm{s}^{-1}) \approx 1.52\mathrm{x}10^{15}\frac{4^{n^*}\zeta_i(\mathrm{eV})}{n^*\Gamma(2n^*)}\left(20.5\frac{\zeta_i^{3/2}(\mathrm{eV})}{E(\mathrm{GV/m})}\right)^{2n^*-1}\exp\left(-6.83\frac{\zeta_i^{3/2}(\mathrm{eV})}{E(\mathrm{GV/m})}\right) \tag{3.25}$$

where Γ is the standard gamma function and $n^* \approx 3.69\mathrm{Z}/\zeta_i^{(1/2)}$ is the effective principle quantum number, with Z being the ionization state level. The fraction of the neutral state which is ionized is given by $\mathrm{W}\Delta\mathrm{t}$, where $\Delta\mathrm{t}$ is the amount of time the field is on.

Using the ADK ionization probability rate, the fraction of neutral nitrogen gas that is ionized as a function of time using a Gaussian laser pulse with a peak average intensity of $1.3\mathrm{x}10^{19}$ W/cm^2, a central wavelength of 815 nm and a 45 fs pulse width (full width half maximum (FWHM) of the intensity) can be modeled. As shown in Fig. 3.2 the large step in ionization potential between N^{5+} and N^{6-7+} leads to a large step in space / time between the ionized states. This step allows electrons from N^{6-7+} to be created near the peak of the electric field. The magnitude of the ionization potential as well as the pulse width and size of the electric field of the laser can be used to control the relative location within the laser electric field at which electrons are created. It is this feature of ionization which can be exploited to inject electrons directly into a wakefield.

Figure 3.3 illustrates how tunneling ionization can be used to inject electrons into a LWFA. The wakefield is excited in a plasma created from a gas or a gas mixture that has multiple ionization states. Experiments reported here were carried out in a mixture of helium and trace amounts of nitrogen gas, although it

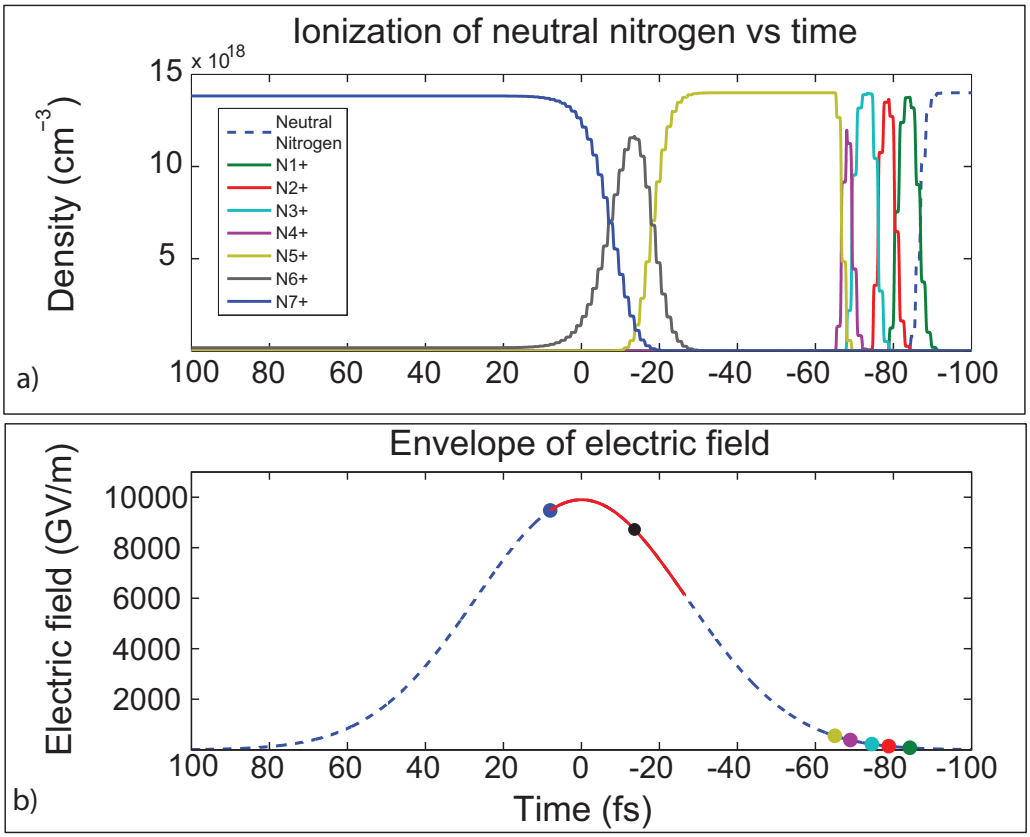

Figure 3.2: a) The density of each ionized state of nitrogen vs time calculated using the ADK model. The ionization rate was calculated for a Gaussian laser pulse with a peak average intensity of 1.3x10^{19} W/cm^2 and a pulse width $\tau_{fwhm} = 45$ fs. The neutral density of nitrogen was 1.4x10^{19} cm^{-3}. The envelope of the laser electric field is shown by the dashed line in frame b). The colored circles correspond to the time / location at which the maximum density of a particular ionized state of nitrogen is reached. The red line indicates the range of times over which electrons from N^{6-7+} are created. The large step in ionization potential between N^{1-5+} and N^{6-7+} creates a large step in time / location between the species allowing electrons from N^{6-7+} to be born near the peak of the field.

may be desirable to use other trace atoms with multiple ionization states depending on the plasma density and laser conditions that are used. As Fig. 3.3 a) indicates, the leading edge of the ultra-short laser pulse is intense enough to fully ionize helium atoms and the outer five electrons of nitrogen. The ponderomotive force of the laser pushes out these electrons, creating a wake. There is a large difference between the ionization potential (IP) and thus the ionization appearance intensity of the 5th (L shell) electron that produces N^{5+} (IP 98 eV) and the two K-shell electrons that produce N^{6+} and N^{7+} (IP 552 and 667 eV respectively). This step in the ionization potential can be matched to the laser intensity profile and the plasma density, such that the 6th and 7th nitrogen electrons are tunnel ionized by the electric field of the laser and injected into the electric field of the fully formed wake, as shown in Fig. 3.3 b). These ionized electrons appear at rest and slip backwards relative to the laser pulse and the wake. If they gain enough energy from the longitudinal electric field (E_z) of the first period of the wake such that they reach the phase velocity of the wake v_ϕ, they are trapped and will gain additional energy as they now move forward with respect to the wake. The amount of energy necessary for an electron to be trapped by the potential of the wake will be examined using theory and simulations in the next chapter. Additionally it can be seen from Fig. 3.3 c) that the potential of the wakefield varies with the location or phase of the wake, and that the maximum potential occurs at the middle of the wake where the accelerating electric field is zero. In the next chapter the theory behind trapping electrons into LWFA will be discussed in detail and the benefit of injecting electrons via ionization into the wakefield at large initial potentials will be explained.

Electrons also gain energy directly from the laser field as a consequence of being tunnel ionized. This effect, known as Above Threshold Ionization (ATI) has been widely studied with experiments and simulations [65, 66, 67, 68, 69].

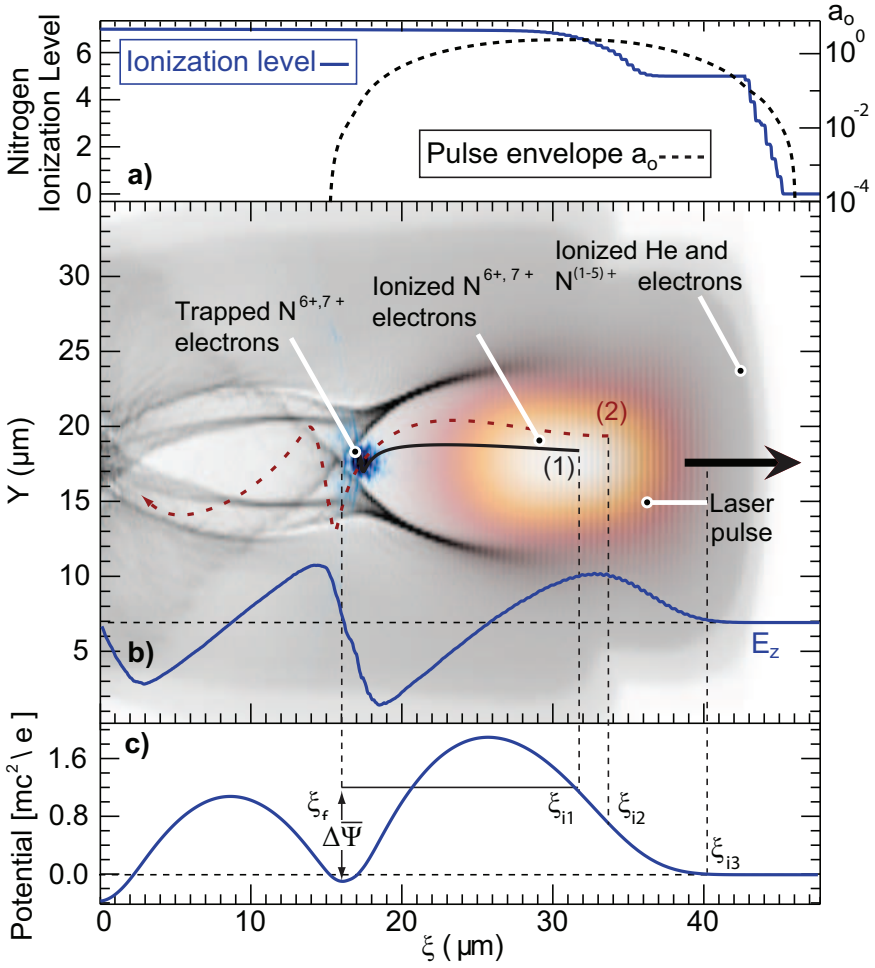

Figure 3.3: OSIRIS simulation of the injection of tunnel ionized electrons ($n_e = 7 \times 10^{18}$ cm^{-3}; $a_0 = 2$). As the laser pulse propagates to the right it ionizes a 9:1 mix of He and N_2 and drives a wake. a) The envelope of the a_o of the laser (dashed line) and the ionization state of nitrogen atoms (solid line) on axis. The superimposed trajectories (1) and (2) in frame b) represent simulation electrons ionized into the wake from the K-shell of nitrogen. Electron (1) is ionized close to the axis and is trapped by the wakefield, while electron (2), ionized earlier and off-axis, is not trapped. The solid line labeled E_z refers on axis longitudinal electric field of the wake. (c) The normalized wake potential $\bar{\Psi}$ on axis, with particular points relevant to the physics of trapping depicted.

The energy that electrons gain from the electric field of the laser is given by,

$$\text{Energy} = \int \vec{v} \cdot \vec{E} dt \tag{3.26}$$

Electrons gain momentum in the perpendicular direction (in the direction of the electric field polarization) from the electric field, as well as in the longitudinal direction (in the direction of the laser propagation) due to the $\vec{v}X\vec{B}$ force. Electrons will have a large range of energies corresponding to the phase within the field at which they were ionized. As shown by [68] if the longitudinal electric field of a focused laser pulse is much smaller than the electric field in the perpendicular direction of polarization, then the energy that electrons gain from ionization can be estimated by approximating the laser pulse as a plane wave. In this case, canonical momentum is conserved and the relationship between the longitudinal and perpendicular momentum has been derived as, [65, 66]

$$p_z = \frac{p_\perp^2}{2mc} \tag{3.27}$$

and are ejected from the focus of the laser pulse at an angle of,

$$tan\theta = \sqrt{\frac{2}{\gamma - 1}} \tag{3.28}$$

where θ is the angle between the direction of laser propagation and polarization. Since canonical momentum is conserved, the final perpendicular momentum of the electron after it has left the field can be related to the initial vector potential at which it was ionized. In this manner eqn. 3.27 can be rewritten in terms a_{oi}, the normalized vector potential at which the electron is ionized as,

$$\frac{p_z}{mc} = \frac{a_{oi}^2}{2} \tag{3.29}$$

It should be noted that a_{oi} is the instantaneous normalized vector potential, meaning that it depends on the exact phase within the vector potential A the

electron is created. 2-D OSIRIS simulations using the ADK ionization model have been preformed to examine the energy that electrons from N^{6-7+} gain from ATI using a laser spot size, pulse width and intensity similar to what has been used experimentally. The simulations where done at low plasma densities (10^{10} cm^{-3}) to ensure that accelerating fields created within the plasma were small and did not influence the results. The angle at which electrons from N^{6-7+} are ejected, as well as the energy that they gain from ATI where found to be in good agreement with that predicted equations 3.27 and 3.28. As will be discussed later, the longitudinal momentum gained in the direction of laser propagation can aid with the trapping of electrons into a LWFA.

3.3 The Trapping of Electrons Injected via Tunnel Ionization into a LWFA in the Blowout Regime

While self-trapped electrons originate from outside of the wake, as previously discussed, due to the large step in ionization potential, electrons can be tunnel ionized and injected directly into the accelerating wakefield. As mentioned above, electrons injected at locations close to the center of a potential well can gain a relatively larger amount of energy than electrons injected further from the center. As will be seen, using the linear approximation of the wake, the amount of available wake potential for electron electrons which have been injected into the wakefield far exceeds $\Delta\overline{\Psi}$ required for trapping. Therefore, even thought the linear approximation of the field does not correctly model the electron sheath, it can still be used to accurately model the dynamics of trapping electrons which are injected into the wakefield.

To estimate the potential difference that an injected electron experiences,

consider an electron that is tunnel ionized on axis, appearing at longitudinal location z_i and being trapped at the back of the wake where $z_f = -R_b$ as shown in Fig. 3.1. The range of initial injection locations over which the approximation for the longitudinal electric field is valid, is from $-R_b$ to $3/4R_b$. The initial injection location can be defined as $z_i = \alpha R_b$, where α can vary from -1 to $3/4$. Integrating Eqn. 3.22 from $-R_b$ to z_i, and using the matching condition given by Eqn. 2.17, the approximated normalized potential difference that the electron experiences as a function of a_o is given by,

$$\begin{aligned} \Delta\Psi &= (\frac{E_{max}}{R_b})\frac{1}{2}(\alpha^2-1)R_b^2 \\ \Delta\Psi &= (\frac{mc^2 k_p\sqrt{a_o}}{e})R_b\frac{1}{2}(\alpha^2-1) \\ \frac{e}{mc^2}\Delta\Psi &= k_p\sqrt{a_o}(\frac{2\sqrt{a_o}}{k_p})\frac{1}{2}(\alpha^2-1) \\ \Delta\overline{\Psi} &= -a_o(1-\alpha^2) \end{aligned} \tag{3.30}$$

recall that here $\alpha = z_i/R_b$. Notice that because $z_f = -R_b$, Eqn. 3.30 is really indicating the maximum potential difference that is available to an injected electron within the first period of the wake. The maximum available normalized potential difference that an electron experiences as a function of the initial injected location and laser a_o (wake amplitude) is shown in Fig. 3.4.

The solid horizontal line in Fig. 3.4 corresponds to a $\Delta\overline{\Psi} = -1$, which is the approximate potential difference required to trap an electron. As shown in Fig. 3.4, electrons injected near the very back (or very front) of the wake close to $\pm R_b$, will not gain enough energy to experience $\Delta\overline{\Psi} = -1$, and thus will not be trapped. However, Fig. 3.4 indicates, that over a large range of z_i the $\Delta\overline{\Psi} < -1$, indicating that trapping of electrons will occur over a larger range of injection locations even for relatively small $a_o = 2$. Therefore injecting electrons into the wakefield, can increase the potential difference that is available for electrons to be trapped. The

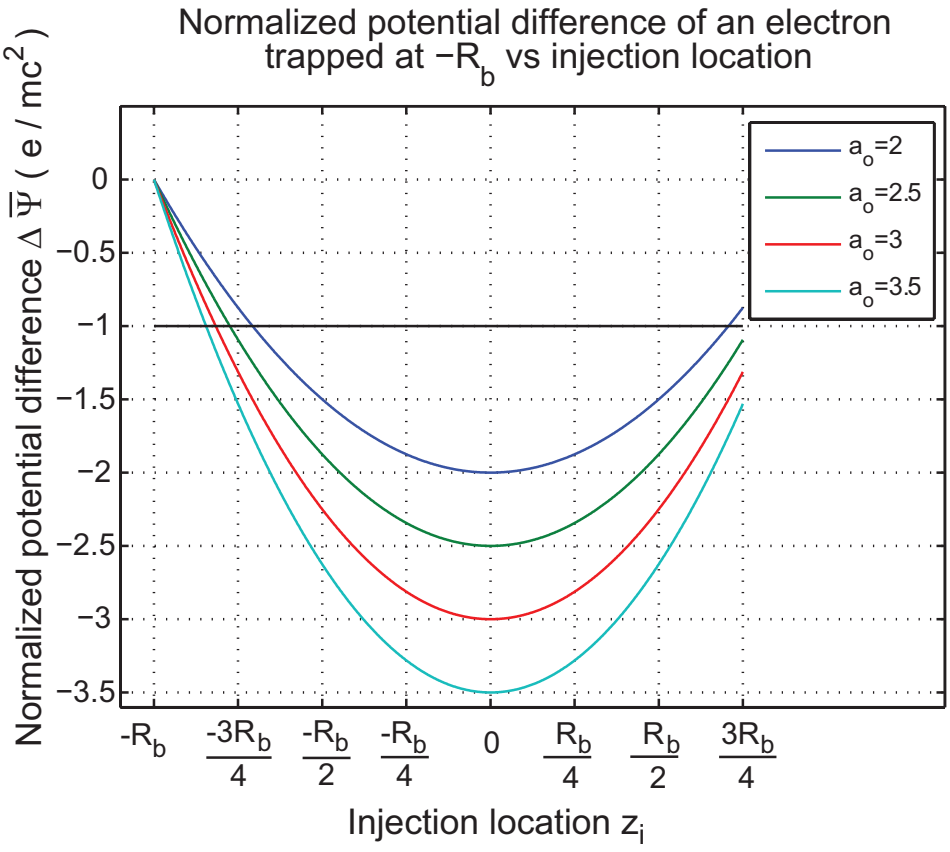

Figure 3.4: The on axis normalized potential difference $\Delta\overline{\Psi}$ in the matched blowout regime vs initial injection location z_i for an electron trapped at $-R_b$. The solid horizontal line at $\Delta\overline{\Psi} = -1$ corresponds to the approximate potential difference required to trap.

optimal location for injection is at the middle of the wakefield ($z = 0$) where the electric field of the wake is 0. This is because electrons injected at this location only experiences the accelerating phase of the wake. Injection of electrons into the wakefield allows electrons to gain enough energy to be trapped using smaller absolute wake amplitudes than are required for the self-trapping of electrons that originate from outside the wake. For example, from Eqn. 3.20, it is seen that a normalized potential difference required for trapping is given as $\Delta\overline{\Psi}_{REQ} \lesssim -1$. Equation 3.30 and Figure 3.4 indicate that for an $a_o = 2$, an electron injected at $z_i = R_b/2$ will experience a $\Delta\overline{\Psi} = -1.5$. This is less than $\Delta\overline{\Psi}_{REQ}$ meaning that the electron will gain enough energy from the wake to be trapped within the first period of the wake. The self-trapping of electrons for a matched laser pulse with an $a_o = 2$ is not expected as $k_p R_b < 4 - 5$. By tunnel ionizing electrons directly into the wakefield, lower wake amplitudes, driven by lower intensity lasers, can be used to trap electrons. This can be achieved while remaining in the matched blowout regime allowing self-guiding and electron trapping to be achieved at lower plasma densities using a laser $a_o < 4$. As Fig. 2.2 indicates, this reduction in laser a_o will reduced the amount of laser power necessary to trap an accelerate electrons to energies greater than ~ 1 GeV.

As Fig. 3.4 indicates over a large range of laser and injection parameters, the approximated $\Delta\overline{\Psi}$ that the electron experiences from the wake upon reaching $-R_b$ is less than -1. This indicates that the electron will gain enough energy to be trapped before actually reaching $z = -R_b$. This will reduce the dephasing length and final energy gain of the electron. Using Eqn. 3.22 and assuming that $\Delta\overline{\Psi} = -1$ at the location where the electron is trapped, z_f can be solved as a function of z_i as,

$$z_f = R_b \sqrt{\frac{z_i^2}{R_b^2} + \frac{1}{a_o}} \tag{3.31}$$

Using the average accelerating electric field of the wake and using z_f to calculate the dephasing length, the electron energy gain from the wakefield as a function of initial injection location, z_i and laser a_o is given by,

$$\Delta E = \frac{2}{3} a_o \frac{\omega_o^2}{\omega_p^2} \left(\sqrt{\frac{z_i^2}{R_b^2} + \frac{1}{a_o}} \right) mc^2$$

$$\Delta E(\text{MeV}) \approx \frac{1}{3} a_o \frac{\omega_o^2}{\omega_p^2} \sqrt{\frac{z_i^2}{R_b^2} + \frac{1}{a_o}} \tag{3.32}$$

To illustrate this effect on the final accelerated energy, Eqn. 3.32 has been plotted for as a function of z_i and a_o at a plasma density of 1.4x10^{19} cm^{-3} in Fig. 3.5. As indicated by Eqn. 3.32 and Fig. 3.5 electrons which have been injected via ionization at locations further from the center of the wake ($z_i = 0$) gain more energy. This is because an electron injected at z_i will first be decelerated from z_i to $z = 0$ and then be accelerated from $z = 0$ to $z = -z_i$. In a symmetric potential, the electron will gain no energy as it moves from z_i to $-z_i$. Therefore the dephasing length for these electrons will depend on $|z_i|$ plus some additional length, z_{add}, that it takes the electron to gain enough energy to turn around and move at v_ϕ, whereas the dephasing length that electrons injected at the center of the wakefield will only depend on z_{add}. Electrons injected closer to the center of the wakefield will have smaller dephasing lengths and therefore smaller total energy gains than electrons injected further from the center which have larger dephasing lengths.

From the scaling laws describing the wake size and maximum electric field, it has been shown that the wake potential that exists in the matched self-guided regime is greater than the analytically estimated required potential for an electron to be trapped ($\Delta\overline{\Psi} \approx -1$) over a wide range of injection locations. Additionally, it was found that the location at which an electron is ionized into the wakefield determines the maximum energy gain for that electron.

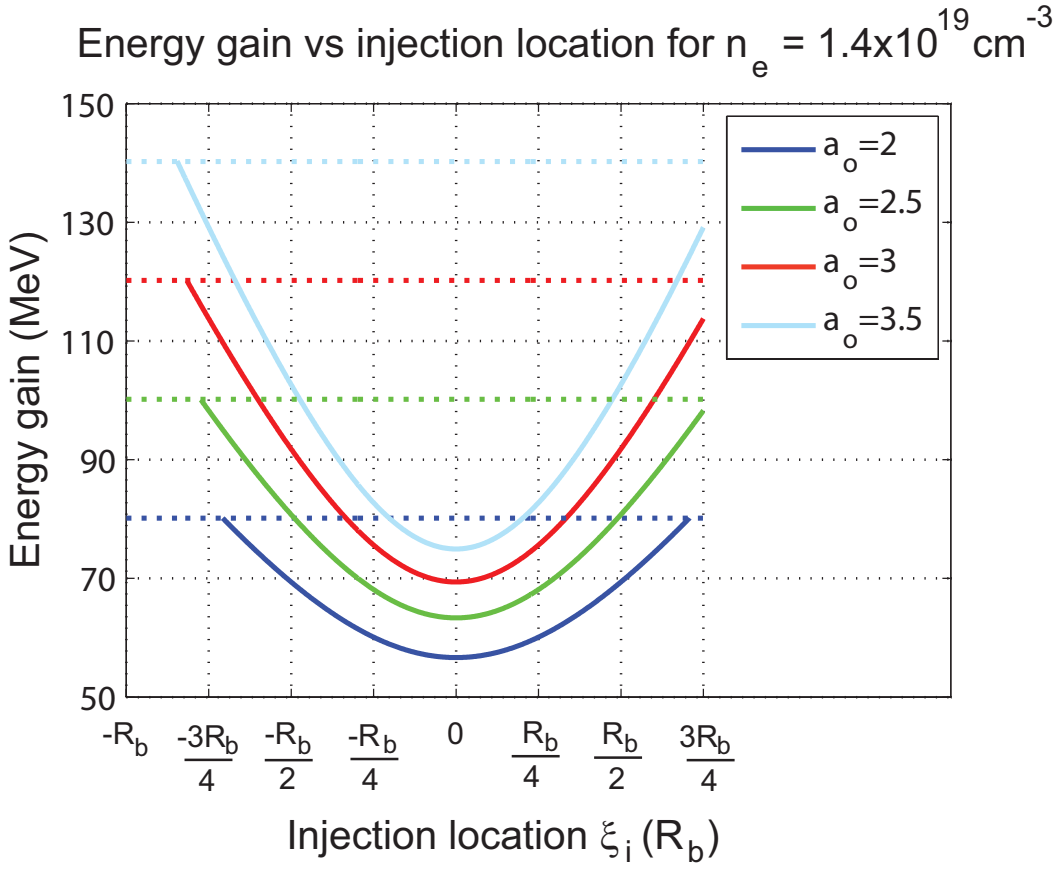

Figure 3.5: The energy gained by an electron vs initial injection location and laser a_o. The solid colored lines indicate that an electron injected closer to the middle of the wakefield ($z_i = 0$) gains less overall energy, due to having a shorter dephasing length than an electron injected further from the center of the wake. The dashed horizontal colored lines indicate the approximated maximum energy gain ($z_f = R_b$) as given by Eqn. 2.24.

To study the trapping process in more detail, 2-D OSIRIS simulations, which included the ADK model of ionization, were preformed. The dynamics of ionization injection paticulary which electrons are trapped and which are not trapped was first examined. Then a comparison between the estimated required potential difference and the simulated potential difference observed for trapping was made. Both of these investigations were made through tracking the trajectories of electrons created from the N^{6-7+} ionized states.

To start, a 2-D simulation with similar laser and plasma parameters to the experiment was preformed, with a laser $a_o = 2.5$, pulse width of 45 fs (FWHM of the intensity), and a spot size (1/e of the electric field) equal to 4.5 μm. The plasma density profile was a 2 mm long slab, with a uniform density of $1.4\text{x}10^{19}$ cm^{-3} and initially the laser was polarized out of the plane of the simulation. A ratio of 90:10 percent helium to nitrogen gas was used. In the simulation, the electron density could be split into the contributions from three species: electrons originating from He^{1-2+}, N^{1-5+} and N^{6-7+} ionized states respectively. In this manner, it was possible to isolate the properties of electrons from a particular group of ionization states. The properties of electrons from each species, which include position, momentum and energy are saved by the simulation. In this work these properties were saved every $\sim$ 1000 time steps or every $\sim$ 25 μm. To maintain tractable file sizes, a *cut* is usually placed on this *raw* data. In this simulation work, the properties from a random sample of 10% of the total electron density from N^{6-7+} was recorded. From this sample of electron density, it is then possible to select of group of $\sim$ 300-500 electrons and track their properties for every time step of the simulation. This enables one to make a detailed study of the behavior of injected electrons from N^{6-7+}.

Figure 3.6 shows a small sample of the trajectories of electrons just from the

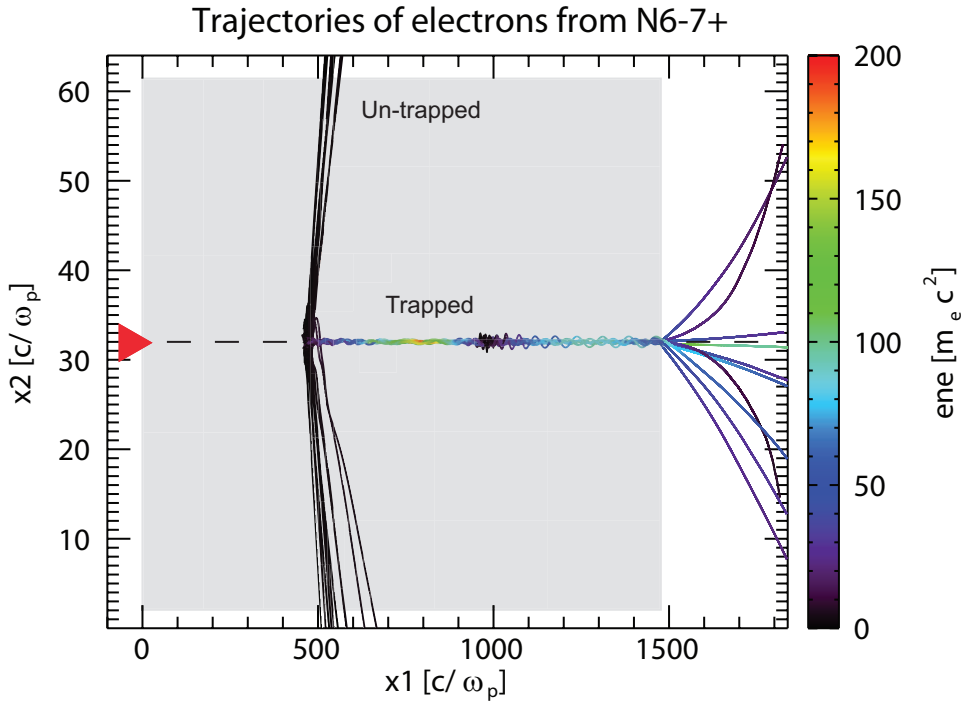

Figure 3.6: Trajectories of a group of electrons from N^{6-7+} plotted vs space in the stationary lab frame. These electrons have all been ionized over a small range of space / time centered around $\sim$ 452-467 (c/ω_p) or 402-414 ($1/\omega_p$) respectively. The color of the electron trajectory corresponds to the energy gained from the wakefield. A portion of electrons are trapped, and remain on axis while gaining energy. The rest of the electrons are not trapped into the wake and immediately after being created leave the laser / wake axis at a large angle. Trajectories corresponding to electrons which are not trapped into the first bucket are not shown to simplify the physical picture. The grey area corresponds to the 2 mm long slab neutral gas profile. The laser, denoted by the red triangle, is focused on to the edge of the gas profile. The laser axis is shown by the dashed line.

N^{6-7+} ionization states plotted vs space in the laboratory frame. These trajectories were created from the previously mentioned simulation parameters. This figure shows that there are two groups of electrons. One that becomes trapped within the wakefield and remains on axis while gaining energy and another group of electrons that are not trapped and leave the laser / wake axis at large angles. One of the first questions that can be addressed with this simulation data is: Which electrons are trapped and why do they become trapped?

As Fig. 3.4 indicates, a larger potential difference is available to those electrons created closer to the center of the wakefield electrons ($z_i = 0$) and can allow for them to be trapped, while electrons born further from the center will not experience a sufficient potential difference to be trapped. From the electron trajectory data, the initial location at which trapped and un-trapped electrons are injected via ionization is known. For this particular group of tracked electron trajectories, electrons are created and trapped over a range of locations and times between 452-467 c/ω_p (642-663μm) and 402-414 1/ω_p (1.9056-1.9625 ps) respectively. As shown in Fig. 3.7 a), the longitudinal electric field and thus the wake potential is approximately quasistatic over the range of space and times that electrons are injected and trapped. Since the wake potential is quasistatic, the relative location and initial potential at which trapped and untrapped electrons are injected into the wake can be plotted and compared. As shown in Fig. 3.7 b), the electrons from the N^{6-7+} ionized states which are trapped, shown as green circles, are the electrons which are injected further back in the wakefield at larger initial normalized potentials, while the un-trapped electrons, shown in red, are the electrons born further forward in the wakefield at with smaller initial potentials (see Fig. 3.1). This result confirms that the most important parameter in determining whether or not an injected electron will be trapped, is the initial injection location within the wakefield. It is this injection location which

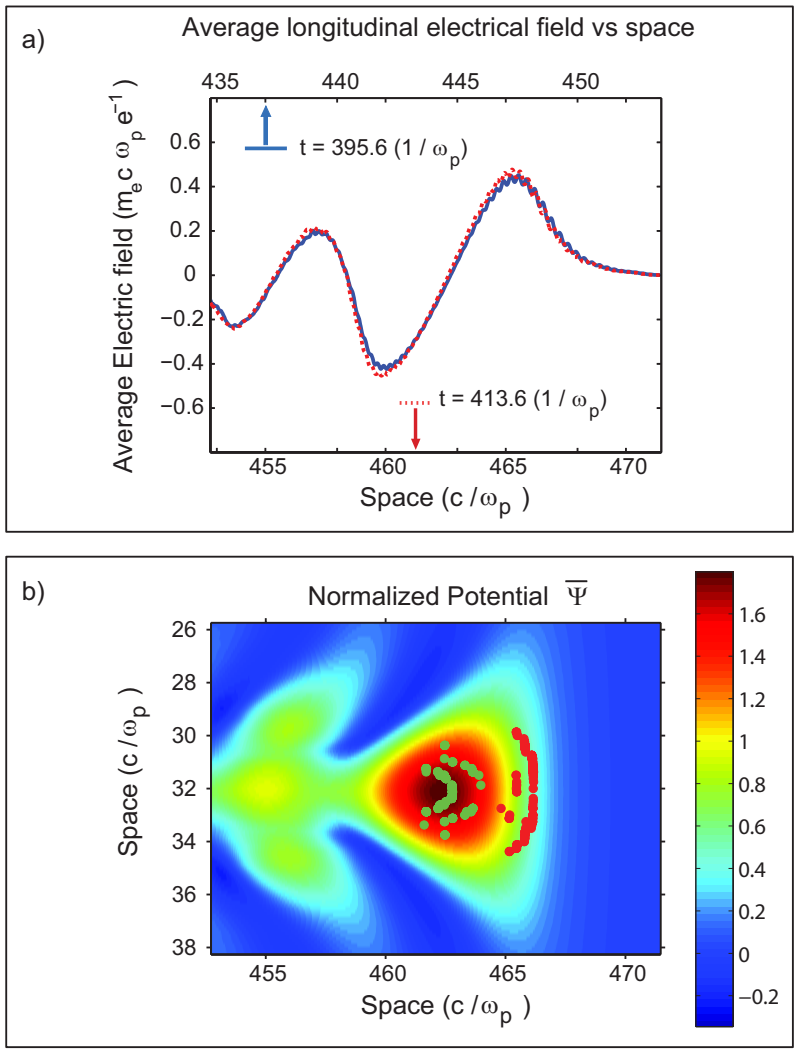

Figure 3.7: a) The longitudinal electric field of the first period of the wake, averaged transversely in space over 5.7 μm. The solid line corresponds to the electric field at a time $\sim$395 $1/\omega_p$ where ionization of the tracked particles begins, while the dashed line is the electric field at a latter time when the majority of the tracked electrons have been trapped at $\sim$413 $1/\omega_p$. b)The normalized potential $\overline{\Psi}$ vs space with the initial location of trapped (shown in green) and un-trapped (shown in red) electrons from N^{6-7+}. The trapped electrons are always injected closer to the center of the wakefield as compared to the un-trapped electrons.

determines the potential difference, and thus whether or not the electron can gain enough energy to move with the wake at v_ϕ and become trapped before slipping out of the first period of the wake.

From the simulation data, the normalized potential difference $\Delta\overline{\Psi}$ for the group of trapped electrons can also be found and compared to the analytic estimate for the required $\Delta\overline{\Psi}$ for trapping to occur given by equation 3.20. For 2-D simulations, when the laser is polarized within the plane of the simulation, the injected electrons experience the combined laser and wake forces in the same plane. This allows for a more accurate description of the trapping process as opposed to the situation when the laser is polarized out of the plane of the 2-D simulation and the laser and wake forces are decoupled and in different planes.

As discussed above, over the range of times that electrons are injected via ionization and then trapped by the wakefield, the potential of the wake is essentially quasistatic. Therefore, in order to find $\Delta\overline{\Psi}$ the relative location within the potential at which an electron is created, which gives $\overline{\Psi}_i$ and the location at which the electron trapped, which gives $\overline{\Psi}_f$ is needed. The initial injection location of each electron is given by the simulation track data. To find $\overline{\Psi}_f$, the location within the potential where the longitudinal velocity of the electron equals v_ϕ must be found. Unfortunately, when electrons are trapped within the envelope of the electric field of the laser, as they are in the simulation when the pulse width of the laser is 45 fs, it becomes difficult to determine the exact time / location at which an electron is trapped. This is because the perpendicular and longitudinal momentum of the electron is being modulated by the field of the laser, causing the electron to accelerate and decelerate around the phase velocity of the wake. Additionally the phase velocity of the wake is constantly evolving due to pump depletion and non-linear frequency shifting of the laser electric field. The limited

time resolution at which data pertaining to the wake velocity is recorded from the simulation, limits the accuracy for determining the instantaneous v_ϕ of the wake. This effect combined with the momentum modulation of the electron due to the electric field of the laser leads to an uncertainty in determining $\overline{\Psi}_f$.

To make a more accurate measurement of the $\Delta\overline{\Psi}$ that trapped electrons experience, a simulation was preformed with the laser field polarized in the plane of the simulation. For this simulation the same laser and plasma parameters were used as stated above, except that the laser pulse width was shortened from 45 fs to 11 fs. With the shorter pulse width, electrons were no longer trapped within the field of the laser. Figure 3.8 details the location at which electrons from N^{6-7+} are created (green circles) and trapped (black circles) within the laser field and wake potential. As shown in Fig. 3.9 a) for each trapped electron, the potential difference $\Delta\overline{\Psi}$ was found and plotted against the final perpendicular momentum of the electron, $p_{\perp f}$ at the instant that trapping occurred. The solid red line in Fig. 3.9 a) is the required potential difference for trapping plotted as a function of $p_{\perp f}$ that was analytically estimated by Eqn. 3.20 using a fixed $\gamma_\phi = 10.95$ corresponding to a plasma density of 1.4x10^{19} cm^{-3}. As shown in Fig. 3.9 a) there is some scatter between the simulated normalized potential difference $\Delta\overline{\Psi}_{sim}$ and the estimated normalized potential difference $\Delta\overline{\Psi}_{est}$ for trapping. If the evolution of the phase velocity of the wake is taken into account, the difference between $\Delta\overline{\Psi}_{sim}$ and $\Delta\overline{\Psi}_{est}$ is decreased as shown by Fig. 3.9 b). This figure shows that for the majority of the tracked electrons, the difference between the simulated and calculated $\Delta\overline{\Psi}$ is $\sim .05$, which for a $\Delta\overline{\Psi} \approx .9$ gives an agreement of $\sim 5\%$. Figure 3.9 b) indicates that the required $\Delta\overline{\Psi}$ found in 2-D simulations is in good agreement, with that which was analytically estimated given by Eqn. 3.20.

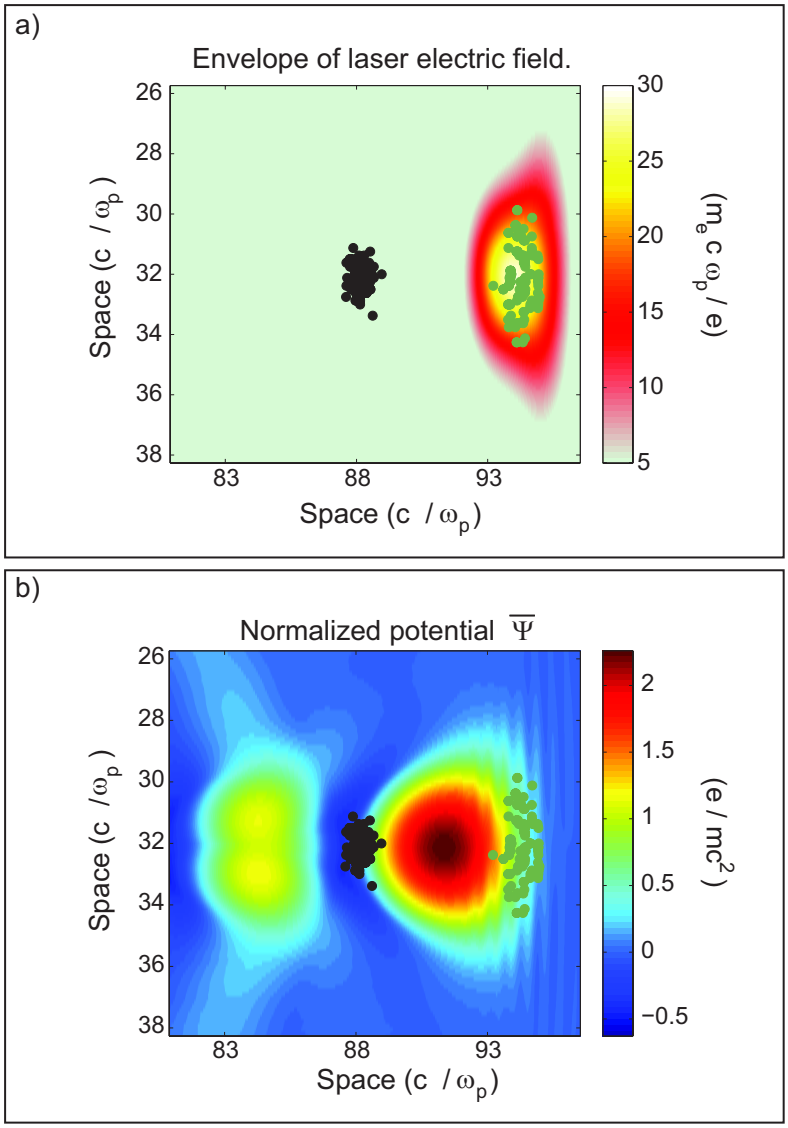

Figure 3.8: a)The envelope of the laser electric field, with a pulse width of 11 fs (FWHM intensity) plotted vs space. The location of the initial and final trapped position of injected electrons from the N^{6-7+} ionized states is shown by the green and black circles respectively. b)The normalized potential $\overline{\Psi}$ plotted vs space with the initial and final injection and trapping locations of electrons shown.

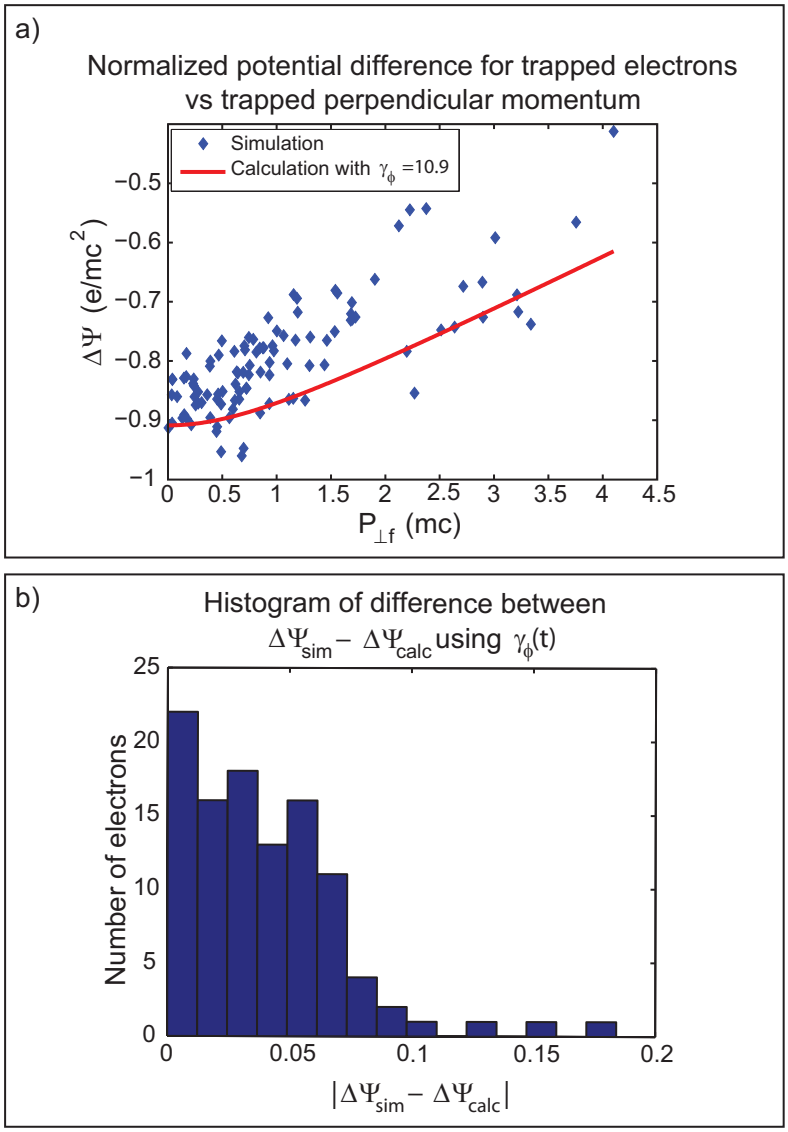

Figure 3.9: a)The simulated (blue diamonds) normalized potential difference that a group of electrons from N^{6-7+} experience between being created and being trapped plotted vs the final perpendicular momentum of the electron at the instant that it is trapped. The solid red line corresponds to the analytic estimate of the the $\Delta\overline{\Psi}$ required for trapping using a fixed $\gamma_\phi = 10.95$. b) Electron number vs the difference between the simulated $\Delta\overline{\Psi}$, and analytically calculated $\Delta\overline{\Psi}$ taking into account the time evolving wake velocity and γ_ϕ.

In conclusion, in this section a analytical model for the potential difference $\Delta\overline{\Psi}$ that is required for an electron to be trapped within the wakefield was detailed. Using an approximation for the wake size and longitudinal accelerating field amplitude in the matched blowout regime, it was shown that the potential difference available for electrons exceeds the estimated required $\Delta\overline{\Psi}$ over a large range of injection phases. Additionally, it was shown that the maximum energy gain for an electron is a function of wake amplitude and injection phase. Finally, using 2-D OSIRIS particle in cell code simulations, which included the ADK ionization model, it was found that the analytical estimate for the required $\Delta\overline{\Psi}$ for trapped electrons was in good agreement with the $\Delta\overline{\Psi}$ for trapped electrons observed in simulations. Work is being done to integrate a potential Ψ diagnostic into OSIRIS, to increase the time resolution and accuracy at which $\Delta\overline{\Psi}$ can be measured.

CHAPTER 4

Experimental Setup and Methods

Experiments to investigate tunnel ionization injection and trapping were conducted at UCLA using a CPA Ti:Sapphire laser system. Laser pulses with energies ranging from 200-500 mJ and average pulse widths of $\sim$ 45 fs were focused by an off-axis parabolic mirror (OAP) to a spot size of $\sim$ 5 μm. Here the pulse width is defined as the full width at half maximum (FWHM) of the intensity of the pulse and the spot size is taken to be the distance to $1/e$ of the electric field. Taking into account that $\sim$70% of the energy could be focused into the spot size, the power ranged from 4-10 TW and the peak a_o of the laser varied from $\sim$1.5 to 2.5 in these experiments. To create a plasma and a LWFA, the waist of the laser pulse was focused 50-150 μm inside the front edge of a column of gas created by a conical gas jet. The leading edge of the laser pulse was intense enough to ionize the gas to create the plasma. The ponderomotive force of the laser then displaced free electrons driving a wake and creating the accelerating structure. Electrons accelerated by this wake were sent through a dipole magnet onto a Lanex phosphor film. A $\sim$ 100 μm thick piece of aluminum foil was placed in front of the Lanex film to block transmitted laser light. Electrons with energies above $\sim$ 1 MeV pass through the thin aluminum light shield onto the Lanex film. Collisions between the accelerated electrons and the phosphorescent substrate of the Lanex film resulted in visible light being created. The light from the phosphor screen was imaged by a 35 or 50 mm camera lens onto either a 12 bit or

16 bit CCD camera. The energy of the electrons was measured by observing the induced deflection of the electrons by a dipole magnet onto a Lanex screen. The experimental setup used to measure the electron energy spectrum is shown in Fig. 4.1. As shown in Fig. 4.1, a probe beam was created from the small amount of light ($< 1\%$) transmitted through the last turning mirror before the OAP. The probe beam was sent into a Michelson interferometer which was used to measure the plasma density profile on every shot. The interferometer was setup such that the plasma was probed $\sim$ 75 ps after the main pump beam had passed. The pulse width of the probe beam was estimated to be less than 100 fs long.

A conical gas jet with a .5 mm throat and either a 2 or 3 mm opening was used in these experiments [70, 71]. To observe the effects of tunneling ionization injection, a wake was driven in plasmas created from a mixture of helium and nitrogen as well as in a mixture of helium and methane gases. Results were then compared to LWFA driven in plasmas created from pure helium and pure nitrogen gases. For both mixtures the two ratios that were investigated were 90% helium and 10% nitrogen/methane and a 95% helium and 5% nitrogen/methane. Each gas mixture was ordered pre-mixed from the Air Liquid gas company.

For gas mixtures that were used, it was found that the acceleration of electrons was sensitive to the level of laser contrast. The contrast of the laser pulse is defined by the ratio between the peak intensity of the laser pulse to the the intensity of the laser pulse at some time before the peak. Ideally, before the laser pulse arrives no laser light would exist. Unfortunately, several smaller 'pre-pulses' exist and arrive at the plasma before the main pulse does. Pre-pulses come from two sources within the laser system and arrive on two different time scales before the main pulse. Amplified spontaneous emission (ASE), which is created and amplified in both the laser oscillator and regenerative amplifier, creates a

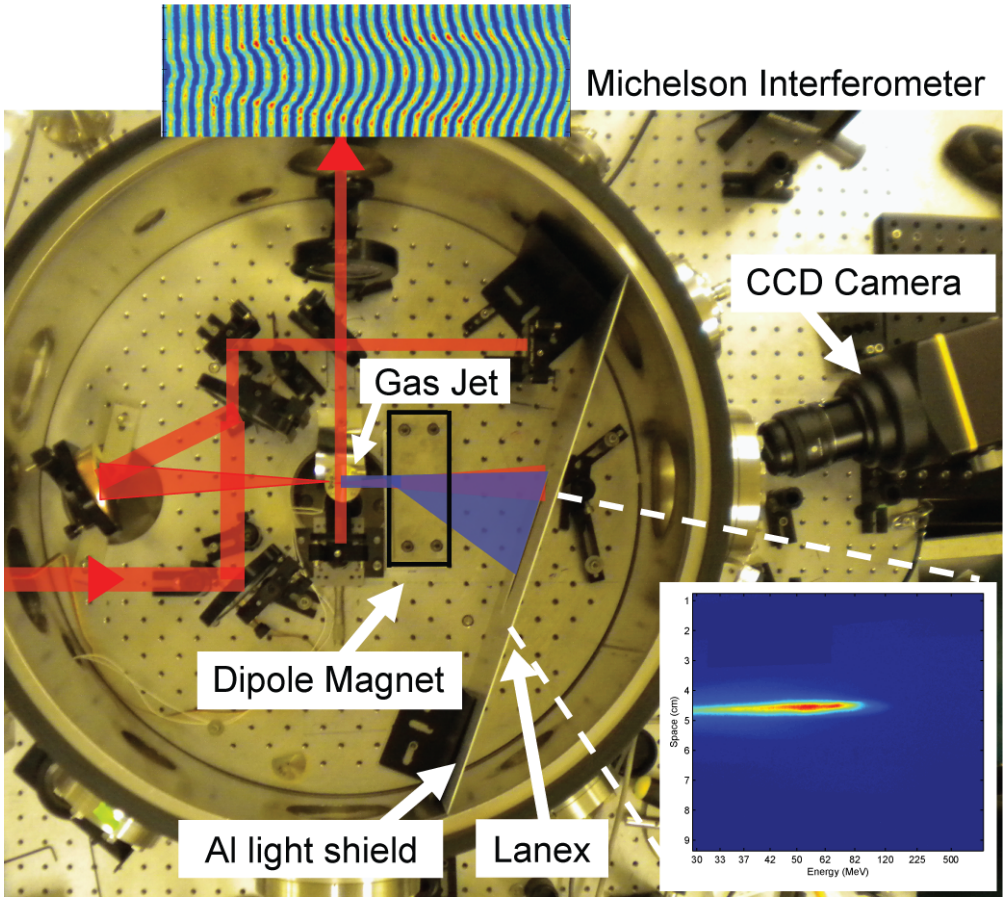

Figure 4.1: Diagram of experimental setup. The amplified laser pulse shown in red, is focused by an off axis parabolic mirror on to the edge of a supersonic gas jet nozzle creating a LWFA. The transmitted laser light is dumped onto a aluminum light shield, while electrons which are created, shown in blue, are dispersed by the dipole magnet. These electrons pass through the Al shield onto a Lanex screen which phosphoresces. An example of the deflected electron signal recorded by the intensified CCD camera is shown in the bottom right. A small amount of transmitted laser light from the last laser turning mirror was used as a probe beam and sent into a Michelson interferometer. The interferogram that is created records the plasma density profile. An example of a typical interferogram is shown at the top of the figure.

pedestal on top of which the main pulse sits. The ASE pedestal exists over several nanoseconds and the front edge of the pedestal is considered to be a pre-pulse, as it arrives a few nanoseconds before the main pulse. Partial reflections and transmissions within the laser system can create lower intensity replicas of the main pulse. These replicas are separated in time from the main pulse, and are also amplified by the laser system creating pre-pules which usually arrive picoseconds before the main pulse.

On a nanosecond time scale, laser pre-pulse are thought to negatively effect LWFA experiments as they can be intense enough to ionize a small region of plasma before the main pump pulse arrives. Over a nanosecond, the plasma has enough time to diffuse away. Therefore, by the time the main pulse arrives, the plasma density will be lower than desirable and spatially inhomogeneous. This will change the way in which the laser pulse focuses within the plasma and effects the coupling of energy into the accelerating wake structure. On a picosecond time scale, plasma created from pre-pulses do not have as much time to diffuse. It is not known how detrimental picosecond pre-pulses are to the success of the LWFA experiments.

To measure the contrast of the laser on a nanosecond time scale, a fast photo diode with $\sim$ 1 ns time resolution was used. The signal from the diode was displayed on a Textronix TDS-3032B oscilloscope. The contrast that could be measured was approximately 10^4. In these experiments if the diode detected even a small level of nanosecond pre-pulse, the likelihood of observing accelerated electrons decreased dramatically. An example of a laser pulse with a measurable pre-pulse and without a measurable pre-pulse is shown in Figure 4.2. On a nanosecond time scale, ASE pre-pulse can be reduced by changing the timing of the two pockel cells within the regenerative amplifier. These pockel cells control

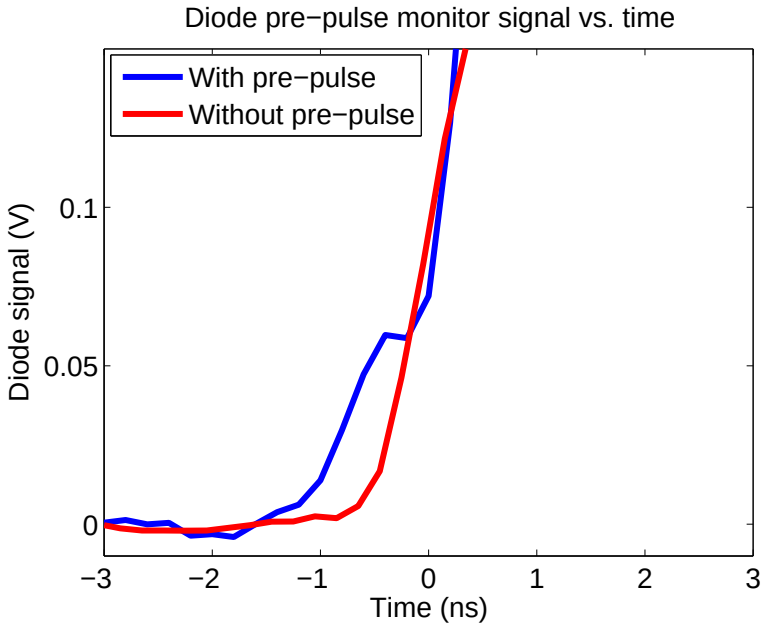

Figure 4.2: Pre-pulse on a nanosecond time scale

the time at which the laser pulse in switched into and out of the regenerative amplifier. Switching the laser pulse into the regenerative amplifier as late as possible and switching the laser pulse out as early as possible, reduces the time over which ASE is amplified and thus can reduce the pre-pulse level. A third pockel cell, known as the 'slicer' was also used after the regenerative amplifier. The slicer was used to chop as much of the remaining ASE as possible without cutting into the main pulse.

Experiments conducted in pure helium were the most insensitive to the level of nanosecond pre-pulse. This is because the first electron of helium has a relatively large ionization potential (24.5 eV) and therefore requires a relatively large intensity ($\sim 10^{15}$ W / cm^{-3}) to be ionized. The level of permissable pre-pulse became smaller and smaller as gas mixtures containing nitrogen and then methane began to be used. The first electron of nitrogen is ionized at an ionization poten-

tial of 14.5 eV and the four electrons from hydrogen contained in each methane molecule are ionized at 13.6 eV. These lower ionization potentials reduced the required laser intensity for ionization to $\sim 10^{14}$ W/cm^{-3}. It was observed that as the laser power was increased beyond ~ 5 TW, the level of pre-pulse became large enough to negatively effect experiments conducted in the nitrogen and methane gas mixtures. To further enhance the contrast beyond what was obtainable using the pockel cells, a thin (2 mm) red glass filter (RG850), with an anti-reflection coating at 800 nm was inserted into the output of the regenerative amplifier. The red glass filter passes light with wavelengths longer than 850 nm and attenuates wavelengths below 850 nm. The central wavelength of the laser was ~ 815 nm, and therefore is attenuated. However, at high intensities the red glass filter acts as a saturable absorber. Therefore, the lower intensity nanosecond pre-pulse was attenuated, while the more intense main pulse saturated the red glass and was transmitted with only a slight attenuation. In this manner, the contrast was thought to be improved 5-10 times, and allowed successful experiments to be preformed in nitrogen and methane gas mixtures with powers greater than 5 TW.

Additionally the success of the experiment was very dependent on the the relative alignment of the gas jet height, longitudinal z and transverse y position, with respect to the waist of the laser pulse. A camera equipped with a 35 mm camera lens was mounted on the top of the target chamber. This camera, known as the top view camera, looked down onto the gas jet and was used to align the nozzle in the transverse and longitudinal directions. The height of the nozzle was set by observing the density profile obtained from the Michelson interferometer diagnostic. The following alignment procedure was used to in these experiments to obtain accelerated electrons. First, under vacuum, the gate valve was closed and the target chamber was filled with ~ 5 torr of nitrogen gas. After checking the

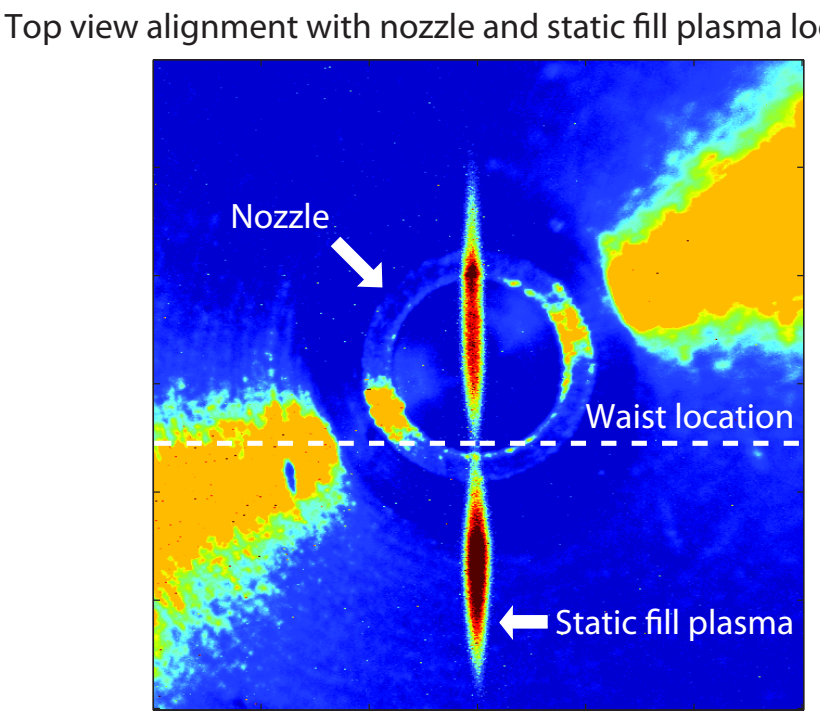

Figure 4.3: Top view of nozzle and static fill plasma location. The nozzle is aligned such that the static fill plasma is centered transversely and such that the laser waist is located ~ 100 μm inside the front edge of the nozzle.

transverse profile of the laser beam for hot spots before the compressor, the laser pulse was amplified to 1-2 TW and was allowed to enter into the target chamber. The laser pulse was intense enough to ionize the nitrogen gas and form a dumbbell shaped 'static fill' plasma as shown in Fig. 4.3. Using the top view camera with a blue glass filter to block the red laser light, the laser waist location was marked using static fill plasma profile. The nozzle was then positioned such that the waist of the static fill plasma was located ~ 100 μm within the front edge of the nozzle and transversely centered as shown in Fig. 4.3. From preforming many experiments with the same OAP and F-number beam, it has been observed that for consistent self-guiding and creation of electron beams the laser waist should be located ~ 100 μm within the front edge of the gas jet. Often times during the experiment, the longitudinal z position is scanned $\pm$ 100 μm in 50 μm steps around the initial location to try and optimize the coupling of the laser pulse into the plasma wake to obtain more consistent results. After the static fill alignment was preformed, the gate valve was opened and time was allowed for the target chamber to be pumped back down to vacuum. The gas line from the gas bottle to nozzle was then flushed to ensure that it was containment free. An approximate plasma density was then chosen and the corresponding nozzle backing pressure was set.

Using the Michelson interferometer, the height between the plasma and top of the nozzle was first set to be ~ 1 mm. The gas jet was then triggered to fire and using 1-2 TW of power the plasma density profile was observed. Scanning the height of the nozzle $\pm$ .25 mm, the final height of the nozzle was set to be at the location which gave the flattest density profile was obtained. An example of how the plasma density profile varied with height is shown in Fig. 4.4. It should be noted that the height at which the best density profile is obtained will change with backing pressure and with the gas mixture used. The variation of

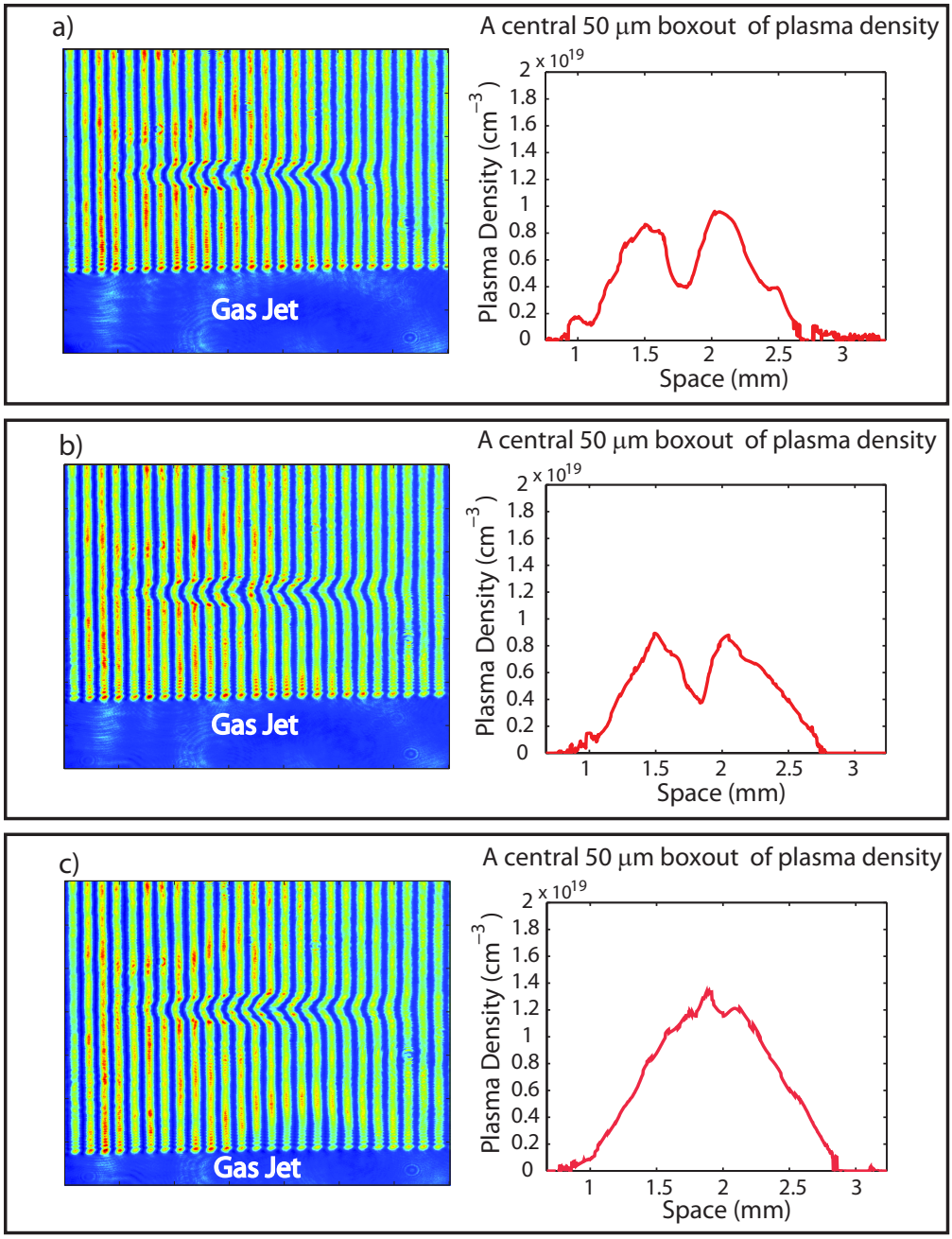

Figure 4.4: A interferogram and corresponding plasma density at 3 different gas jet heights (a-c). For each height the backing pressure on the gas jet was fixed at 100 PSI and the 90:10 He:N_2 gas mixture was used. As the gas jet is lowered the plasma density profile changes and becomes smoother.

the plasma density profile with height is thought to be due to shocks which form as the gas expands and leaves the nozzle as it enters the vacuum chamber.

The day to day alignment of the laser, including the final pointing through the target chamber and onto OAP is another important factor to the reproducibility and success of the experiment. An image of the focal spot, which was directly recorded using only a 20x microscope objective to image the laser focus is shown in Fig. 4.5. The resolution of this objective was ~ 4 μm. This image of the laser spot was recorded close too, but probably not exactly at best focus. Additionally, as the image plane was scanned around the laser focus, an astigmatism in the laser spot size was observed. This abberation might have contributed to the slightly larger than nominal spot size measured and to the amount of light that is outside the laser spot size. The FWHM of the spot intensity was 6.7 μm in the x-direction by 6.8 μm in the y-direction. These widths correspond to a spot size of $\sim$5.8 μm for a Gaussian. The matched spot size for self-guiding at a plasma density of 1.4 $\times 10^{19}$ cm^{-3} and over the range of laser intensities used in these experiments was 4-4.5 μm. Additionally over the range of laser powers used the ratio of P/P_c at this density was $\sim$1.5-3. Therefore for a nominal spot size of 6 μm, the ratio of $P/P_c > 1$ indicates that a small amount of self-focusing is expected as the laser pulse evolves to the matched spot size in these experiments.

To monitor the focused spot size of the laser during the experiment, a forward imaging diagnostic, which imaged relayed the laser focus after the OAP to a CCD camera with a magnification of $\sim$ 12x, and a resolution of $\sim$6 μm was employed. This diagnostic was used before most experimental runs to ensure that the laser spot was of good quality, and not aberrated. The forward spot diagnostic could also be set to image the exit of the plasma. In this manner the output laser mode from the plasma could be monitored, and the relative amount of laser self-guiding

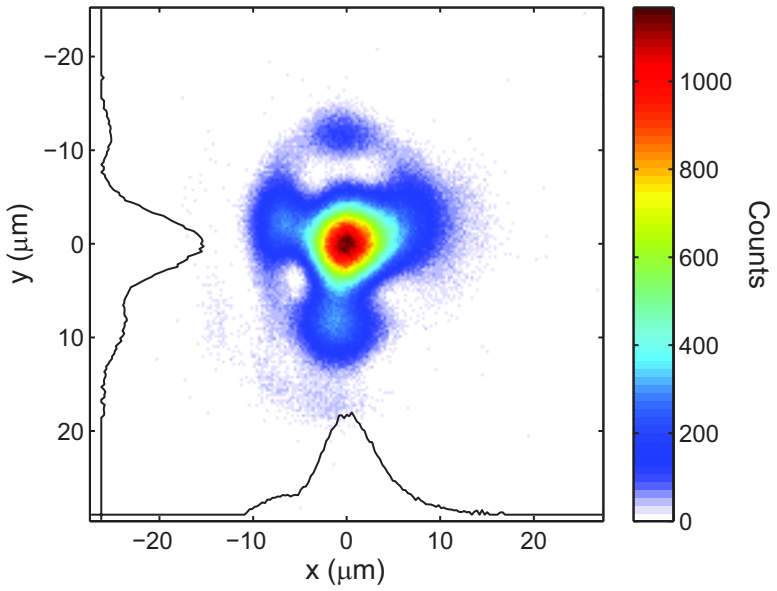

Figure 4.5: The spatial profile of the laser pulse near best focus recorded with a 20x microscope objective. The FWHM is equal to 6.7 μm and 6.8 μm in the x and y direction respectively.

could be observed. Additionally the transmitted laser light from the experiment could be image relayed onto an imaging spectrometer. The imaging spectrometer was also set to image the exit of the plasma and used a grating with 150 grooves / mm that was blazed for 500 nm. The slit of the imaging spectrograph was often opened to 300-500 μm to ensure that the transmitted laser light passed into the spectrograph. With such a large slit size the spectral resolution was determined by the spot size of the image relayed laser light. When the laser pulse was self-guided through the plasma, the spot size at the slit of the spectrograph was $\sim$ 10-15 μm giving a spectral resolution of $\sim$ 2 nm. The transmitted laser light was imaged by the spectrograph in the transverse plane with spatial resolution of $\sim$13 μm. The imaging spectrometer allowed the guided portion of the transmitted laser light to be distinguished from the un-guided transmitted light. In this manner the laser light which had been spectrally modulated from interacting with the wakefield and from ionization of neutral gas could be identified. When the experiment was set up to measure the energy of accelerated electrons as shown in Fig. 4.1, access to the forward transmitted diagnostics was lost.

The input laser energy and pulse width were also recorded on every laser shot. A 1% light leak through a turning mirror from the first and second multipass amplifiers was sent to two different diodes. The voltage measured by each diode was calibrated to a Coherent J-50-MB-LE energy meter. The transmission through the compressor gratings, focusing OAP, and an estimation of the amount of laser light in the $1/e$ focused profile was taken into account to determine the amount of laser energy participating in the interaction.

The pulse width was measured using a Positive light utlrafast single shot auto-correlator. The auto-correlator could measure pulses as short as $\sim$40 fs with a resolution of $\pm$4 fs. During the experiment, a leak of the compressed

laser pulse was sent to the auto-correlator to monitor the pulse width on every shot. The pulse width of the laser light leaked to the auto-correlator will not be the same as the pulse width of the main pump that is sent to the experiment. This is because the light that is leaked passes through over a centimeter of glass. The group velocity dispersion (GVD) of the glass causes the leaked light to be broadened in time. For short laser pulses with 20-30 nm of bandwidth, even this small amount of glass can broaden the pulse width of the laser by 5-10%. To send the shortest laser pulse to the experiment the following technique was used. First the distance between the compressor gratings was set such that the auto-correlator measured the minimum pulse width. At this setting, the gratings are actually set to send a slightly longer, frequency chirped (blue to red) laser pulse to the experiment. However, at the auto-correlator the shortest pulse width of the laser is measured because the glass in the path to the auto-correlator causes the chirped pulse to be compressed in time. The amount of GVD from the glass in the auto-correlator path width can be calculated. Additionally, the amount that the compressor gratings need to be moved to compensate for the GVD of the glass can also be calculated. To send the shortest laser pulse to the experiment, the calculations indicated that the gratings needed to be moved together by 150 μm from where the shortest pulse is measured at the auto-correlator. To confirm that this correction actually sent the shortest pulse to the experiment, a scan of compressor spacings over $\pm$ 200μm was preformed and the amount of ionization induced blue shifted light was recorded. The energy of the laser was set such that only a very small amount of ionization induced blue shifted light was initially observed. As the compressor spacing was scanned, the pulse width of the laser changed and near threshold the largest amount of ionization induced blue shifted light should correspond to the laser pulse with the shortest pulse width. This location was found to corresponded to the same position that was

predicted using the GVD calculations. The correction of 150 μm in the grating spacing changed the pulse width of the laser by about 6 fs.

As a result of measuring the laser energy and pulse width, the amount of laser power was therefore known and using the vacuum laser spot size, one could determine the a_o of the laser on each shot. Additionally, on each shot the plasma density was measured using interferometry, and either the transmitted laser or electron properties were observed. In this manner a careful and detailed study of the laser plasma interaction which created the LWFA and accelerated electron beams was made.

As stated above, a Michelson interferometer was used to create an interferogram to measure the plasma density that was created on each shot. A brief description of a Michelson interferometer, the method of phase retrieval and Abel inversion used will now be given. In a Michelson interferometer, an input pulse is split by a beam splitter into two identical pulses. The two pulses are sent into two separate, but nearly identical delay arms. After passing through the delay arms, the two pulses are retro-reflected and then recombined by a beam splitter. The two recombined laser pulses interfere with one another. The interferogram created records the difference in phase between the two arms (or two laser pulses) of the Michelson. One arm of the Michelson is known as the probe arm, as it passes through the plasma. For the Michelson setup in this experiment, the probe arm and main drive pulse where timed such that the probe arm only made one pass through the plasma. The other arm of the Michelson does not contain any additional object to modify the phase of the pulse and is known as the reference arm. When there is no plasma present, the interferogram records the difference in phase resulting from the path length difference between the two arms of the Michelson.

When a plasma is created, the phase of the probe pulse arm is modified by index of refraction of the plasma. To recover the phase difference between the probe and reference pulses, a 2-D Fourier transform is taken of the interferogram. In the k-space domain, there will be three features. At $k = 0$, there will be a 'DC' component which contains no phase information, and is just proportional to the square of the amplitudes of the two Michelson pulses. Centered at a $k = \pm k_{int}$, there will be an 'AC' component which will contain the phase difference between the two arms of the Michelson. Here k_{int} is the wave number or spatial frequency of the interference pattern. Filtering out one of the AC k components, and then taking the inverse Fourier transform one recovers,

$$\mathrm{AC}(x,z) = E_{\mathrm{p}}(x,z)E_{\mathrm{ref}}(x,z)exp\Big[i(\Delta\phi_{\mathrm{delay}}(x,z) + \Delta\phi_{\mathrm{plasma}}(x,z))\Big] \quad (4.1)$$

where $E_{\mathrm{p}}(x,z)$ and $E_{\mathrm{ref}}(x,z)$ are the amplitudes of the probe and reference arms respectively, $\Delta\phi_{\mathrm{delay}}$ is the phase difference due to the spatial delay between the two Michelson arms, and $\Delta\phi_{\mathrm{plasma}}$ is the phase difference between the two Michelson arms due to the plasma. Here the spatial coordinate system is used, where z is the direction of the laser pump pulse, x is the vertical up / down direction, and y is horizontal left / right direction. The phase term containing $\Delta\phi_{\mathrm{delay}} - \Delta\phi_{\mathrm{plasma}}$ can be found by taking the arctangent of the real values of AC(x,z) divided by imaginary values of AC(x,z). The values of the arctangent range from $-\pi$ to π and because of this any recovered phase will need to be *unwrapped* as detailed by [72] (fortunately Matlab has a built in unwrapping function which can be used). To isolate $\Delta\phi_{\mathrm{plasma}}$, a reference measurement can be made when there is no plasma and the same Fourier analysis can be preformed to recover just the $\Delta\phi_{\mathrm{delay}}$ phase term. Subtracting the reference delay phase from the measurement made with the plasma leaves only, $\Delta\phi_{\mathrm{plasma}}$.

For a 2-D interference pattern, such as the ones shown in Fig. 4.4, the

$\Delta\phi_{\text{plasma}}(x,z)$ that is measured is the total integrated phase of the plasma vs space. The amount of integrated phase that the probe beam accrues as it transverses across the plasma in the y direction, is proportional to the index of refraction and the thickness of the plasma. The integrated phase difference between the reference and probe arm is then given by,

$$\begin{aligned}
\Delta\phi_{\text{plasma}}(x,z) &= \int \Delta k dy \\
\Delta\phi_{\text{plasma}}(x,z) &= \int \Big(k_o - k_p(x,y,z)\Big) dy \\
\Delta\phi_{\text{plasma}}(x,z) &= \int \frac{2\pi}{\lambda}\Big(1 - \text{in}_p(x,y,z)\Big) dy
\end{aligned} \tag{4.2}$$

where here k_o is the vacuum wave number of the probe light, and k_p and in_p are the wave number of the probe beam within the plasma and the index of refraction of the plasma, respectively. Using the plasma dispersion relationship, the index of refraction of the plasma, in_p, can be related to the plasma density and is given by,

$$\begin{aligned}
\text{in}_p &= \sqrt{1 - \frac{n_e e^2}{\epsilon_o m_e \omega^2}} \\
\text{in}_p &\approx 1 - \frac{1}{2}\frac{n_e e^2}{\epsilon_o m_e \omega^2}
\end{aligned} \tag{4.3}$$

This relationship can now be substituted into Eqn. 4.2, and an equation for the integrated plasma density can be solved for in the following manner,

$$\begin{aligned}
\Delta\phi_{\text{plasma}}(x,z) &= \int \frac{2\pi}{\lambda}\Big(1 - 1 + \frac{1}{2}\frac{n_e(x,y,z)e^2}{\epsilon_o m_e \omega^2})\Big) dy \\
\Delta\phi_{\text{plasma}}(x,z) &= \frac{\lambda e^2}{4\pi\epsilon_o m_e c^2}\int n_e(x,y,z) dy \\
\frac{4\pi\epsilon_o m_e c^2}{\lambda e^2}\ \Delta\phi_{\text{plasma}}(x,z) &= \int n_e(x,y,z) dy
\end{aligned} \tag{4.4}$$

Assuming the plasma is cylindrically symmetric in the x-y plane, an Abel inversion of the integrated phase difference can be made to recover the plasma

density profile, $n_e(x, y, z)$. There are a few methods which can be used to preform an Abel inversion. An early paper on the subject, with a good conceptual model of the process and a detailed example of such an inversion is [73]. In this reference, a 1-D example is given with the left hand side of Eqn. 4.4 being denoted as the $N(x)$, the spectral radiance in the y direction while $n_e(x, y, z)$ on the right hand side of Eqn. 4.4 is written as $\epsilon(r)$, the emission coefficient of the plasma.

To measure the plasma density from the recovered phase in this work, the Abel inversion was preformed using a method developed by Kalal and Nugent [74]. This method follows Bockasten's physical picture of Abel inversion (with slight coordinate and variable name changes), but cleverly uses a Fourier series to approximate the integrated phase difference of the plasma. Once the left hand side of Eqn. 4.4 has been expressed analytically, a derivative can be taken and the plasma density $n_e(x, y, z)$ can be solved for directly. It should be noted that when approximating $\Delta\phi_{\text{plasma}}(x, z)$ a sufficient number of coefficients for the Fourier series should be used to obtain an accurate Abel inversion.

All methods of Abel inversion assume that the plasma, or phase object is cylindrically symmetric. In experiments, the measured phase shift is almost never symmetric in space. Therefore in order to preform the Abel inversion, the profile or lineout of the phase is split into two pieces. In this work the phase was split into two pieces at the centroid of the phase lineout. A copy of each piece is made, then mirrored and recombined with the original piece to make two symmetric phase objects. Each symmetric object is then separately Abel inverted, then each object is split in half and reconnected with the other un-symmetric half. In this manner one can Abel invert un-symmetric phase objects. At the center of the phase object, the Abel inversion tends to be a bit noisy, with un-physical increases and decreases in plasma density being recovered. Additionally the Abel

inverted density is often slightly discontinuous where the two phase objects were split and rejoined. This can limit the accuracy of the on axis density which is recovered.

Another factor that limited the accuracy of the Abel inversion, is the amount of phase noise between the measured reference and plasma interferograms. This can be quantified by subtracting the phase recovered from two different reference interferograms (i.e. no plasma). Ideally there would be no difference in phase between two reference shots, but unfortunately in the Michelson setup used for this experiment the level of phase noise varied in a random manner by $\pm.2$ radians across the interferogram, as shown in Fig. 4.6 a). The recovered phase contribution from a plasma is shown in Fig. 4.6 b). Here the drive laser pulse is traveling from the right to the left, and the approximate laser focus and axis are denoted by the red arrow and white dashed line, respectively. To examine the effect of phase noise on the recovered density, .2 radians of phase was added and subtracted from the recovered phase shown in Fig. 4.6 b). It should be noted that phase was only added and subtracted to values of the initially recovered phase that were greater than .2 radians (i.e. noise was not added to noise). As shown in Fig. 4.6 c), adding or subtracting phase to the recovered density does not drastically effect the peak recovered density. This is because the amount of noise, .2 rad, is still relatively small to the maximum phase shift of 4 rad. Additionally, as the laser pulse leaves the plasma, the laser spot size is larger due to diffraction and therefore, even though the plasma density is dropping, the volume of plasma is large enough that a fair amount of phase shift is accrued by the probe pulse. Because of this, the small amount of phase noise does not have a large effect on the plasma density profile at the back of the plasma. However, at the front edge of the plasma where the laser pulse is initially focused, the volume of plasma is very small and the plasma density is relatively low. This leads to a

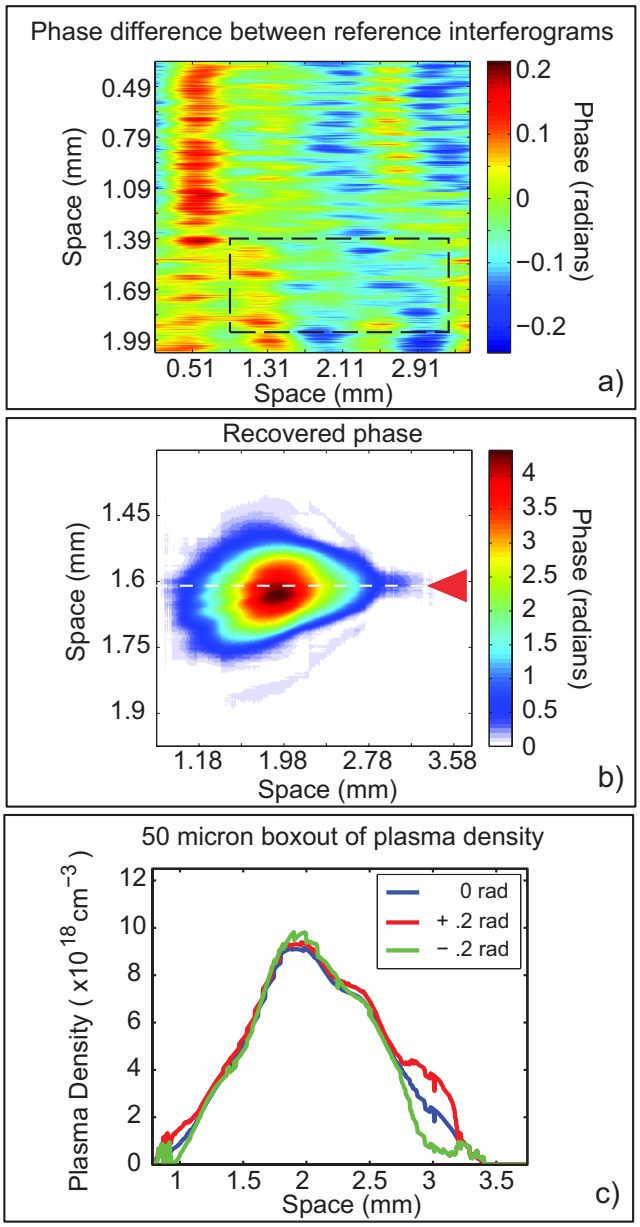

Figure 4.6: a)Phase difference between two reference interferograms vs space. The dashed boxed area corresponds to the area of recovered plasma phase vs space as shown in frame b). In frame b) the red arrow and white dashed line correspond to the approximate laser focus and axis. c) The plasma density profile vs space for the recovered phase with 0 and $\pm$ .2 radians of phase noise added.

very small phase shift being recorded in this region as shown in Fig. 4.6 b) at around 3 mm in space. The addition of phase noise to this region, where now the amount of signal is approximately equal to the amount of noise, results in a large change in the recovered profile and density of the plasma. The rate at which the plasma density rises at the leading edge is of great interest for many experiments, as large density ramps can decrease the amount of coupled laser light into the plasma interaction. To make an accurate density measurement of this region, one should try to increase the amount of phase signal to phase noise. To do this the laser beam could be defocused in order to create a larger volume of plasma to create a larger phase signal. Another option to increase the amount of measured phase would be to increase the wavelength of the probe laser pulse. As Eqn. 4.1 indicates, increasing the probe wavelength increases the amount of measured phase shift. Additionally, if the gas jet and thus plasma profile is assumed be symmetric in the z-direction of laser propagation, then the rising edge plasma profile could be assumed to be equal to the more accurately measured falling edge profile.

An illustration of the dipole magnet that was built to deflect the accelerated electrons is shown in Fig. 4.7 a). The dipole magnet was designed using concepts from G.A. Novikov et. al. [75]. The frame of the dipole magnet was constructed out of low carbon steel (shown in grey), and had a small gap within the middle of the frame through which the electron beam passed. The length of the dipole magnet, measured from face to face, was 50.8 mm, with a gap of approximately 38.1 mm width by 12.7 mm tall. Several small neodymium magnets (shown in yellow), with large magnetic fields, were arranged within the larger casing. The low carbon steel casing of the dipole magnet served to contain and direct the magnetic field lines creating an almost uniform magnetic field across the open gap within the middle of the magnet. The field down the center of the magnet

gap spacing is shown in Fig. 4.7 b), and was measured using a calibrated FW model 5100 Hall effect Gauss meter. Profiles of the magnetic field to the right and left of the center were also measured and are almost identical to the profile shown in Fig. 4.7 b).

The purple rectangularly shaded region in Fig. 4.7 b), is the approximate equivalent magnetic field profile and is used in order to simplify the electron deflection calculation. The length of the equivalent magnetic field can be estimated using two methods, which give similar results. The first method used, is to integrate the entire measured magnetic field and set this area equal to the area of the equivalent field. The width of the equivalent field can be found as the 'height' or value of the equivalent field is assumed to be the peak measured value. Using this method the width of the equivalent field was found to be 65 mm. A second, empirically based method as described in [76] indicates, that for the dipole magnet structure being used here, that the length equivalent rectangular field from each face should be .62 x the gap height of the dipole magnet. At this location, the second method also predicts that the magnetic field should be 40% of the peak value. At a distance of 7.87 mm (.62x12.7 mm) from the face of the magnet, the measured field strength is 3727 Gauss and $\sim$ 40 % of the peak value as predicted. Again the magnitude of the equivalent field is set equal to the peak value of the measured field. The length of the equivalent field as determined by this second method is 66.5 mm and is equal to the length of the magnet 50.8 mm, plus 2x7.87 mm, the additional length from each face.

Accelerated electrons are bent or deflected in a circular motion within the equivalent magnetic field. To calculate the deflection again two methods were used. The first method calculated the radius of curvature of an electron using an

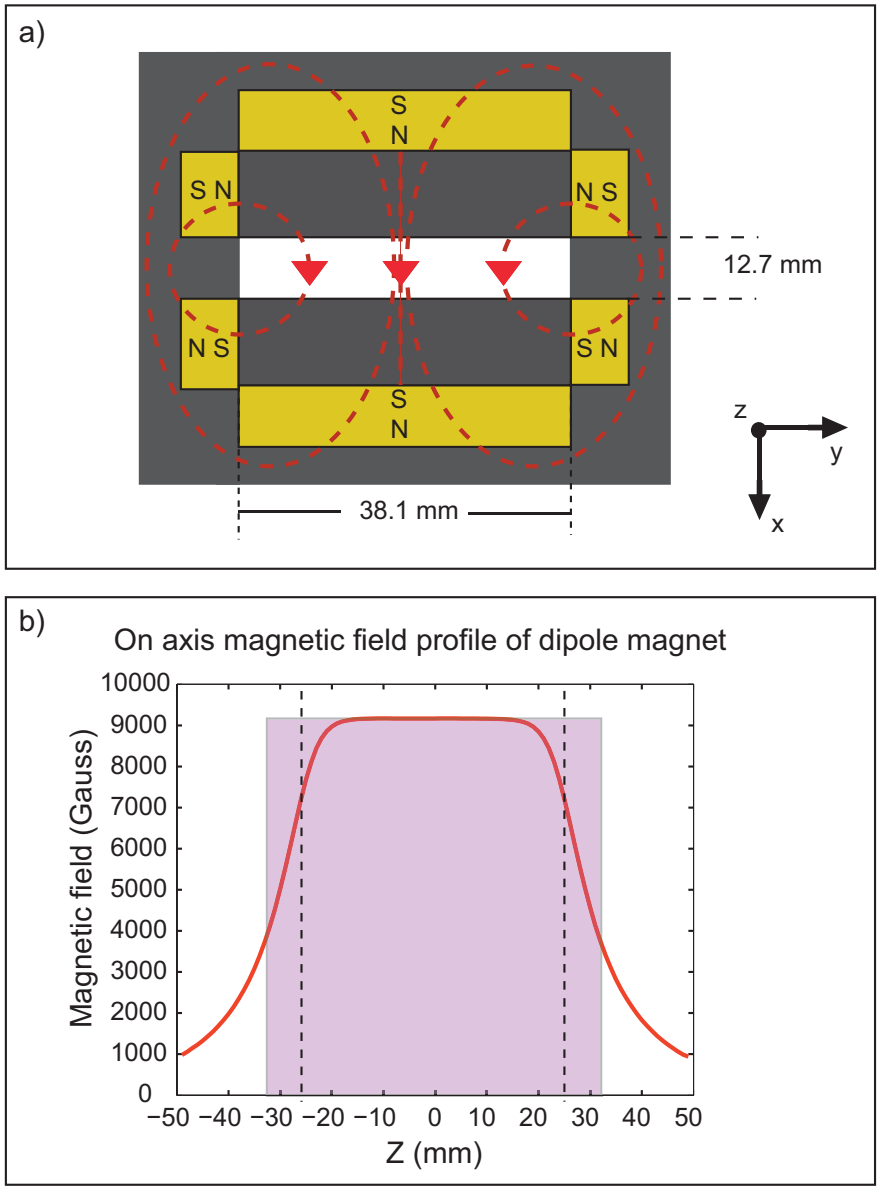

Figure 4.7: a)Illustration of the permanent dipole magnet that was used in the experiments. b) The measured on axis magnetic field of the dipole magnet vs longitudinal space. The dashed lines correspond to the 50.8 mm length of larger permanent dipole magnet, measured from face to face. The shaded purple region, with a width of ∼65 mm and a magnetic field value of 9170 Gauss, represents the equivalent magnet field which was used to calculate the electron beam deflection.

engineering formula given by,

$$R = \frac{3.4 \times 10^3 \times \text{Energy (MeV)}}{\text{B-field(Gauss)}}(\text{cm}) \tag{4.5}$$

where R radius of curvature of the electron is in units of cm and only depends on the energy of the electron being deflected and the magnitude of the magnetic field.

The electron trajectory through a magnetic field can also be calculated from the relativistic equations of motion. Since only the direction of the electron is being changed and no energy is being gained or lost through the magnetic field, γ is a constant and the relativistic equations of motion can be solved for in a straight forward manner. The deflection trajectory, and thus the inferred energy of electrons, depends on the energy of the electron, the magnitude of the magnetic field *and* the angle at which it enters the magnet. Using the equations of motion, the effect of an electron beam entering the magnetic field at an initial angle, can be included to give a more accurate description of the deflection trajectory of an electron. When the entrance angle into the magnetic field is set to be 0°, Eqn. 4.5 gives very good agreement with the trajectories calculated using the equations of motion.

Figure 4.8 a) shows the deflection imparted by the equivalent magnetic field on an electron beam over a range of electron energies. In this figure, a beam of electrons with a range of energies from 20-200 MeV is initially traveling to the right in the z direction at a height of 1 cm. At z = 0, the electron beam enters into the equivalent magnetic field of the dipole magnets. Electrons will be bent by this field as indicated by Eqn. 4.5, with lower energy electrons having a smaller radius of curvature, and thus being bent more, than electrons at higher energies. At a distance of ∼16 cm a LANEX screen is placed at an angle of ∼ 20° with respect to normal. The energetic electrons pass through the LANEX,

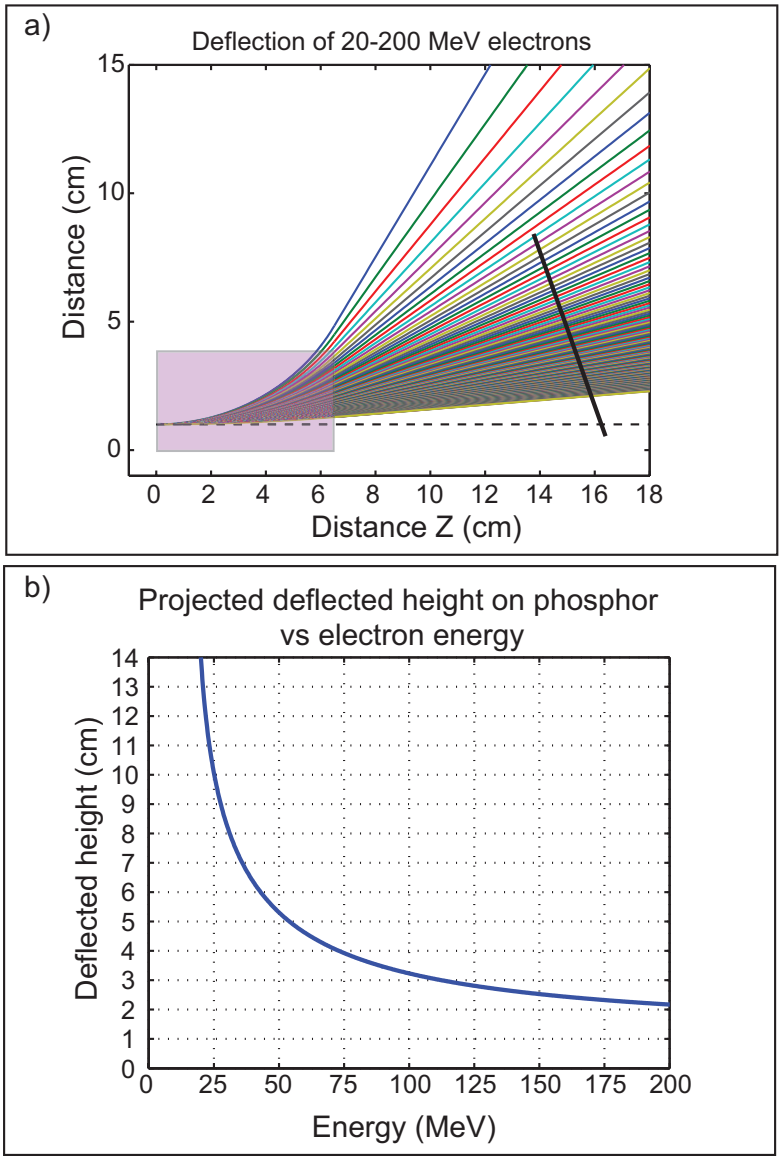

Figure 4.8: a)The deflected trajectories of electrons with energies ranging from 20-200 MeV, where each trajectory line is a 1 MeV energy step. The shaded purple region is the equivalent magnetic field region used to calculate the electron deflection. The dashed line at a height = 1 cm is the un-deflected electron trajectory. The solid black line, is the location and size of the phosphor screen. b) The projected deflection height on the phosphor screen vs electron energy.

causing it to phosphoresce. The location of phosphorescence is measured by a CCD camera. In this manner the dipole magnet disperses the electron beam, where the deflection in height is correlated to the electron energy. It should be noted that electrons were dispersed in the horizontal plane, in the direction of the laser field polarization. The deflection height on the LANEX screen vs the electron energy is shown in Fig. 4.8 b). This curve can then be fit to the measured electron deflection, to infer the energies of the accelerated electron beam. As seen in Fig. 4.8 b), at energies greater than 200 MeV, where small changes in deflection correspond to large changes in electron energy, the energy inferred from the electron deflection becomes much more sensitive to the initial angle at which the electron beam enters the magnetic field.

Another important aspect to notice from Fig. 4.8 b), is that the electron deflection, or dispersion, is not linear with electron energy. As a consequence, the initially measured signal vs. deflection height, is not the true spectral intensity of the electron beam. To see this, first consider that the smallest deflection which can be measured is the pixel size of the CCD camera divided by the magnification of the imaging system and is equal to Δy. Now imagine that a continuous and constant deflection signal, of value V, was measured across all deflection heights. Examining the dispersion curve in Fig. 4.8 b), one can conceptually deconvolve this flat measured spectrum into what the actual spectral intensity would look like. To do this, first consider that at a large electron energy, the Δy corresponds to a large range of electron energies. To find the spectral intensity, the constant signal V measured over one Δy needs to be divided and split over this large range of energies. Conversely, at low electron energies, the same signal V, measured over the same Δy is split over a very small range of energies. Therefore, the spectral intensity would be very much peaked up at lower electron energies and fall very fast at high electron energies for a measured spectrum which has a

constant value over a large range of deflection heights.

Analytically, through conserving the S, the total signal, the signal which is measured, $C(y)$, which denotes counts of signal a function of deflected height y, can be transformed into counts of signal as a function of electron energy, $C(E)$, via the following relation,

$$\Delta S \mid_{y_o} = C(y_o)\Delta y_o = \Delta S \mid_{E_o} = C(E_o)\Delta E_o$$
$$C(E_o) = C(y_o)\frac{\Delta y_o}{\Delta E_o} = C(y_o)\frac{dy}{\partial E} \mid_{y_o} \tag{4.6}$$

Using the curve fitting toolbox in Matlab, a power series can be fit to the deflection height y vs electron energy E, shown in Fig. 4.8 b). With the coefficients of the power series, the derivative of the curve fit can be easily made to solve for $dy/\partial E$ as a function of E. This allows Eqn. 4.6 to be solved in a straightforward manner. Note that $C(E)$ is actually counts of signal / electron energy (MeV). Figure 4.9 is a comparison of the measured signal C(y) and the deconvolved spectral intensity C(E). Here C(y) is the measured electron deflection signal and is plotted vs the energy corresponding to the measured deflection height. Using Eqn. 4.6, the spectral intensity, C(E) is recovered from C(y). Notice that at lower energies even though C(y) is decreasing, because of the non-linear dispersion of the dipole magnet, C(E) remains roughly constant.

To measure the amount of charge in the accelerated electron beam, an integrating current transformer (ICT) was used [77]. A current transformer can be thought of a toroidal solenoid. When an electron beam passes through the center of the ICT, the current of the electron beam creates a magnetic field which is perpendicular to the windings of the toroid. The magnetic field induces a current and voltage within the windings primary of the transformer. With in the secondary of the transformer, this current is integrated via some capacitance within the ICT. The voltage associated with the integrated current delivered across some

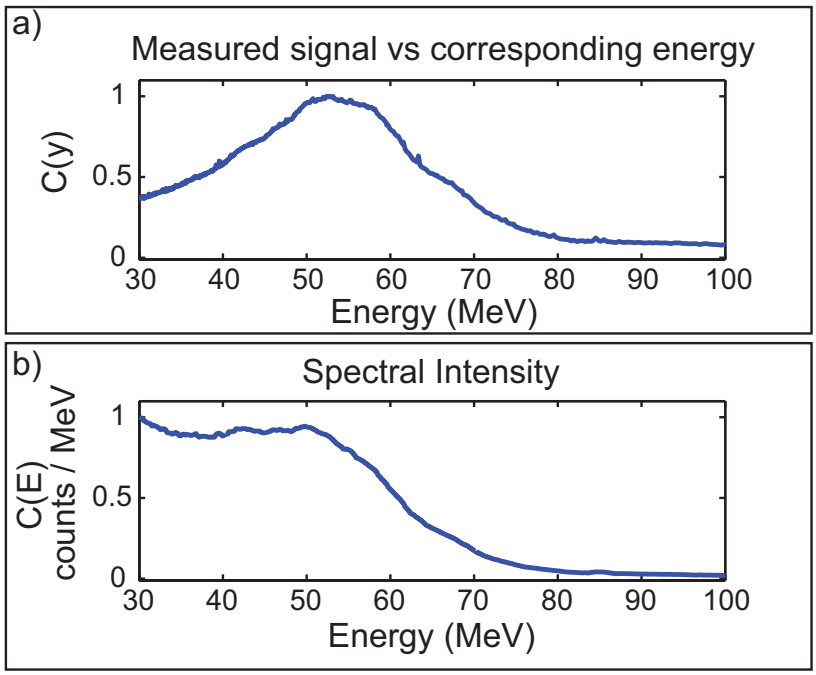

Figure 4.9: a)The measured electron deflection signal, C(y) plotted vs the energy corresponding to the height of deflection. b)The deconvolved spectral intensity C(E) plotted vs energy. Both C(y) and C(E) have been normalized.

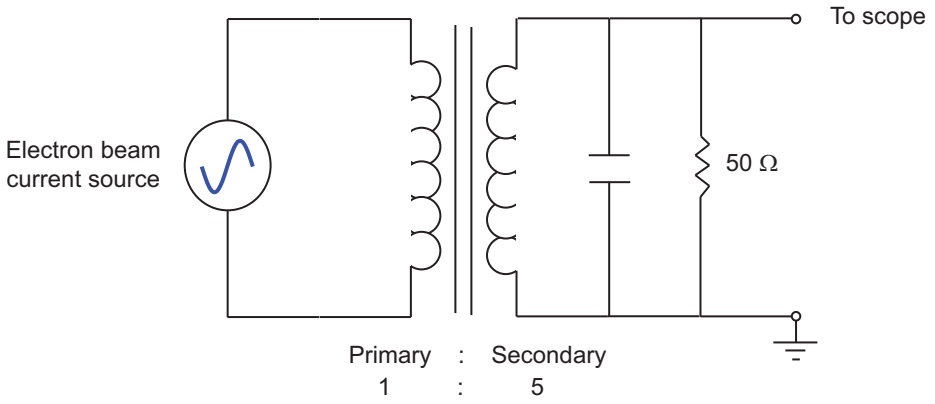

Figure 4.10: A schematic of an integrating current transformer, ICT, with a 1:5 transformer ratio. The electron beam induces a current and voltage with in the primary of the ICT which after being transformer via induction into the secondary windings is integrated across some internal capacitance. The integrated current is then delivered across a 50 Ω internal resistance and the resulting voltage is read out across a oscilloscope.

internal resistance is measured by a fast oscilloscope. A schematic for the ICT is shown in Fig. 4.10. As the name implies, the *integrating* current transformer does not resolve the electron beam current with time. The voltage signal created has a rise time of $\sim$ 20 ns that is independent of the current profile rise time. The measured voltage can be integrated to find the current of the electron beam. The ICT model used in these experiments was ICT-055-070-05:1-H-VAC. The 05:1 in the model number indicates the turn ratio of the ICT. This model had a $S = 5.00\ (V \cdot s)/C$ across a 50 Ω termination, where S is defined as the sensitivity. Different ICT models will have different turn ratios and sensitivities. For the ICT used in these experiments the conversion from measured signal to charge in coulombs is then,

$$\text{Charge(C)} = \frac{\int V(t)dt}{5.0(V \cdot s)}C \tag{4.7}$$

where $V(t)$ is the measured voltage signal which in these experiments is typically $\sim$40 ns long with a peak signal of 5-50 mV.

The experimental setup used to measure the electron charge with the ICT is shown in Fig. 4.11. In this setup the ICT was placed outside the vacuum chamber to reduce the noise on the measured signal. Noise can be created by fields that are induced within ICT that are not related to the electron beam current. Noise sources include electrons that strike the outside of the transformer, and the electromagnetic pulse (EMP) created by the laser pulse interacting with objects it strikes. To minimize these noise sources, the ICT was placed outside the chamber. The electron beam was taken out of the vacuum chamber through a thin mylar window. In front of the mylar window, 50 μm of aluminum was placed to block the laser light. Before the electron beam was sent through the ICT, a low dispersion magnet was used to disperse the electron beam. The low dispersion magnet was built in a similar fashion as the one described above, but with a peak magnetic field strength of 2850 Gauss and an equivalent length of 68 mm. Electrons with energies below 14 MeV were deflected into 3 mm of tungsten. The tungsten beam block stopped electrons from hitting the ICT and creating noise. In this manner the charge above 14 MeV was measured by the ICT. A LANEX screen was placed on the back of the ICT . The phosphoresce from this screen is imaged by a Nikon 50 mm f/1.4D AF camera lens onto a 16 bit image intensified Princeton Instruments PI-MAX CCD camera..

An image of the dispersed electron beam after passing through the ICT is shown in Fig. 4.12. The lower magnetic field of the dipole magnet made resolving energies above $\sim$ 50 MeV inaccurate. Even after taking the aforementioned steps to minimize the ICT signal noise, the measured ICT signal, shown in blue in Fig. 4.13, still contains a significant amount of AC noise. From the ICT manual, it is

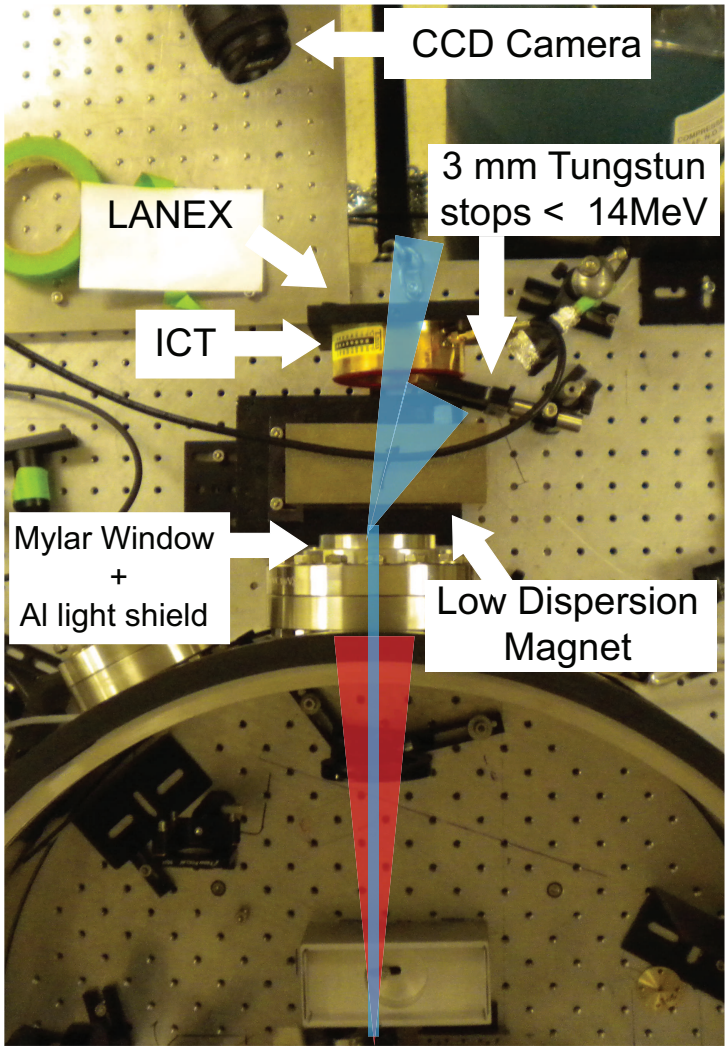

Figure 4.11: The experimental setup used to measure the electron beam charge. The electron beam, shown in blue, is first taken out of the vacuum chamber through a thin mylar window. The laser beam, shown in red, is dumped against a thin 50 μm Al foil. The electron beam then passes through a dipole magnet. Electrons below 14 MeV are deflected into and stopped within 3 mm of tungsten. The remaining higher energy electrons pass through the ICT where there charge is measured. On the back of the ICT a LANEX screen is placed. The phosphoresce from this screen is imaged by a camera lens onto a CCD camera.

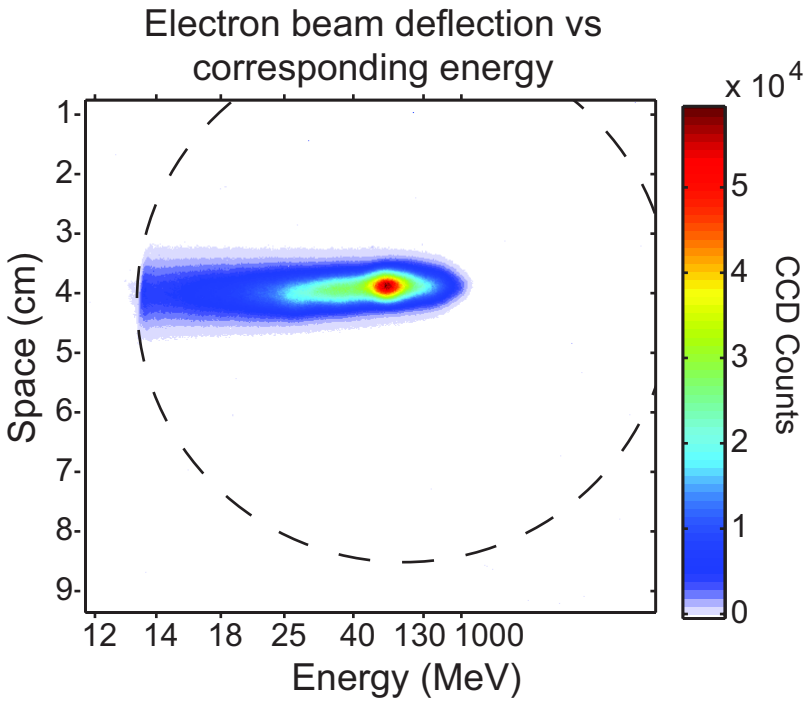

Figure 4.12: An image of the deflected electron location vs energy. The height of deflection has be converted to the corresponding energy. The energy resolution above ∼50 MeV is very poor. The dashed circle corresponds to the approximate ICT location. At lower energies, the ICT was shielded from the electron beam by 3 mm of tungsten which stopped electrons below ∼14 MeV.

known that a clean ICT voltage signal should rise and fall over a time period of ∼40 ns, and should not have an AC modulation on it. To filter out the AC noise, a Fourier transform is taken. The real component of the Fourier transformed signal is shown in Fig. 4.13 b). Here, a super gaussian filter, shown by the dashed red line, can be multiplied with the normalized real and imaginary parts of the Fourier transformed signal to filter out a large portion of the high frequency noise. Re-scaling and then taking the inverse Fourier transform of the frequency filtered signal, recovers the filtered signal in time. The recovered filtered signal in time is shown as the red curve in Fig. 4.13 a). The amount of measured charge for each electron beam was found by using the same super gaussian bandwidth filter and integrating each filtered ICT signal over the same fixed time duration of 44 ns (-6 to 38 ns), denoted in Fig. 4.13 a) by the green circles.

The amount of charge measured by the ICT was compared to the total amount phosphoresce signal created by the electron beam as it passed through the LANEX screen. Figure 4.14 shows that there is a linear relationship between the amount of charge measured by the ICT and the total amount of phosphor signal over a range of electron energies from ∼10-100 MeV. Integrating current transformers have been used to measure the charge of electron beams with pulse widths of ∼1 ps, however there has been a bit of uncertainty on wether ultrashort electrons beams with pulse widths of 10-100 fs as created from LWFAs can be accurately measured with ICTs. While Fig. 4.14 is not an absolute calibration, it appears that for electron beams with sub 100 fs pulse widths, the relative trend in charge as measured by the ICT is in good agreement and linearly proportional to the amount of charge / phosphoresce indicated by the LANEX screen. The measurement was made using Kodak Fast F Lanex film. A Princeton Instruments, PI-MAX intensified CCD camera, with a gain setting of 75 was used to make this measurement. The amount of integrated phosphor signal is proportional not only

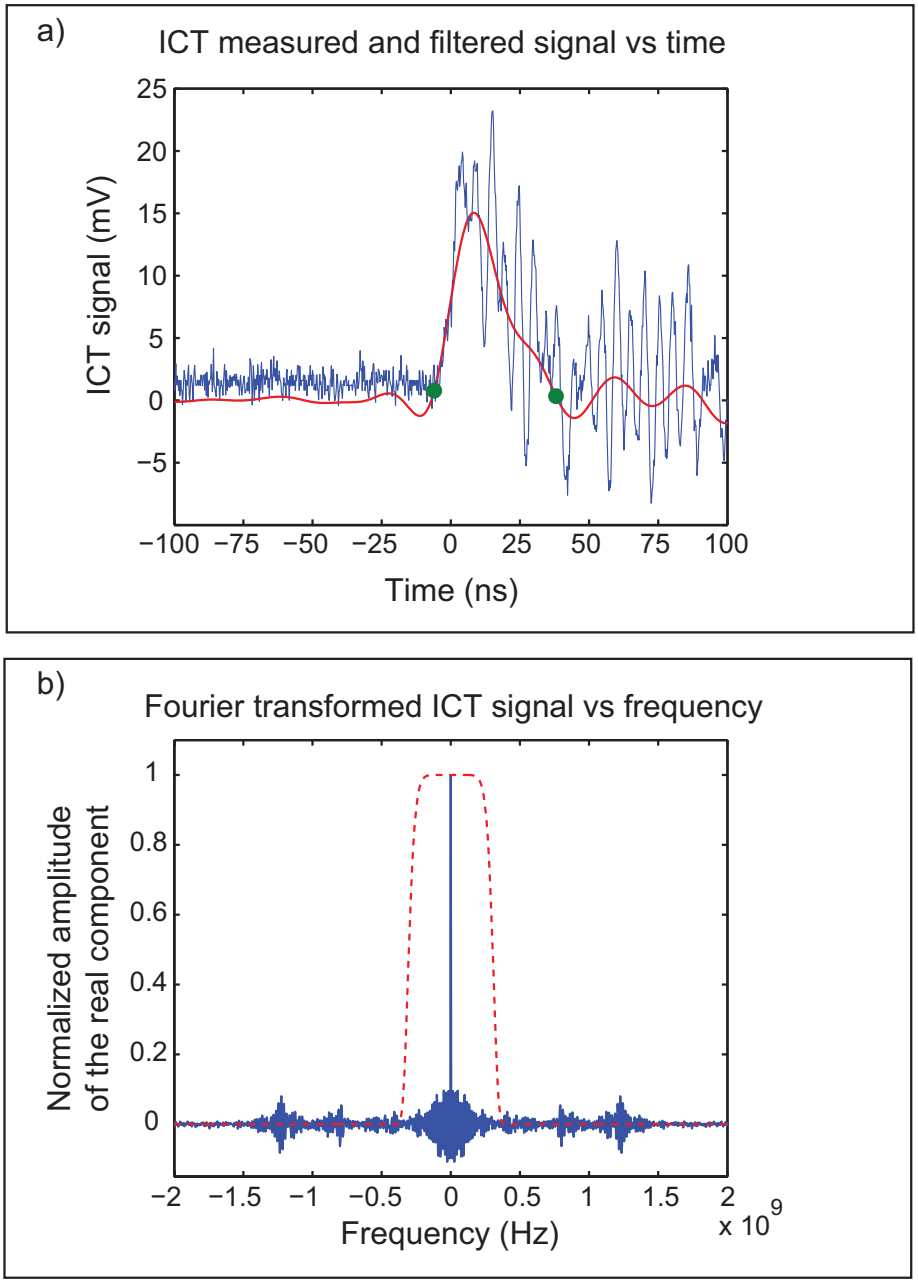

Figure 4.13: a) The raw measured ICT signal vs time shown in blue, and the recovered filtered ICT signal vs time shown in red. The green circles represent the fixed period of time over which the filtered ICT signal is integrated to measure the electron beam charge. b) The real component of the Fourier transform of the ICT signal vs frequency. The red dashed line is the super gaussian filter.

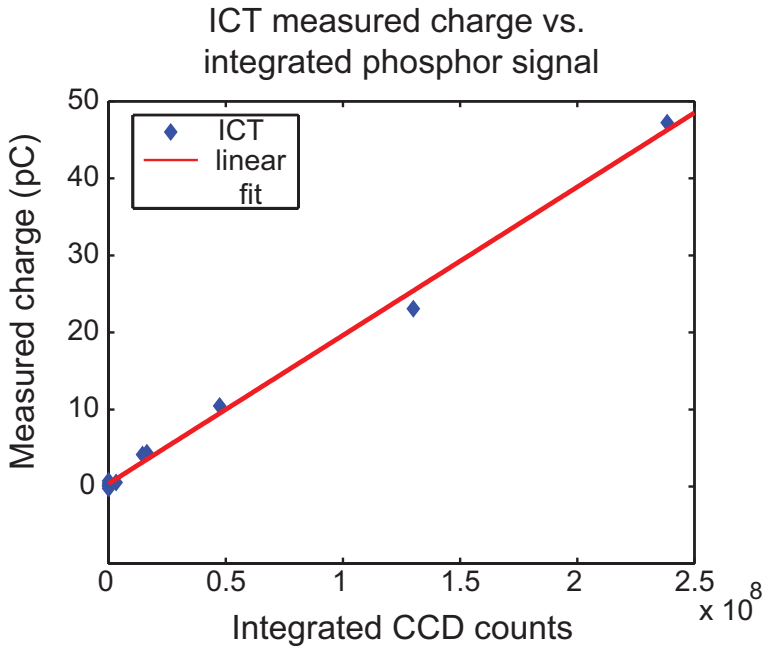

Figure 4.14: The charge measured by the ICT (blue diamonds) vs the total integrated phosphor signal measured by the 16 bit image intensified PI-MAX CCD camera.

to the gain setting of the camera, but also the distance between and the characteristics of the optic used to collect the phosphor signal. Once these variables are fixed, Fig. 4.14 indicates that the phosphoresce of the LANEX film is linearly proportional to the amount of charge in the electron beam. In this experimental setup the lowest amount of charge the ICT could measure was ~ 5 pC. At these charge levels, the CCD camera with a gain setting of 75 could still distinguish the phosphor signal from the background noise. The gain on the CCD camera can be increased from 75 to 200, and if calibrated at this gain setting, in principle could be used to measure charge below 5 Pc.

Using these experimental setups and methods, a study of ionization injection and the properties of the electron beams that were created was undertaken.

CHAPTER 5

Results

To demonstrate the injection of electrons into a laser driven wakefield, using tunnel-ionization of a minority species gas initial experiments were preformed using a 90:10 He:N_2 gas mixture, and a $\sim$2 mm long gas jet which produced a plasma with a peak density of $\sim$1.4x10^{19} cm^{-3} and density profile as shown in Fig. 5.1. Varying the laser a_o between 1.5-2.5 and the P/P_c between 1.5-4, the appearance threshold for the trapping and acceleration of electrons in the gas mix was observed to be lower than that required to self-trap electrons in a pure He plasma with a comparable plasma density profile and peak density. The lower observed a_o and P/P_c threshold for accelerating electrons agrees quantitatively with the model developed for ionization injection earlier in chapters 2-3. In addition to this lower trapping threshold, the intensity threshold for observing accelerated charge corresponded to that required to ionize the 6th and 7th electrons from nitrogen. Furthermore, when accelerated electrons were created from the helium nitrogen gas mixture, an enhanced amount of transmitted blue shifted laser light was also observed. Furthermore this blue shifted light was confined to a narrow guided spot exiting the plasma. This enhancement in blue-shifted light, as well as the intensity threshold corresponding to that required to ionized N^{6-7+}, both indicate that electrons were injected into the wakefield via ionization of the 6th and 7th states of nitrogen. These results were confirmed using 3-D OSIRIS simulations which modeled the interaction using laser and plasma

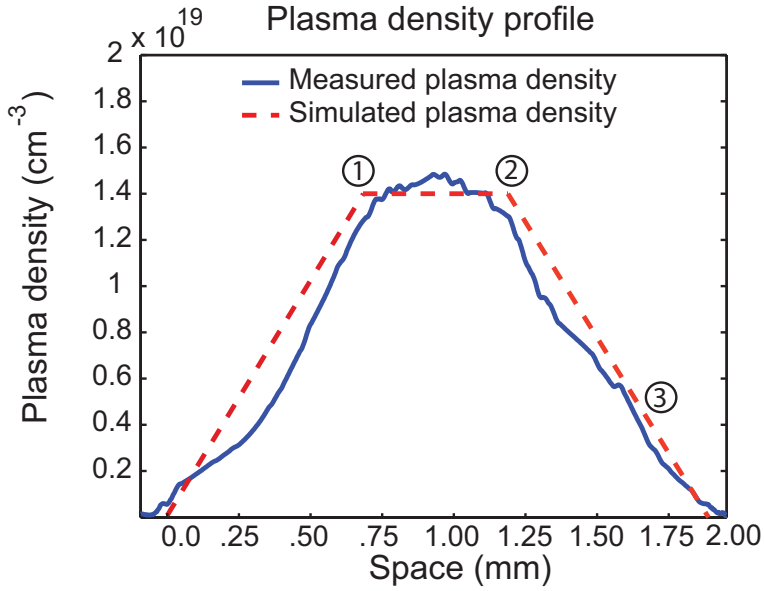

Figure 5.1: An example of the measured plasma density profile shown in blue. The plasma profile was taken from averaged density over a 100 μm boxout down the center of the plasma. The peak plasma density was $\sim$1.4x10^{19} cm^{-3}. The dashed line indicates the simulated plasma profile that was used. As will be discussed later, the circled numbers correspond to locations within the plasma where simulations were used to investigate the laser plasma dynamics in detail.

parameters that were closely matched the experimentally measured values and included the dynamics of ionization using the ADK model. Additionally these simulations allowed the properties of electrons created from the N^{6-7+} ionized states to be isolated and examined. We find that the experimentally measured electron spectra, divergence and relative charge are in good agreement with corresponding observed values created only from electrons originating from N^{6-7+} in the 3-D simulations.

Using the 90:10 He:N_2 gas mixture, the intensity threshold for the trapping of electrons was measured by varying the a_o of the laser at a fixed plasma density

of $\sim$1.4x10^{19} cm^{-3}. Figure 5.2 is a plot of the relative total charge, with energies above 25 MeV, of the dispersed electron beam versus initial a_o. The shaded region of Fig. 5.2 indicates that electron spectra were not observed below an a_o of 1.6. This sharp intensity threshold, which is slightly below the a_o required to ionize the 6th electron from nitrogen, suggests that the trapped and accelerated electrons are indeed from the K shell of nitrogen. At the threshold for observed accelerated charge, the power of the laser pulse was $\sim$1.4 times the critical power for self-focusing (P_c) [47]. Therefore it is likely (and it is observed in present simulations) that the intensity of the laser pulse increased as the initial spot size of 5 μm (1/e field amplitude) is focused by the plasma to the matched blowout radius of $\sim$ 4 μm [20]. This process allows the laser to ionize and inject the 6th electron of nitrogen, even when the initial a_o is just below the corresponding ionization threshold. The increase in total charge with a_o is thought to be due to the larger volume of ionized and injected electrons and due to the ionization of the 7th electron of nitrogen that occurs at higher laser intensities. Figure 5.2 indicates that the trapping threshold and the relative trend in total accelerated charge seen in the experiment are in good agreement with those seen in the simulations. Simulations indicate that while the laser pulse evolves within the plasma, injection and trapping of electrons begins to occur once the laser intensity rises above the ionization appearance intensity for $N^{6+,7+}$. As a comparison, in the blowout regime, previous simulations have indicated that self-trapping of electrons into the first period of the wake requires an a_o of 4.3 [60]. A recent overview of many experiments [58] has found that an a_o of $\sim$3.8 was required to self-trap wake electrons consistently. These vector potentials are larger than the threshold value of a_o seen for ionization trapping of the 6th nitrogen electron here. The measured electron spectra obtained at a laser a_o of 2.35 and 1.64 are shown in Fig. 5.3 a) and 5.3 b), respectively. The broad electron spectrum observed

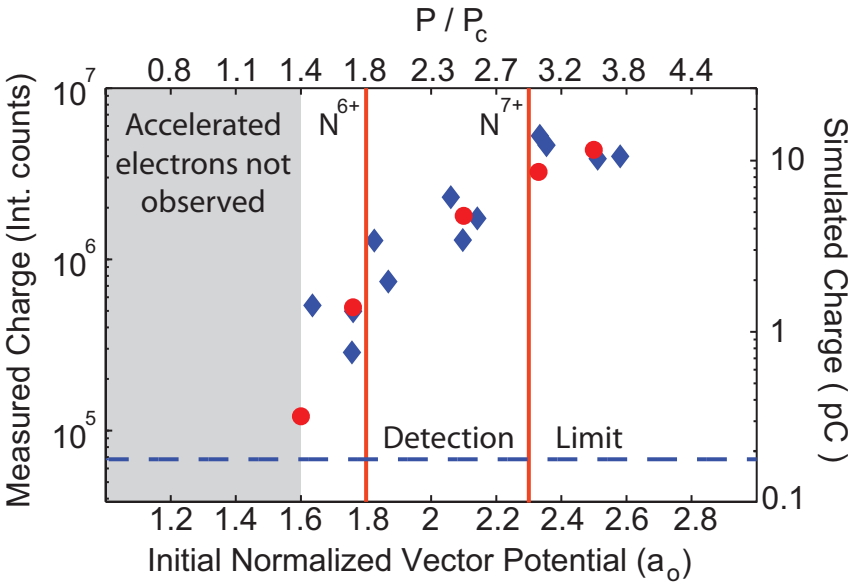

Figure 5.2: Measured (diamonds) and simulated (circles) integrated charge of electrons with energy > 25 MeV vs laser a_o and normalized power P/P_c. Solid lines correspond to the a_o required to ionize the 6th and 7th electron of nitrogen in one cycle of the laser pulse using the ADK model. Dashed line is the experimental signal detection limit. $n_e \sim 1.4 \times 10^{19}$ cm^{-3} ; 9:1 He:N_2 gas mix.

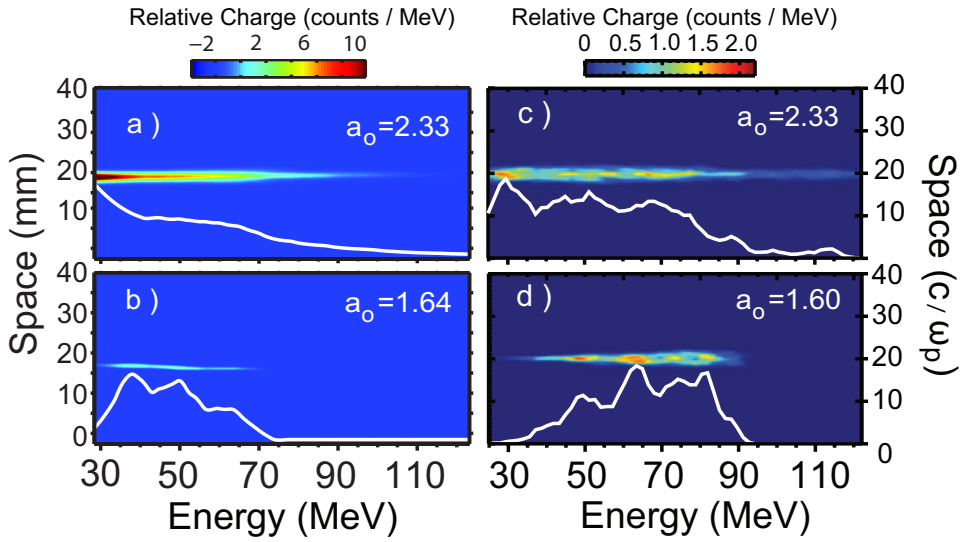

Figure 5.3: A comparison between the observed a) and b) and the simulated c) and d) electron spectra created at a $n_e \sim 1.4\text{x}10^{19}$ cm^{-3} from a 9:1 He:N_2 gas mix.

in Fig. 5.3 a) is consistent with the continuous injection and acceleration of electrons from the K shell of nitrogen. Lowering the laser intensity can limit the distance over which the laser pulse is intense enough to ionize the 6th nitrogen electron into the wake. When the injection of electrons is stopped, the wake will continue to accelerate previously trapped electrons. If a significant amount of acceleration takes place after the injection of electrons has stopped, then there will be an absence of a low energy tail in the observed spectrum as seen in Fig. 5.3 b). In future experiments, a two cell arrangement, where the first cell contains a mixture of two species for injection (He:N_2 for example) and a second accelerator stage containing only one gas (e.g. He) would allow for narrower energy spread beams to be obtained. Electron spectra shown in Fig. 5.3 c) and 5.3 d) are generated using 3-D OSIRIS particle in cell code simulations [78] which included ionization effects using the ADK model [62]. The dimensions of the simulation

were 71 μm X 57 μm X 57 μm with each direction having 3000 X 256 X 256 cells, with 2 electrons per cell. In these simulations, the laser energy, spot size, pulse width, as well as the gas mixture ratio and plasma density profile were the same as the experimental values stated above. By tracking the ionization state in the simulations, it was found that the two helium and the outer five electrons of nitrogen only formed the wake and were not trapped. The simulated spectra shown in Fig. 5.3 c) and 5.3 d) are comprised only from electrons from the K-shell of nitrogen. This confirms that it is indeed electrons from K-shell that are injected and accelerated preferentially due to being ionized into the wakefield.

The simulated spectra at both laser intensities are in qualitative agreement with the spectra observed in the experiment. In both the experiment and simulations, the energy spread of the accelerated electrons is found to decrease as a_o is decreased, from being continuous at a_o of 2.33 to $\Delta E/E \simeq .6$ at an a_o of 1.6. With $n_e = 1.4\text{x}10^{19}$ cm^{-3} and $a_o = 2.3$, the maximum energy gain given by the 3-D nonlinear theory [28], $E(\text{MeV}) \approx (1/3)(\omega_o/\omega_p)^2 a_o$, is 92 MeV, which is close to the observed value. Here ω_o and ω_p are the laser and plasma frequency, respectively. Simulations indicate that the continuous electron ionization and injection leads to a decrease in the potential of the wake due to beam loading. This can eventually limit the amount of charge trapped as well as the final energy accelerated electrons reach. On the other hand, in theory, beam loading could be used advantageously to produce narrow energy spread beams.

To gain a better understanding of the trapping dynamics of the experiment, a comparison of the laser, wake and accelerated electron evolution at three different locations within a 3-D simulation was preformed. The simulation was preformed using a laser a_o of 2.1, spot size of 6 μm, pulse width of 45 fs and with the 90:10 He:N_2 gas mixture. The plasma density profile and the three specific locations

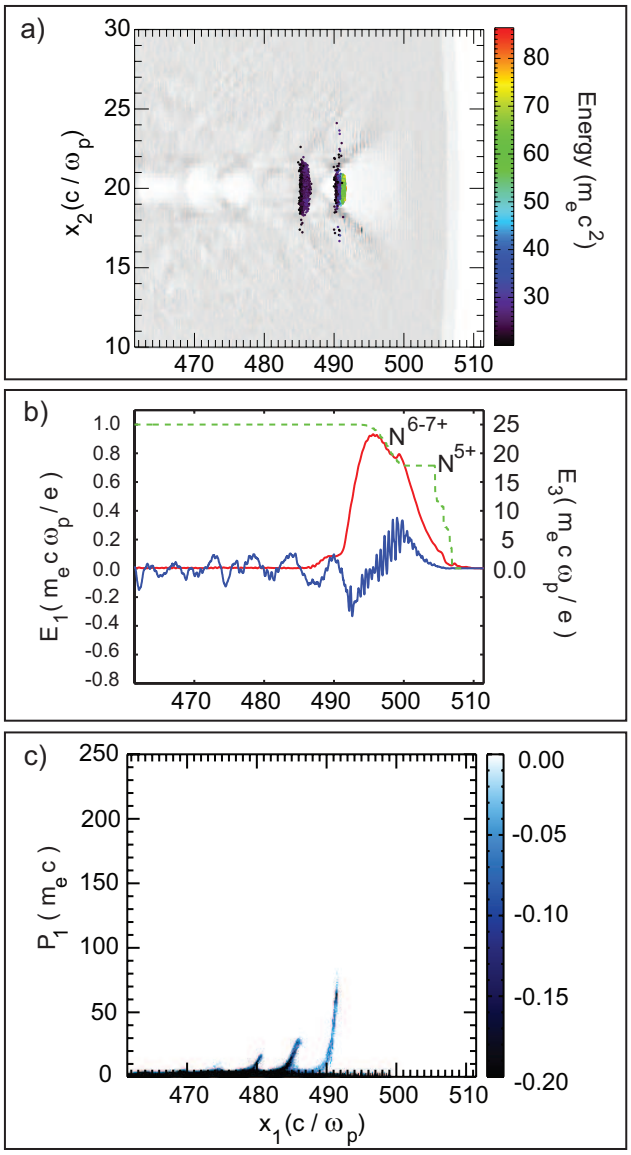

Figure 5.4: The evolution of the wake, accelerated charge and laser taken from a 3-D simulation taken at a location corresponding to (1) shown in Fig. 5.1. a) Electrons from N^{6-7+} shown in color, overlaid with the helium charge density, shown in grey. b) The on axis electric field of the wake E_1 (blue) and and laser pulse envelope E_3 (red). The dashed green line indicates the ionization state of N. c) The longitudinal momentum of electrons from N^{6-7+} plotted vs space.

(1-3) within the simulation at which these quantities are compared are shown in Fig. 5.1. From this simulation, and from observations taken from similar 2-D simulations, it is concluded that electrons are continuously injected, accelerated and subsequently decelerated throughout the interaction. Furthermore, for a 10% concentration of nitrogen, it is observed in simulations that ionization locally depletes the amplitude of the laser pulse, which in turn may be effecting the amplitude of the wake that is driven. Near the end of the interaction, beam loading of the accelerating field is observed and thought to be effecting final accelerated energy spectrum of electrons.

Examining the 3-D simulations, it appears that injected electrons from N^{6-7+} begin to be trapped into the first period of the wakefield within the rising edge of the density profile $\sim$400 μm into the simulation. Figure 5.4 shows the wake and laser profiles as well as the injected electron momentum $\sim$700 μm into the plasma at the beginning of the density plateau. As shown in blue in Fig. 5.4 a) and b) the wake structure and longitudinal accelerating field at this point in the simulation are not yet well defined. This could be due to the rising density profile and to the spot size of the laser initially being slightly larger than the matched spot size. Some time / space may be need for the laser to self-focus to the matched spot size and drive a stronger amplitude wake. The ionization contour of nitrogen is shown by the dashed green curve in Fig. 5.4 b). It shows that electrons from N^{6-7+} are being injected and trapped into the first period of the wakefield. Electrons from the N^{6-7+} ionized states which are injected, but not trapped into the first period of the wakefield, are thought to be streaming back through the following accelerating structure. Some of these electrons are trapped into the second and third periods of the wakefield as shown in Fig. 5.4 a) and c). These trapped and un-trapped electrons that stream back through the wakefield might also be contributing to the lower wake amplitudes seen in Fig. 5.4

a) and b). For this reason, it might be advantageous to lower the concentration of nitrogen to helium in the gas mixture. Additionally the laser profile, shown in red in Fig. 5.4 b), indicates a local depletion of the laser amplitude corresponding to the location at which the N^{6-7+} states are ionized. The local depletion of the pump via ionization is unavoidable, but should be minimized to maximize the wake amplitude and pump depletion length. Experimentally observed charge measurements indicate that the difference in the amount of accelerated charge using the 90:10 and 95:05 He:N_2 gas mixtures are minimal. Therefore it is thought that a 10% concentration of nitrogen gas may be too large, increasing the rate at which the pump is depleted while injecting an excess of un-trapped electrons that unnecessarily lower the wake amplitude.

The longitudinal momentum of trapped electrons reached at the end of the density plateau is shown in Fig. 5.5 c). As shown in this figure and as previously discussed, the momentum of electrons within each period of the wakefield is continuous, as electrons are continuously injected, trapped and accelerated within each period. Comparing the longitudinal momentum at the end of the density plateau to that at the beginning (Fig. 5.4 c)) it is observed that the maximum longitudinal momentum reached in the first period of the wakefield increases with propagation distance, but that the total number of accelerated charge above $\sim$10 MeV in the first period decreases. It is thought that electrons which were injected earlier in the interaction (at or before location 1 in Fig. 5.1) might have reached their dephasing length and subsequently lost energy. It has been observed from electron trajectories in 2-D simulations that many of electrons are unable to be re-trapped into the first period of the wake after reaching a dephasing length and being decelerated. The loss of accelerated charge due to dephasing is thought to be one reason for the decreased amount of accelerated electrons in the first period of the wake observed at the end of the density plateau. Figure 5.5 a), shows the

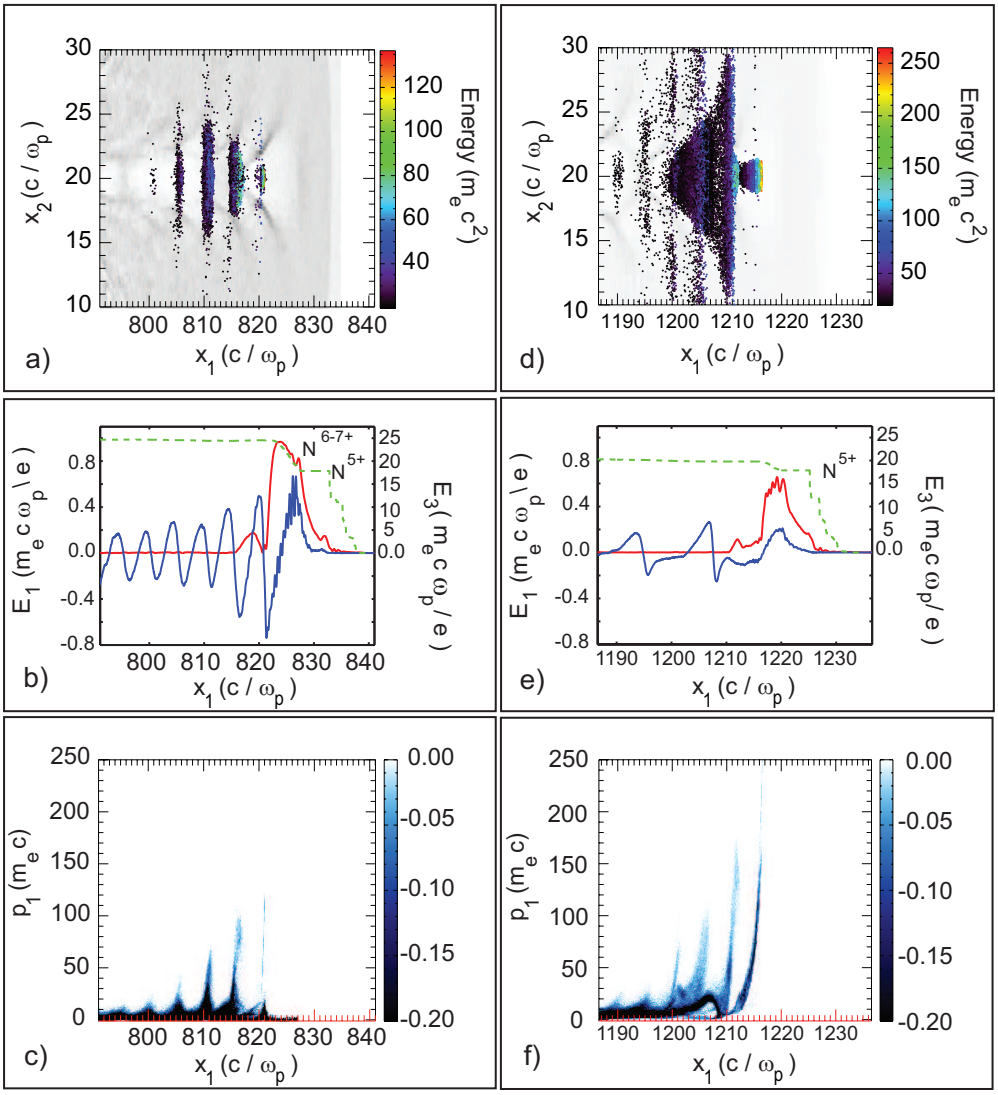

Figure 5.5: The evolution of the wake, accelerated charge and laser. The simulated data on left / right hand column is taken at a location of (2) / (3) shown in Fig. 5.1. a) and d): Electrons from N^{6-7+} shown in color, overlaid with the helium charge density, shown in grey. b) and e): E_1 (blue) and E_3 (red) are the on axis electric field of the wake and laser respectively. The dashed green line indicates the ionization state of N. c) and f): Longitudinal momentum of electrons from N^{6-7+} plotted vs space.

charge density of the wakefield and the location of electrons from N^{6-7+} that have reached energies of 10 MeV or more. This figure shows that indeed some electrons from N^{6-7+} are leaking out of the each period of the wakefield. Even with some loss of trapped electrons, if constant and continuous trapping of injected electron is occurring then it would seem that after some distance the spectrum and number of electrons would remain quasi-constant. One possibility for why the number of electrons in not constant is that the wake potential and the profile of the laser pulse both evolve and this can turn the trapping of electrons on and off as the location of the injection changes and the wake amplitude oscillates. These effects are particularly relevant within the density up and down ramp, where the plasma density is changing somewhat rapidly.

Figure 5.5 b) indicates that at the end of the density plateau a relatively strong and coherent wake accelerating structure is being driven. This figure shows that the profile of the laser has been compressed in time, and that the amplitude of the field is still strong enough to inject electrons via ionization into a favorable location within the wakefield. The laser and accelerating field amplitudes close to the end of the plasma density down ramp, are shown in Fig. 5.5 e). This figure shows that the laser amplitude has now decreased to below the level required to ionize a significant amount of N^{6-7+}. Examining the accelerating field E_1, it appears that a significant amount of beam loading has occurred, reducing and flattening out the accelerating gradient of the wake on axis. In general close to the end of the density down ramp there is a decrease in the amplitude of the wake due to the decrease in the plasma density and laser amplitude and possibly due to the beam load of the wakefield. As seen in Fig. 5.5 d), the decrease in wake amplitude in turn allows a large amount of low energy electrons to escape or leak out of the wakefield. The decrease in plasma density can also cause a change in phase for trapped electrons. Figure 5.5 e) shows the plasma

wavelength has increased and in Fig. 5.5 f) it can be seen that a portion of electrons from the second period of the wakefield have 'jumped' into the first period at a location $x_1 \approx 1210$ (c/ω_p). Figure 5.5 f), also shows that a much larger portion of electrons in the second period have dephased and rolled over in phase space at $x_1 \approx 1207$ (c/ω_p). Figures 5.5 d) and f) indicate that electrons which have gained the most longitudinal momentum remain on-axis and within the first period of the wakefield. Figures 5.4 and 5.5 give an impression of the various laser and wake dynamics which occur during the process of ionization injection and trapping. However more work, including varying the gas mixture ratio, optimizing the laser and plasma density profile and tracking the trajectories of trapped and un-trapped electrons is needed to fully understand the trapping process and optimize the properties of the accelerated electron beam.

Figure 5.6 shows three electron beam spectra obtained from the 95:05 He:CH_4 gas mixture. The large step in the ionization potential from C^{4+} (64.5 eV) to C^{5+} (392 eV) creates the step in space allowing electrons C^{5-6+} to be injected directly into the wakefield. The lower ionization potential of carbon permits electrons to be injected into the wake using even lower laser powers as compared with injecting electrons from the K-shell of nitrogen. For our laser parameters, the BSI model [79] indicates that C^{5-6+} will be created using an approximate a_o of 1.3-1.7 respectively. It was found that when using the He:CH_4 gas mixtures, that the success of the experiment was even more sensitive to the level of pre-pulse. This is due to the relatively large amount and the low ionization potential of the hydrogen contained within the CH_4. The plasma density profile for each spectra was $\sim$2 mm in length and triangular in shape with a peak plasma density of $\sim$1.7x10^{19} cm^{-3}. In Figures 5.6 a)-c) the ratio of P/P_c is shown for each spectra and indicates the relative strength and rate of self-focusing which occurs. It is thought that when P/P_c is larger, the evolution of the wake and laser occurs

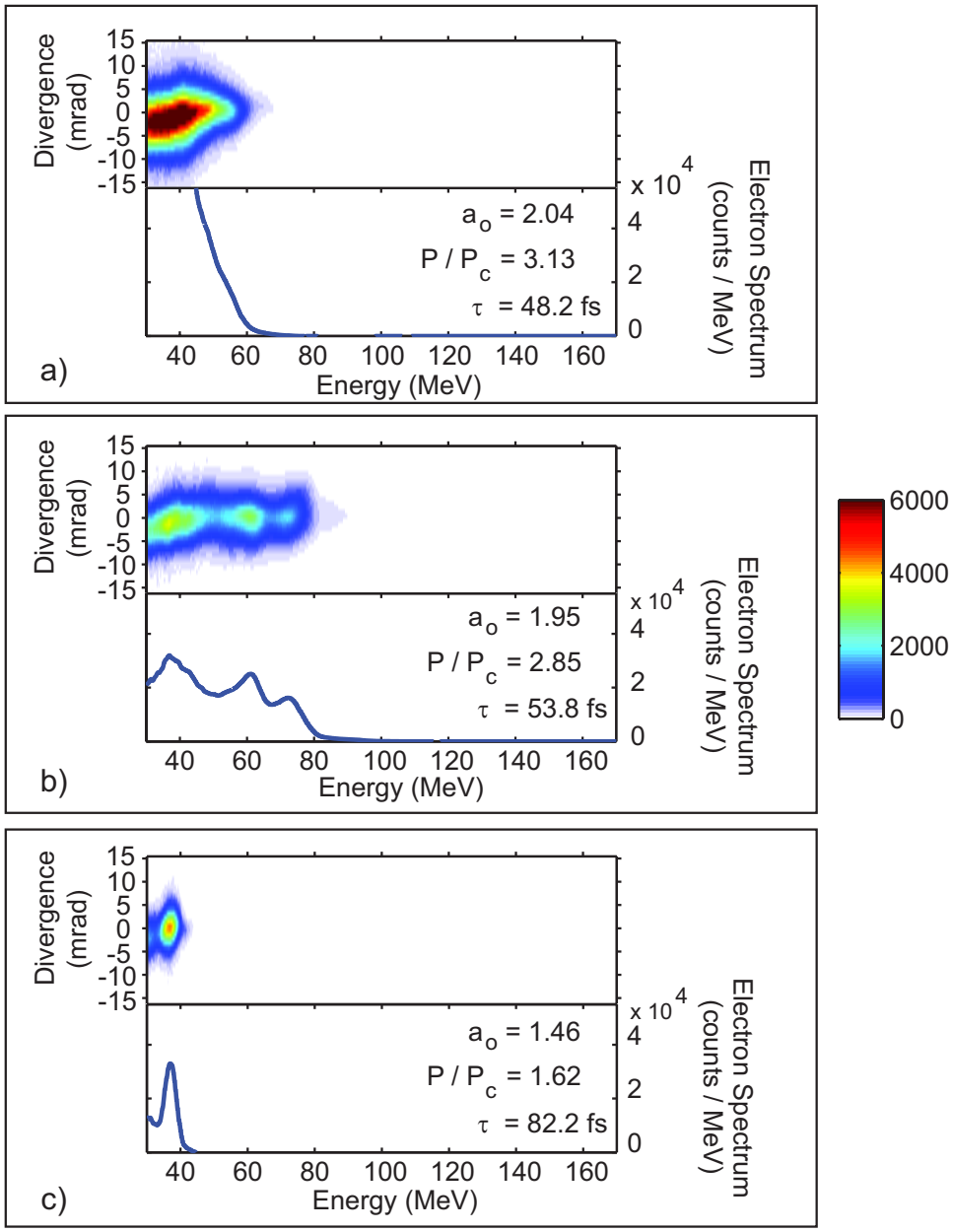

Figure 5.6: a)-c) The electron energy spectrum and the integrated spectral intensity plotted vs electron energy. Each energy spectrum was created from a 95:05 mixture of He:CH_4 at a peak plasma density of 1.7x10^{19} cm^{-3}. The laser a_o, pulse width (FWHM) τ and ratio of P/P_c are shown for each spectrum. The spectral intensity has been summed over a 30 milliradian range of angles.

more quickly, causing the trapping and subsequent dephasing of electrons to occur sooner within the plasma. This effect could explain why the spectrum in Fig. 5.6 a) has a large amount of charge piled up at a relatively lower energy, while the spectrum shown in Fig. 5.6 b), at a slightly lower P/P_c has a lower amount of peak charge, but has the charge spread out over a range of higher energies. Again, as previously discussed, continuous electron beam spectra may not be observed as it is thought that the long density down ramp at the back of the density profile limits the distance over which injection of electrons via ionization can occur.

The spectrum shown in Fig. 5.6 b) shows three distinct peaks in the electron spectrum. It is thought that each of these peaks corresponds to the electrons originating from the first, second and third periods of the wake as shown in the momentum vs space plot in Fig. 5.5 f). Figure 5.6 c) shows the a narrower electron spectrum created when the a_o of the laser was reduced to $\sim$1.5 by stretching the pulse width, τ to $\sim$80 fs. This electron spectrum had a peak energy of 37 MeV and a $\Delta E/E$ (FWHM) of $\sim$12%. The narrower spectrum could be caused by the reduced a_o of the laser. The lower a_o could reduce the amount of electrons from C^{5+} that are created and decrease the length over which these electrons were injected into the wakefield. Additionally the lower wake amplitude / potential driven by the lower a_o of the laser might of limited the phase space over which injected electrons could be trapped, allowing a narrower energy spectrum to be created. In addition to the smaller energy spread, the spectrum shown in Fig. 5.6 c) had a 2.7 mrad ($e^{-\frac{1}{2}}$) divergence.

A mixture of 95:05 He:N_2 gas was also used in these experiments. In general, electron spectra with similar energies, divergences and charge were observed from the 95:05 He:N_2 gas mix as was from the 90:10 He:N_2 gas mix. In order to reach higher accelerated electron energies, the plasma density needed to be lowered to

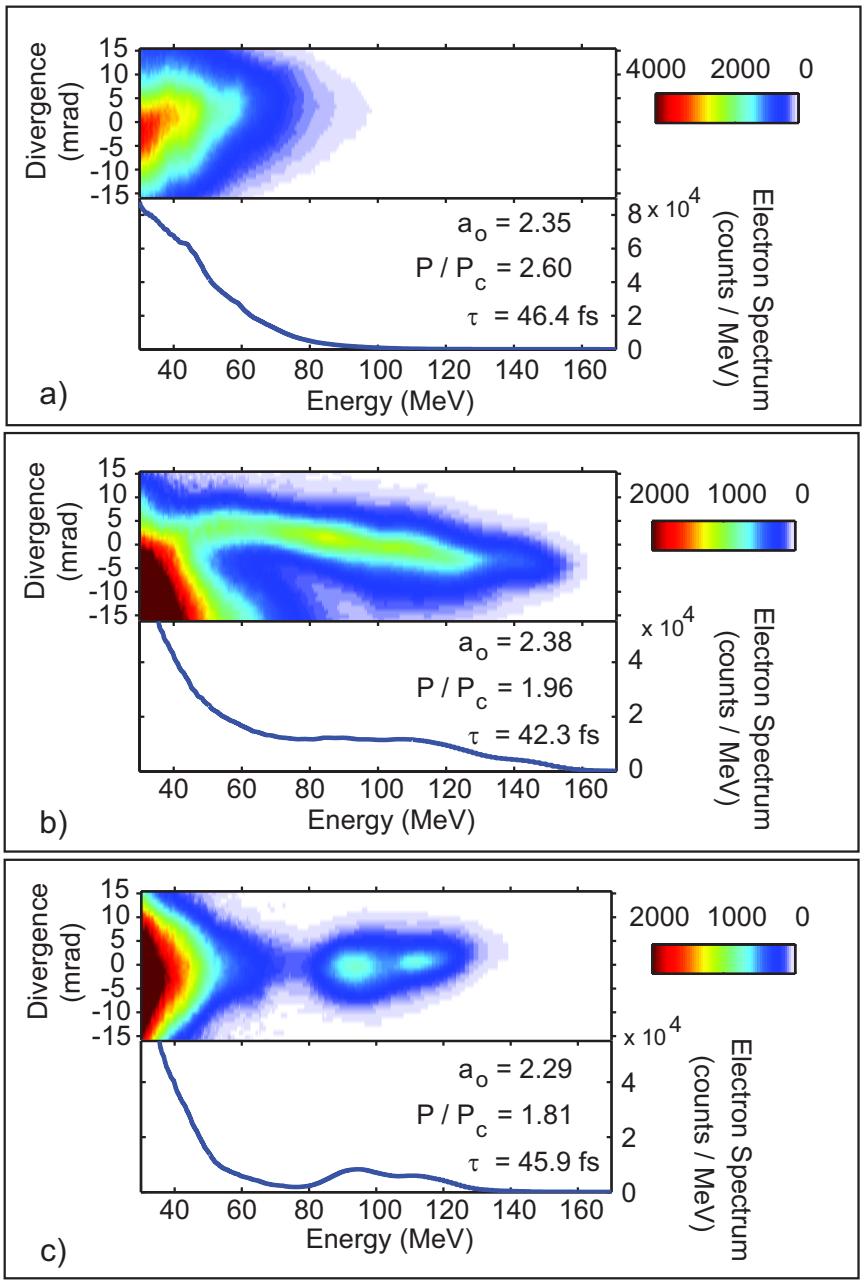

Figure 5.7: a)-c) Electron energy spectrum and the integrated spectral intensity (over a 30 mrad) plotted vs electron energy. These spectra where observed using a 95:05 He:N_2 gas mix and a gas jet with a 3 mm opening. The plasma density in frame a) was lowered from 1.1 to .85x10^{19} cm^{-3} in frames b)- c).

increase the dephasing length. Unfortunately the 2 mm conical gas jet nozzle was unable to produce a flat plasma density profile below $\sim$1.2x10^{19} cm^{-3}. In order to reduce the plasma density, a conical nozzle with a .5 mm throat and a 3 mm opening was used. Using this 3 mm nozzle, a plasma density profile with a $\sim$ 600 μm up ramp, followed by a $\sim$2 mm plateau and a $\sim$600 μm down ramp could be created with lower plasma densities down to 7.5x10^{18} cm^{-3}. The average plasma density of the plateau for the electron spectrum shown in Fig. 5.7 a) was 1.1x10^{19} cm^{-3} and was reduced to 8.5x10^{18} cm^{-3} for the spectra shown in 5.7 b) and c). The spectra shown in Fig. 5.7 represent some of the most commonly observed spectral shapes from the 95:05 He:N_2 gas mixture. Figure 5.7 a) shows the spectrum observed at a P/P_c ratio of 2.35. This spectrum has a larger divergence, more charge and a lower peak energy that the spectra observed with lower ratios of P/P_c in Fig. 5.7 b) and c). Spectra with continuous energy spreads, as observed with the 2 mm nozzle and 90:10 He:N_2 gas mixtures were also observed. An example of such a spectrum is shown in Fig. 5.7 b). The energy spread of this spectrum extends out to larger energies than were observed in using the 2 mm nozzle. It is thought that the increase in the maximum observed energy is due to the lower density and longer dephasing length obtainable using the 3 mm long nozzle. In addition the spectrum in Fig. 5.7 c) shows that it was possible to observe an electron feature with a a slightly narrower energy spread at a central energy of $\sim$100 MeV. Again it is thought that the spectral shape depends how soon trapping and the subsequent dephasing of electrons occurs. For a laser a_o of 2, at a plasma density of 8.5x10^{18} cm^{-3}, a maximum energy gain of $\sim$130 MeV is predicted using Eqn. 2.24. The maximum electron energy observed in the spectra shown in Fig. 5.7 b) and c) are in reasonable agreement the maximum predicted energy gain.

In Fig. 5.7 b) a slight $\sim$5-10 mrad tilt in the electron beam spectrum is

observed. In addition to this tilt, there is a low energy, relatively high charge, and large divergence component to the electron spectrum shown in Fig. 5.7 b) and c). This low energy component is thought to be from charge trapped into the back buckets of the wakefield, as has been seen in simulations (see Fig. 5.5 f)). In Fig. 5.7 b) the low energy component is offset from the tilted higher energy component. For this particular spectrum, the offset of the low energy feature, as well as the tilted higher energy spectral component are thought to indicate that a stable, symmetric wake is not driven throughout the plasma. Pump depletion of the laser can cause an unsymmetrical wake to be driven. The resulting unsymmetrical focusing force is capable of putting a tilt on the electron energy spectrum.

Figure 5.8 shows the spectrum of the laser pulse measured after propagating through a plasma created from pure helium gas and the He:N_2 gas mix close to the threshold intensity to produce N^{6+}. Transmitted spectra contain frequencies not present in the vacuum laser spectrum. Locally the frequency of the laser pulse can be increased and decreased by the wake via photon acceleration and deceleration [49]. Additionally, ionization of the gas causes an increase in the local electron density which further blue shifts laser frequencies [80]. The spectra were measured by image relaying the exit plane of the plasma onto the slit of an imaging spectrograph. The self-guided portion of the transmitted spectrum shown in Fig. 5.8 was much brighter than the unguided spectrally blue shifted laser light associated with the initial ionization process that forms the plasma (not seen here). Experimental constraints did not allow for the simultaneous use of a LANEX screen and spectrograph. Therefore, a surface barrier detector (SBD) was used to indirectly detect the presence of electrons by monitoring the x-ray Bremsstrahlung radiation created from collisions between accelerated electrons and components in the vacuum chamber.

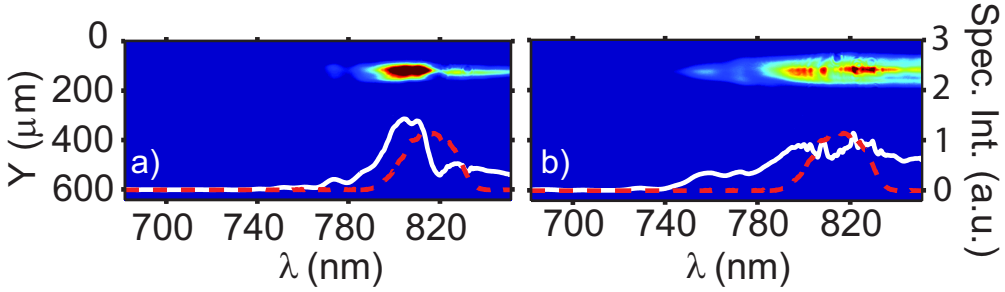

Figure 5.8: The measured spectral intensity of the laser pulse (solid line) observed after propagating through a plasma created from pure helium gas (a) and from a 9:1 He:N_2 gas mix (b). For both spectra n_e was $\sim$ 1.5x10^{19} cm^{-3} and $a_o \approx 1.65$. The dashed line is the normalized spectral intensity of the laser.

If the laser pulse remains well guided as it ionizes and injects electrons into the wake, then the guided portion of the transmitted spectrum from the He:N_2 gas mix is expected to show a greater blue shift than in pure helium. This is indeed observed in our experiments. A strong SBD signal was observed in conjunction with the extended blue shifted spectrum of the transmitted laser pulse from the He:N_2 mix shown in Fig. 5.8b. Below an a_o of 1.6 this additional blue shift in the transmitted laser light in the He:N_2 plasma is not observed.

The divergence for accelerated electron beams is expected to be low near the injection threshold, as electrons are predominantly ionized on axis near the peak laser intensity and do not undergo large betatron oscillations [81]. However, as a consequence of being ionized within the field of the laser, trapped electrons will gain an additional amount of momentum with a component in the direction of the laser field polarization [67, 82]. This effect leads to a beam with an asymmetrical divergence (3 mrad vs 6.3 mrad) as shown in the inset of Fig. 5.9. Additionally, Fig. 5.9 indicates that the divergence transverse to the laser polarization initially remains relatively constant for a_o <2.3, but subsequently increases as the laser

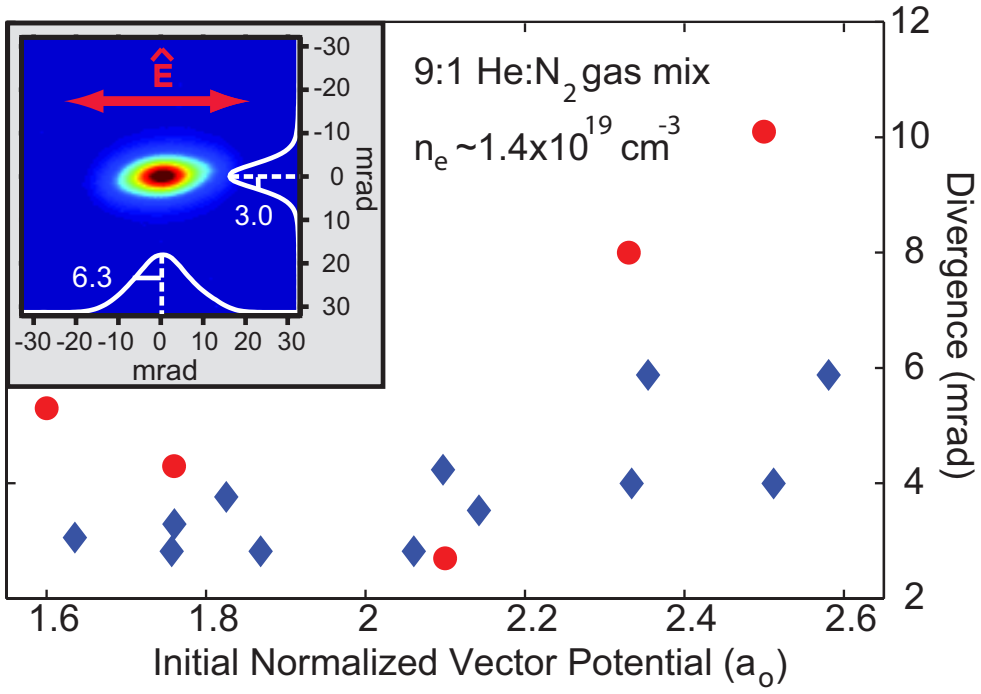

Figure 5.9: Measured (diamonds) and simulated (circles) electron beam divergence ($e^{-1/2}$) transverse to the laser polarization vs laser a_o. An undispersed electron beam ($a_o \approx 2.1$) is shown inset, here the arrow indicates direction of laser polarization.

a_o is increased. A possible explanation for this trend, which is also seen in simulations, is that as a_o is raised, electrons are ionized further off axis and experience a larger radial ponderomotive force from the laser which leads to larger beam divergences.

While the divergences presented here are reasonably small, ionization injection could potentially be used to obtain beams with even better divergence. If the amplitude and profile of the laser pulse can be shaped such that the electrons are only ionized on axis and over a very small volume, then the amount of transverse momentum gained from the wakefield is expected to be very small. Furthermore, if the laser pulse profile is made to be asymmetric, with a longer rise and quicker fall in time, then the divergence of the accelerated electron beam can be further reduced as now the envelope of the laser field will not overlap the location at which electrons will be trapped. An advantage of using an asymmetric laser pulse with a longer leading edge, instead of just a very short laser pulse, is that electrons will be ionized further back towards the center of the wakefield. This will allow these electrons to experience a larger available potential difference, meaning that they can be trapped into a wake with a smaller absolute wake amplitude using less laser power.

Figure 5.10 shows the envelope of an asymmetric laser pulse and the wake potential that is driven taken from a 2-D OSIRIS simulation. The intensity of the laser profile had a 30 fs rise and a 10 fs fall. The laser was focused down to the matched spot size of 4.5 μm with a peak a_o of 2.5. The plasma density was 1.4x10^{19} cm^{-3} and a mixture of 99:1 % helium to nitrogen was used. Compared to simulations where a longer symmetric laser pulse with a 45 fs pulse width, the asymmetrical laser pulse profile did lead to a reduction of electron momentum in the direction of the laser pulses polarization as expected. However, the laser a_o

in this simulation was 2.5, and created a large volume of injected electrons from the N^{6-7+} ionized states. Therefore in this simulation the laser a_o was not optimized to produce an electron beam with a very small transverse momentum. The electron trajectories shown in black in Fig. 5.10 do no accurately represent the trajectories or transverse momentum of the majority of trapped electrons in this simulation. The trajectories shown were chosen to illustrate the concept that electrons created on axis, and trapped outside of the laser field will gain very little transverse momentum. While controlling the ionization injection volume can reduce the transverse momentum gained from the wakefield, as previously mentioned, electrons will gain transverse momentum as a result of being ionized within the field of the laser. An electron ionized at the peak instantaneous vector potential of the laser can gain up to energy up to $2U_p$ in the transverse direction, where U_p is the ponderomotive potential of the laser. However the majority of electrons are created via ionization at low values of A (i.e. near the instantaneous peak of the electric field) and will gain much less than U_P [65]. For the parameters of the laser used in this work, $U_p \approx 1$MeV. If the majority of trapped electrons retain a few hundred KeV of energy in the transverse direction from being ionized and gain a negligible amount of transverse energy from the wakefield, then divergences of less than 1 mrad can be achieved if longitudinal electron energies of $\sim$500 MeV are reached.

Experiments were also preformed at similar densities and comparable laser powers using pure helium. Weak electron spectra were occasionally observed over a range of P/P_c from 2 to 4 but the energy, divergence and energy spread of the spectra had large variations and were irreproducible. Simulations indicate that for our experimental parameters, the spectra produced from pure helium plasmas originate from electrons that are trapped into the 2nd and 3rd periods of the wakefield.

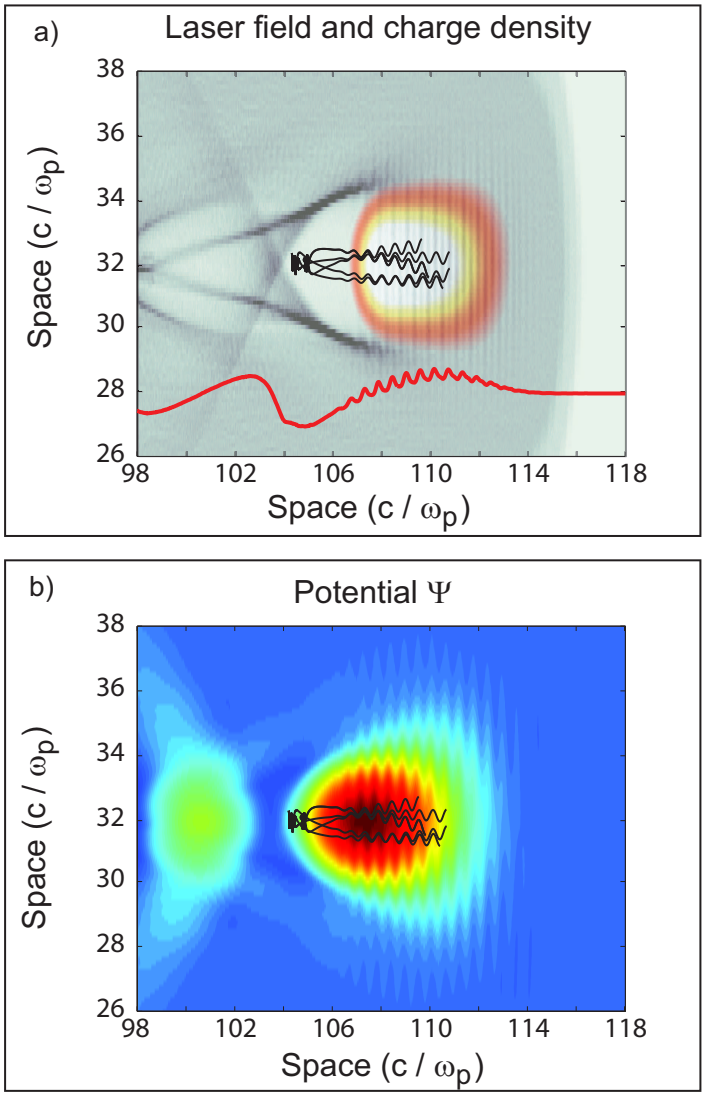

Figure 5.10: a)The envelope of the electric field, shown in color, with the He charge density shown in grey scale vs space. b) the normalized wake potential created vs space. A few selected trajectories of injected electrons from the N^{6-7} ionized states with small transverse momentum are shown in black. These trajectories illustrate the idea of using a asymmetrical laser pulse and limiting the injection ionization volume to produce a beam with a small divergence.

Initial measurements of the electron beam charge were made by placing the ICT inside the vacuum chamber. To stop low energy electrons and transmitted laser light from striking the windings of the ICT, a 1.59 mm thick aluminum shield with a on axis 44.25 mm diameter circular hole was placed in front of the ICT. The aluminum shield stoped electrons with energies below ∼1 MeV from striking the ICT while the hole in the shield allowed the un-deflected electron beam to pass through the ICT. With this setup, the ICT measured more than a nanocoulomb of charge coming out of the LWFA when using the 90:10 He:N_2 gas mixture. It is thought that the majority of this charge comes from electrons with less than 1 MeV of energy that are created by the LWFA. In an attempt to measure the amount of charge at higher electron energies, the .91 T dipole magnet was placed in front of the ICT in order to deflect the lower energy electrons. The dipole magnet and ICT were setup such that only electrons with energies greater than ∼30 MeV passed through the ICT. Unfortunately due to the continuous nature of the electron spectrum, electrons with energies below 30 MeV struck the windings of the ICT creating so much noise, that a charge signal could no longer be measured.

To reduce the noise, the ICT was placed outside the chamber. The first setup used to measure the charge was almost identical as the one shown in Fig. 4.11, except initially the electron beam was taken through a 5 mm thick fused silica glass window and no dipole magnet was used to deflect low energy electrons. The glass window stopped electrons below ∼3 MeV from exiting the vacuum chamber. In this configuration the accelerated charge above 3 MeV created from the 90:10 He:N_2, 95:05 He:N_2 and 95:05 He:CH_4 gas mixtures was measured. The measured charge vs the ratio of P/P_c for these measurements are shown in Fig. 5.11. These charge measurement were made using the conical gas jet with a diameter of 2 mm and over a range of laser powers and plasma densities. The plasma density

profile varied and was found to be dependent on the backing pressure of the gas, the height above the nozzle at which the laser was focused, and the type of gas used. The density profile that was used to calculate the critical power was obtained by averaging the longitudinal density profile over 100 μm in the transverse direction. Over the range of gas pressures, heights and gas mixtures used, the plasma density profile fluctuated considerably. The density profile was observed to be triangularly shaped at times. The profile was also observed to be trapezoidally shaped as shown in Fig. 5.1 and often times this trapezoidal shape would have one or more density spikes within the profile. On each shot, the critical power was always calculated using the maximum peak density value measured. In this manner the ratio of P/P_c represents the largest possible ratio. For these measurements the laser power on target varied from ∼3-6.3 TW and peak value of the plasma density varied from ∼1x10^{19}-2.4x10^{19} cm^{-3}. The average peak plasma density value used in this charge measurement was 1.5x10^{19} cm^{-3}.

For both the He:N_2 and He:CH_4 gas mixtures the measured charge above 3 MeV was found to vary between 20-50 pC at a $P/P_c \sim 2$. For the He:N_2 gas mixture a similar amount of charge is measured for both the 90:10 and 95:05 gas mixtures over the overlapping ranges of P/P_c. As the ratio of P/P_c was increased the amount of accelerated charge observed from the 90:10 He:N_2 and 95:05 He:CH_4 gas mixture was found to increase. The increase in observed charge at larger values of P/P_c is thought to be caused by two main effects. First, for a fixed density, as the ratio P/P_c is increased a larger amplitude wake will be driven creating a larger volume over which the trapping condition can be satisfied. This may enable a larger amount of charge to be trapped. Secondly, as the amount of power is increased, the volume over which the laser becomes intense enough to ionize N^{6-7+} and inject electrons becomes larger, again possibly leading to more charge being trapped. In the 95:05 He:CH_4 gas mixture as the ratio of P/P_c was

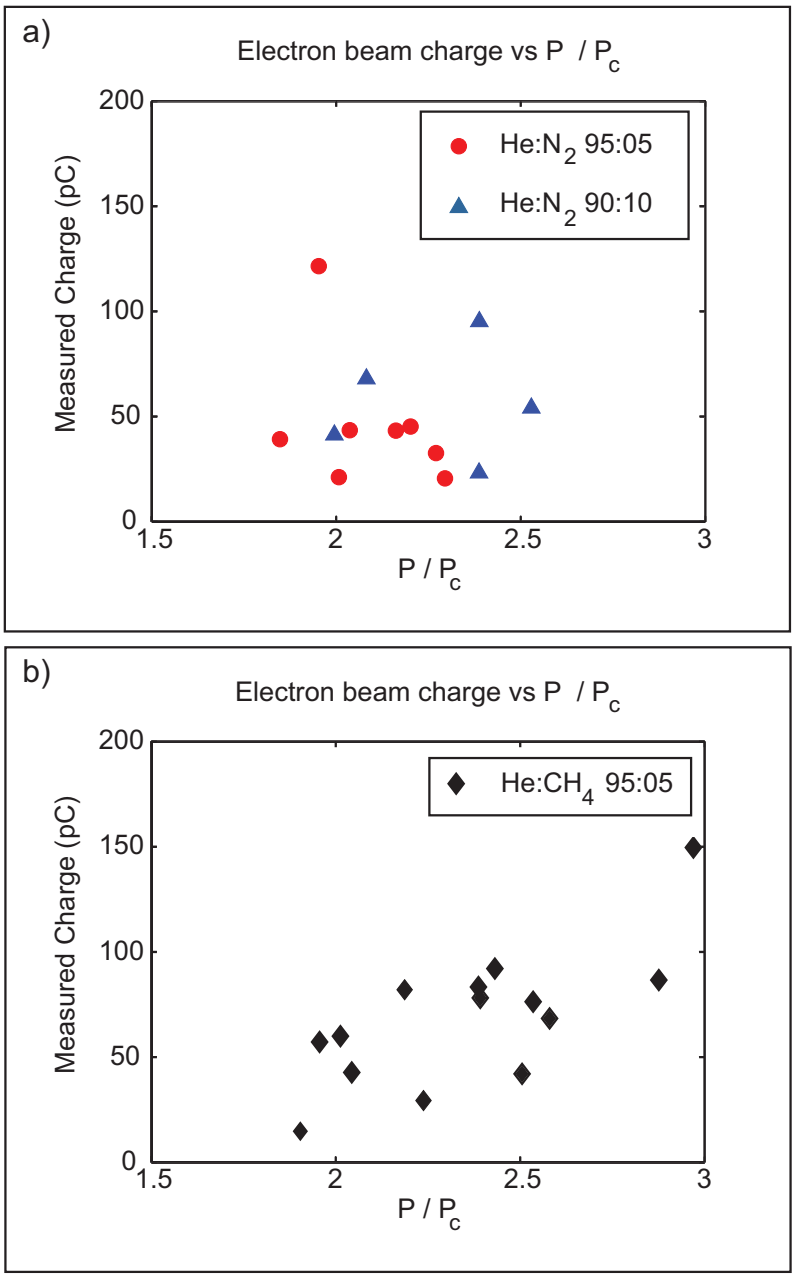

Figure 5.11: The measured charge above ~3 MeV vs P/P_c. a) The blue triangles and red circles correspond to the charge measured using 90:10 and 95:05 He:N_2 gas mixtures respectively. b) The charge measured from the 95:05 He:CH_4 gas mixture.

increased the amount of charge was found to increase to ∼100-150 pC at a P/P_c of nearly 3. In both gas mixtures the magnitude of the accelerated charge was observed to fluctuate by ∼100 % for similar values of P/P_c. This fluctuation in charge may be related to the amount of charge being trapping into multiple periods of the wakefield. The amount of charge trapped and retained within each period of the wake depends on many factors including the value of the plasma density, the plasma density profile, the laser pulse width and magnitude and the laser and wake evolution.

After these measurements were made, the experimental setup was changed to that shown in Fig. 4.11. A dipole magnet with a .285 T field was used to deflect electrons with energies lower than ∼14 MeV into a 3 mm tungsten beam dump. This beam dump stopped these lower energy electrons from striking the ICT. The ICT then measured the charge of electrons with energies above 14 MeV that passed cleanly through the ICT. The charge measured above ∼14 MeV vs the ratio of P/P_c from the 90:10 He:N_2 gas mixture is shown in Fig. 5.12. By deflecting the lower energy electrons, it was thought that a more accurate and consistent measurement of accelerated charge could be made. Figure 5.12 indicates that despite this effort the amount of charge still fluctuates by ∼100 % or more for similar values of P/P_c. The large fluctuation in charge for similar values of P/P_c might indicate there is a 'threshold' in the ratio of P/P_c where very rapidly the wake amplitude starts to grow, and in turn the amount of trapped and accelerated charge increases quickly. In addition to wake amplitude, the trapping of electrons also depends on the phase or location within the wake at which injection takes place. Therefore the threshold ratio of P/P_c at which large amounts of electrons begin to be trapped could also be indicating a sort of resonance between injection location (i.e. pulse width) and plasma density. Additionally fluctuations in the plasma density profile not only effect the trapping

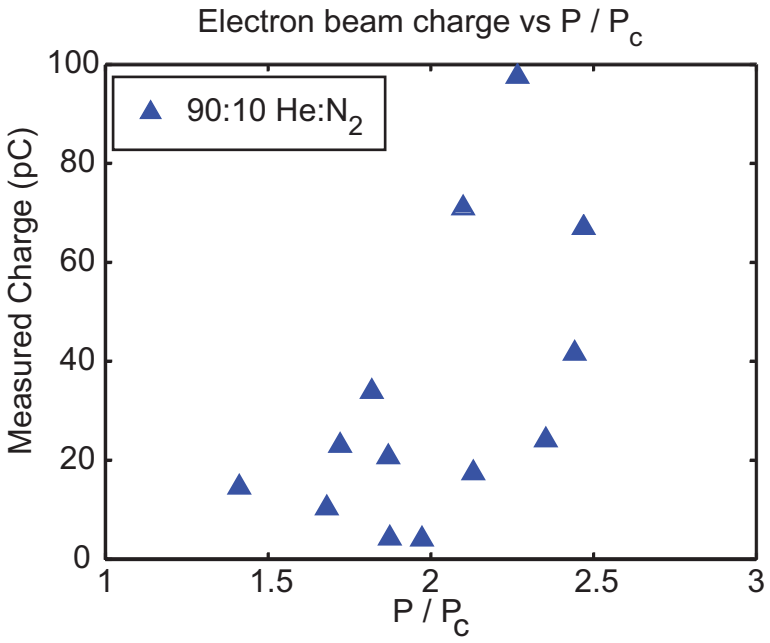

Figure 5.12: The measured charge above ∼14 MeV vs P/P_c using 90:10 gas mixture. Here the ratio of P/P_c has been calculated using the peak measured density.

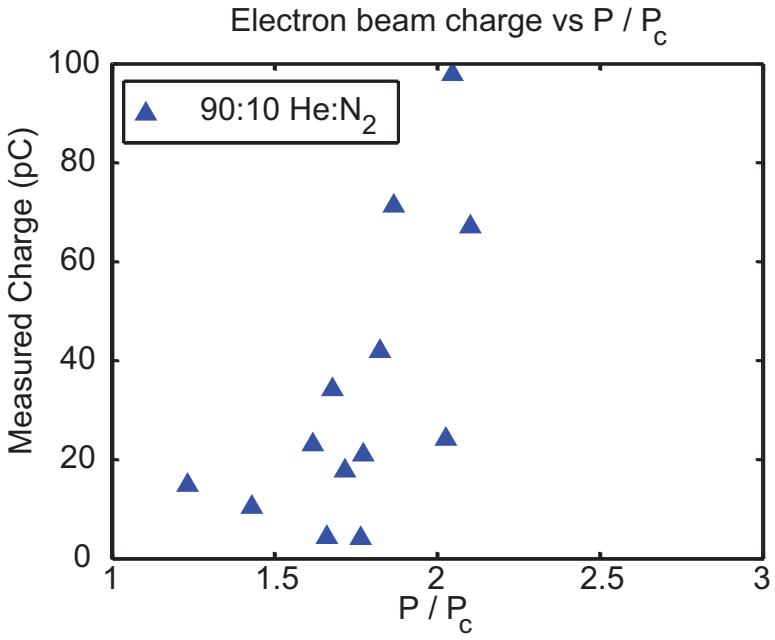

Figure 5.13: The measured charge above ∼14 MeV vs P/P_c using 90:10 gas mixture. Here the ratio of P/P_c has been calculated using the average plasma density of the central ∼700 μm of the plasma profile.

of electrons, but also hinder making an accurate assessment of the critical power for self-focusing. For example, for a triangularly shaped density profile, what density value should be used for to calculate P_c? If instead of the peak density value, an average density over the central ∼700 μm of the density profile is used, the measured charge above ∼14 MeV vs P/P_c can be re-plotted and is shown in Fig. 5.13. Using the average plasma density, the amount of accelerated charge is still found to rapidly increase with increasing values of P/P_c and the amount of charge is still observed fluctuate by ∼100 % or more. Figures 5.13 and 5.12 both indicate that the charge above 14 MeV increases rapidly to ∼100 pC as the ratio of P/P_c is increased in the 90:10 He:N_2 gas mixture. These figures also show that due to the varying plasma density profiles, there is some uncertainty in the

absolute value of P/P_c. Using the average plasma density, accelerated charge was observed at a P/P_c as low as ∼1.2. A gas cell with a flatter, more reproducible profile may aid in making a more accurate measurement of P_c.

In conclusion experimental evidence for the tunneling ionization injection and subsequent trapping of electrons into laser produced wakefields has been presented. The spectral shape, relative amount of charge and beam divergence measured are in good agreement with that from simulations. A detailed description of the laser, wake and electron trapping evolution was presented from data taken from 3-D OSIRIS simulations. This simulation detailed how continuous ionization injection and trapping is eventually inhibited by the changing plasma density profile and subsequent beam loading of the wake. In plasmas produced from 95:05 He:N_2 and 95:05 He:CH_4 gas mixtures it was shown that the spectral shape can be varied from a quasi-continuous to an energy spread of $\sim$ 12% by varying the density, pulse width and in turn the ratio of P/P_c. It was shown that electrons could still be trapped and accelerated via ionization injection as the plasma density was lowered to 8.5x10^{18} cm^{-3}. Here electrons with energies up to ∼110 MeV could be reached using $\sim$ 6 TW of laser power. The amount of accelerated charge injected and trapped from the 90:10 He:N_2 and 95:05 He:N_2 and He:CH_4 gas mixtures was presented. From all of the gas mixtures, tunneling ionization injection was found to create electron beams with 20-100 pC of charge at ratios of P/P_c of ∼2-3. Additionally, it was shown in simulations that by limiting the injection volume, it may be possible to use tunneling ionization injection to create electron beams with less than 1 mrad divergence. In comparison to self-trapping, tunneling ionization injection was shown to require a lower laser intensity to trap electrons, and could be a useful mechanism for injecting electrons into lower density wakefields.

CHAPTER 6

Conclusions

In this dissertation the injection of electrons via tunneling ionization into a laser wakefield accelerator has for the first time been studied and demonstrated. It has been shown, that the large step in the ionization potential of a gas between successive ionization states can be matched to the laser amplitude profile and to the plasma density, such that electrons from the higher ionized state can be injected directly into a LWFA. In this work, gas mixtures comprised of predominately helium with either a small addition of nitrogen or methane gas were used. Near the peak of the laser pulse amplitude, electrons from either N^{6-7+} or C^{5-6+} were created and injected directed into the wakefield which was supported from the electrons of helium and the lower ionization states of either nitrogen or methane. Using the helium nitrogen gas mixture, the observed intensity threshold for the injection, trapping and acceleration of electrons was found to correspond closely to the intensity required to ionize N^{6+}. This sharp onset in the acceleration of electrons at the intensity required to ionize and inject the 6th electron from nitrogen strongly suggests that mechanism of injection is indeed tunneling ionization. Furthermore, the observed broad band electron beam spectra and divergence are in good agreement with 3-D particle in cell code simulations which include the ionization injection process using the ADK model of ionization.

Experiments have shown that using tunneling ionization as an injection mechanism, electrons can be trapped and accelerated using roughly four times less laser

power than that required to self-trap electrons. A fully 3-D Hamiltonian based description of the laser and wakefield was used to find necessary potential difference an electron must experience for trapping to occur. Using the 3-D scaling laws for the LWFA in the blowout regime, it was found that injecting electrons directly into the wakefield significantly increases the potential difference or the amount of energy available to the electron to become trapped. In comparison to self-trapping, this increase in available potential can in turn be used to lower the absolute wake amplitude necessary for trapping to occur. Lower amplitude wakes can be driven with lower laser powers and this model agrees with the experimental observation of accelerated electrons using laser powers far below those required for the self-trapping of electrons.

The reduction in the required laser power to trap and accelerate electrons which have been injected via ionization, could be used to improve the overall efficiency of a LWFA. Additionally the injection and trapping of electrons into wakefields with reduced amplitudes can be used to push laser wakefield accelerators to lower plasma densities in order to reach higher accelerated energies. An advantage of ionization injection is that it can be utilized in conjunction with the self-guiding of the laser pulse in a straight forward manner. Recently the self-guiding and ionization injection concepts were combined to inject electrons at a plasma density of $1.5\text{x}10^{18}$ cm^{-3}, which is the lowest density that electrons have been injected into a LWFA. At this density the laser pulse was intense enough to drive a sufficiently strong wake to remain self-guided, but not intense enough to drive a large enough wake for self-trapping to occur. As a result of injecting electrons via tunneling ionization into a low density LWFA, electrons were able to be accelerated to a peak energy of $\sim$1.45 GeV. To date, this is the highest electron energy that has been reached using a LWFA [53].

Experimental results presented in this dissertation show that the electron spectrum created as a result of ionization injection can be quite varied with energy spreads ranging from continuous down to $\sim 12\%$. The continuous energy spread observed in many electron spectra is thought to be from the continuous injection and trapping of electrons which occurs within the plasma. 3-D OSIRIS simulations indicate that some of the variation in the electron spectrum could be due to the fact that the spectrum contains components from multiple periods of the wakefield. Additionally the simulations show that the evolution of the wake, laser pulse and plasma density profile can all effect the final electron energy spectrum. Simulations also suggest that for concentrations of 10% nitrogen to 90% helium, the number of trapped electrons from N^{6-7+} can beam load the wake and modify the electron energy spectrum. Furthermore the model developed from the LWFA 3-D blowout scaling laws indicates that the injection location within the wake can change the energy gain by $\sim$50%.

There is still much work to be done with the ionization injection mechanism in order to optimize the accelerated electron beam properties. In particular, the large energy spreads are unsuitable for almost all electron beam applications. Currently, efforts are being made to reduce the energy spread of the electron beam created via ionization injection by implementing a two stage accelerator. The first short stage, would be comprised of a gas mixture suitable for ionization injection. Here electrons would be injected and trapped, but only over a short distance, thus limiting the energy spread of the electron beam. The laser, wakefield and trapped electrons would then transition to a much longer stage, filled with a pure helium or hydrogen gas where the injection of electrons would be terminated, but the acceleration would continue.

It is also thought that the ionization injection can lead to accelerated electron

beams with lower divergences in the future. Electron beams with low divergences and emittances are necessary to achieve a high fluence desirable for most applications. In this work electron beams with ∼3-10 miliradian divergences have been observed. As previously discussed, it is thought that the beam divergence could be reduced if the laser pulse width is reduced or if the pulse profile is tailored such that field of the laser does not overlap the region over which electron are accelerated within the wakefield. Additionally it is thought the divergence of the electron beam could be further improved if the ionization volume of injected electrons has a very small transverse extent. It is believed that the closer electrons can be ionized to the axis of the wakefield, the smaller the betatron oscillations will be, and as a consequence less transverse momentum will be gained. Due to being created via ionization, electrons will retain some transverse momentum imparted from the field of the laser. It is believed that when the injection process is optimized, the small amount of transverse momentum gained from ionization (500 KeV) will be small, compared to the transverse momentum of self-trapped electrons which must cross the sheath and be injected from outside of the wakefield.

Initial measurements of the electron beam charge indicate that 20-100 pC of charge can be consistently trapped and accelerated using both the helium nitrogen and helium methane gas mixtures at a ratio of $P/P_c \approx 2$. In these measurements, at similar ratios of P/P_c the amount of charge was observed to fluctuate by over $\sim 100\%$. One should be able to reduce the fluctuation in the amount of charge trapped using ionization injection by improving the reproducibility of the laser as well as the gas source target.

In addition to optimizing the properties of electron beams created through ionization injection, there are a few areas of research within the field of laser

wakefield acceleration which might be further explored using ionization injection. One topic of interest is to see if ionization injection can allow the trapping of electrons into low amplitude linear electron waves. While an external source of laser guiding must be used, injecting and accelerating electrons within the linear regime is of considerable interest. Additionally ionization injection might be used to trap enough charge into a wakefield as to observe beam loading effects. While beam loading will be difficult to study, as it appears that ionization injection traps electrons into multiple periods of the wake, it is still an interesting and open field of experimental study.

References

[1] L. Evens and P. Byrant. LHC machine. *Journal of Instrumentation*, 3:SO8001, 2008.

[2] P. Emma. First lasing of the LCLS x-ray fel at 1.5 angstroms. In *Proceedings of the 2009 Particle Accelerator Conf.* IEEE, in the press.

[3] T. Tajima and J. M. Dawson. Laser electron accelerator. *Phys. Rev. Lett.*, 43(4):267–270, Jul 1979.

[4] V. Malka, J. Faure, and Y. A. Gauduel. Ultra-short electron beams based spatio-temporal radiation biology and radiotherapy. *Mutation Research Reviews in Mutation Research*, 704(1-3):142–151, 2010.

[5] D. A. G. Deacon, L. R. Elias, J. M. J. Madey, G. J. Ramian, H. A. Schwettman, and T. I. Smith. First operation of a free-electron laser. *Phys. Rev. Lett.*, 38(16):892–894, Apr 1977.

[6] Pisin Chen, J. M. Dawson, Robert W. Huff, and T. Katsouleas. Acceleration of electrons by the interaction of a bunched electron beam with a plasma. *Phys. Rev. Lett.*, 54(7):693–696, Feb 1985.

[7] M. Fuchs et al. Laser-driven soft-x-ray undulator source. *Nat. Phys.*, 5:826–829, Sept 2009.

[8] C. Joshi et al. Ultrahigh gradient particle acceleration by intense laser-driven plasma density waves. *Nature*, 311:525–529, Oct. 1984.

[9] C. E. Clayton, K. A. Marsh, A. Dyson, M. Everett, A. Lal, W. P. Leemans, R. Williams, and C. Joshi. Ultrahigh-gradient acceleration of injected electrons by laser-excited relativistic electron plasma waves. *Phys. Rev. Lett.*, 70(1):37–40, Jan 1993.

[10] M. Everett et al. Trapped electron acceleration by a laser-driven relativistic plasma wave. *Nature*, 368:527–529, Apr. 1994.

[11] J. B. Rosenzweig, D. B. Cline, B. Cole, H. Figueroa, W. Gai, R. Konecny, J. Norem, P. Schoessow, and J. Simpson. Experimental observation of plasma wake-field acceleration. *Phys. Rev. Lett.*, 61(1):98, Jul 1988.

[12] I. Blumenfeld et al. Energy doubling of 42 gev electrons in a meter-scale plasma wakefield accelerator. *Nature*, 445(7129):741–744, Feb 2007.

[13] D. Strickland and G. Mourou. Compression of amplified chirped optical pulses. *Optics Communications*, 56(3):219–221, Dec 1985.

[14] C. A. Coverdale, C. B. Darrow, C. D. Decker, W. B. Mori, K-C. Tzeng, K. A. Marsh, C. E. Clayton, and C. Joshi. Propagation of intense subpicosecond laser pulses through underdense plasmas. *Phys. Rev. Lett.*, 74(23):4659–4662, Jun 1995.

[15] A. Modena et al. Electron acceleration from the breaking of relativistic plasma waves. *Nature*, 377:606–608, Oct 2002.

[16] C. Joshi, T. Tajima, J. M. Dawson, H. A. Baldis, and N. A. Ebrahim. Forward raman instability and electron acceleration. *Phys. Rev. Lett.*, 47(18):1285–1288, Nov 1981.

[17] C. Joshi and T. Katsouleas. Plasma accelerators at the energy frontier and on tabletops. *Physics Today*, 56(6):47–53, 2003.

[18] A. Butler, D. J. Spence, and S. M. Hooker. Guiding of high-intensity laser pulses with a hydrogen-filled capillary discharge waveguide. *Phys. Rev. Lett.*, 89(18):185003, Oct 2002.

[19] W. Lu, C. Huang, M. Zhou, W. B. Mori, and T. Katsouleas. Nonlinear theory for relativistic plasma wakefields in the blowout regime. *Phys. Rev. Lett.*, 96(16):165002, Apr 2006.

[20] J. E. Ralph et al. Self-guiding of ultrashort, relativistically intense laser pulses through underdense plasmas in the blowout regime. *Phys. Rev. Lett.*, 102(175003):1–4, 2009.

[21] J. E. Ralph, C. E. Clayton, F. Albert, B. B. Pollock, S. F. Martins, A. E. Pak, K. A. Marsh, J. L. Shaw, A. Till, J. P. Palastro, W. Lu, S. H. Glenzer, L. O. Silva, W. B. Mori, C. Joshi, and D. H. Froula. Laser wakefield acceleration at reduced density in the self-guided regime. volume 17, page 056709. AIP, 2010.

[22] R.L. Williams, C.E. Clayton, C. Joshi, T. Katsouleas, and W.B. Mori. Studies of relativistic wave-particle interactions in plasma-based collective accelerators. *Laser and Particle Beams*, 8(3):427–49, 1990 1990.

[23] J. Faure, Y. Glinec, A. Pukhov, S. Kisetev, S. Gordienko, E. Lefebvre, J.-P. Rousseau, F. Burgy, and V. Malka. A laser-plasma accelerator producing monoenergetic electron beams. *Nature*, 431(7008):541–4, 30 September 2004.

[24] C.G.R. Geddes, C. Toths, J. van Tilborg, E. Esarey, C.B. Schroeder, D. Bruhwiler, C. Nieter, J. Cary, and W.P. Leemans. High-quality electron beams from a laser wakefield accelerator using plasma-channel guiding. *Nature*, 431(7008):538–41, 30 September 2004.

[25] S.P.D. Mangles, C.D. Murphy, Z. Najmudin, A.G.R. Thomas, J.L. Collier, A.E. Dangor, E.J. Divall, P.S. Foster, J.G. Gallacher, C.J. Hooker, D.A. Jaroszynsk, A.J. Langley, W.B. Mori, P.A. Norreys, F.S. Tsung, R. Viskup, B.R. Walton, and K. Krushelnick. Monoenergetic beams of relativistic electrons from intense laser-plasma interactions. *Nature*, 431(7008):535–8, 30 September 2004.

[26] F.S. Tsung, W. Lu, M. Tzoufras, W.B. Mori, C. Joshi, J.M. Vieira, L.O. Silva, and R.A. Fonseca. Simulation of monoenergetic electron generation via laser wakefield accelerators for 5-25 TW lasers. *Physics of Plasmas*, 13(5):56708–1–12, May 2006.

[27] V. Malka, S. Fritzler, E. Lefebvre, M.-M. Aleonard, F. Burgy, J.-P. Chambaret, J.-F. Chemin, K. Krushelnick, G. Malka, S.P.D. Mangles, Z. Najmudin, M. Pittman, J.-P. Rousseau, J.-N. Scheurer, B. Walton, and A.E. Dangor. Electron acceleration by a wakefield forced by an intense ultrashort laser pulse. *Science*, 298(5598):1596–600, 22 November 2002.

[28] W. Lu et al. Generating multi-gev electron bunches using single stage laser wakefield acceleration in a 3d nonlinear regime. *Phys. Rev. STAB*, 10(061301):1–12, 2007.

[29] J. Osterhoff, A. Popp, Z. Major, B. Marx, T.P. Rowlands-Rees, M. Fuchs, M. Geissler, R. Ho uml rlein, B. Hidding, S. Becker, E.A. Peralta, U. Schramm, F. Gruner, D. Habs, F. Krausz, S.M. Hooker, and S. Karsch. Generation of stable, low-divergence electron beams by laser-wakefield acceleration in a steady-state-flow gas cell. *Physical Review Letters*, 101(8):085002–1–4, 22 August 2008.

[30] D. H. Froula, C. E. Clayton, T. Döppner, K. A. Marsh, C. P. J. Barty, L. Divol, R. A. Fonseca, S. H. Glenzer, C. Joshi, W. Lu, S. F. Martins, P. Michel, W. B. Mori, J. P. Palastro, B. B. Pollock, A. Pak, J. E. Ralph, J. S. Ross, C. W. Siders, L. O. Silva, and T. Wang. Measurements of the critical power for self-injection of electrons in a laser wakefield accelerator. *Phys. Rev. Lett.*, 103(21):215006, Nov 2009.

[31] S. Kneip, S. R. Nagel, S. F. Martins, S. P. D. Mangles, C. Bellei, O. Chekhlov, R. J. Clarke, N. Delerue, E. J. Divall, G. Doucas, K. Ertel, F. Fiuza, R. Fonseca, P. Foster, S. J. Hawkes, C. J. Hooker, K. Krushelnick, W. B. Mori,

C. A. J. Palmer, K. Ta Phuoc, P. P. Rajeev, J. Schreiber, M. J. V. Streeter, D. Urner, J. Vieira, L. O. Silva, and Z. Najmudin. Near-gev acceleration of electrons by a nonlinear plasma wave driven by a self-guided laser pulse. *Phys. Rev. Lett.*, 103(3):035002, Jul 2009.

[32] E. Esarey et al. *Phys. Rev. Lett.*, 76:2073, 1997.

[33] J. Faure et al. *Nature*, 444:737, 2006.

[34] Jerome Faure, Clement Rechatin, Ahmed Ben-Ismail, Jaeku Lim, Xavier Davoine, Erik Lefebvre, and Victor Malka. Physics of colliding laser pulses in underdense plasmas. *Comptes Rendus Physique*, 10(2-3):148–158, 2009.

[35] S. Bulanov, N. Naumova, F. Pegoraro, and J. Sakai. Particle injection into the wave acceleration phase due to nonlinear wake wave breaking. *Phys. Rev. E*, 58(5):R5257–R5260, Nov 1998.

[36] C. G. R. Geddes, K. Nakamura, G. R. Plateau, Cs. Toth, E. Cormier-Michel, E. Esarey, C. B. Schroeder, J. R. Cary, and W. P. Leemans. Plasma-density-gradient injection of low absolute-momentum-spread electron bunches. *Phys. Rev. Lett.*, 100(21):215004, May 2008.

[37] H. Suk, N. Barov, J. B. Rosenzweig, and E. Esarey. Plasma electron trapping and acceleration in a plasma wake field using a density transition. *Phys. Rev. Lett.*, 86(6):1011–1014, Feb 2001.

[38] T.-Y. Chien, C.-L. Chang, C.-H. Lee, J.-Y. Lin, J. Wang, and S.-Y. Chen. Spatially localized self-injection of electrons in a self-modulated laser-wakefield accelerator by using a laser-induced transient density ramp. *Phys. Rev. Lett.*, 94(11):115003, Mar 2005.

[39] E. Oz et al. Ionization-induced electron trapping in ultrarelativistic plasma wakes. *Phys. Rev. Lett.*, 98(084801):1–4, 2007.

[40] T. P. Rowlands-Rees et al. *Phys. Rev. Lett.*, 100(10):105005, 2008.

[41] T. W. B. Kibble. Refraction of electron beams by intense electromagnetic waves. *Phys. Rev. Lett.*, 16(23):1054–1056, june 1966.

[42] Francis F Chen. Introduction to plasma physics and controlled fusion, 1984.

[43] Brice Quesnel and Patrick Mora. Theory and simulation of the interaction of ultraintense laser pulses with electrons in vacuum. *Phys. Rev. E*, 58(3):3719–3732, Sep 1998.

[44] P. Sprangle, E. Esarey, A. Ting, and G. Joyce. Laser wakefield acceleration and relativistic optical guiding. *Applied Physics Letters*, 53(22):2146–2148, 1988.

[45] V. I. Berezhiani and I. G. Murusidze. Relativistic wake-field generation by an intense laser pulse in a plasma. *Physics Letters A*, 148(6-7):338 – 340, 1990.

[46] P. Sprangle, E. Esarey, and A. Ting. Nonlinear interaction of intense laser pulses in plasmas. *Phys. Rev. A*, 41(8):4463–4469, Apr 1990.

[47] Guo-Zheng Sun et al. Self-focusing of short intense laser pulses in plasmas. *Phys. Fluid*, 30(2):526–532, 1987.

[48] S. C. Wilks, J. M. Dawson, and W. B. Mori. Frequency up-conversion of electromagnetic radiation with use of an overdense plasma. *Phys. Rev. Lett.*, 61(3):337–340, Jul 1988.

[49] E. Esarey et al. Frequency shifts induced in laser pulses by plasama waves. *Phys. Rev. A*, 42(6):3526, 1990.

[50] J. Faure, Y. Glinec, J. J. Santos, F. Ewald, J.-P. Rousseau, S. Kiselev, A. Pukhov, T. Hosokai, and V. Malka. Observation of laser-pulse shortening in nonlinear plasma waves. *Phys. Rev. Lett.*, 95(20):205003, Nov 2005.

[51] F. S. Tsung et al. Simulation of monoenergetic electron generation via laser wakefield accelerators for 5-25 tw lasers. *Phys. of Plasmas*, 13(5):056708, 2006.

[52] C. D. Decker, W. B. Mori, K.-C. Tzeng, and T. Katsouleas. The evolution of ultra-intense, short-pulse lasers in underdense plasmas. *Physics of Plasmas*, 3(5):2047–2056, 1996.

[53] C. Clayton et al. Self-guided laser wakefield acceleration beyond 1 GeVusing ionization-induced injection. *Accepted to Phys. Rev. Lett.*, June 2010.

[54] A. Pak, K. A. Marsh, S. F. Martins, W. Lu, W. B. Mori, and C. Joshi. Injection and trapping of tunnel-ionized electrons into laser-produced wakes. *Phys. Rev. Lett.*, 104(2):025003, Jan 2010.

[55] I. Kostyukov, A. Pukhov, and S. Kiselev. Phenomenological theory of laser-plasma interaction in "bubble" regime. *Physics of Plasmas*, 11(11):5256–5264, 2004.

[56] S. Kalmykov, S. A. Yi, V. Khudik, and G. Shvets. Electron self-injection and trapping into an evolving plasma bubble. *Phys. Rev. Lett.*, 103(13):135004, Sep 2009.

[57] W Mori, W Lu, and J Martins. Conversations about electron trapping in 3-d simulations with non-evolving drivers. 2010.

[58] S.P.D. Mangles et al. Self-guided wakefield experiements diven by peta-watt class ultra-short laser pulses. *IEEE Trans. on Plas. Sci.*, 36(4):1715, 2008.

[59] D. H. Froula, C. E. Clayton, T. Döppner, K. A. Marsh, C. P. J. Barty, L. Divol, R. A. Fonseca, S. H. Glenzer, C. Joshi, W. Lu, S. F. Martins, P. Michel, W. B. Mori, J. P. Palastro, B. B. Pollock, A. Pak, J. E. Ralph, J. S. Ross, C. W. Siders, L. O. Silva, and T. Wang. Measurements of the critical power for self-injection of electrons in a laser wakefield accelerator. *Phys. Rev. Lett.*, 103(21):215006, Nov 2009.

[60] F. S. Tsung et al. Near-gev laser wakefield acceleration of self-injected electrons in a centimeter-scale plasma channel. *Phys. Rev.*, 93(18):1–4, 2004.

[61] Wei Lu. Nonlinear plasma wakefield theory and optimum scaling for laser wakefield acceleration in the blowout regime. *University of California Los Angeles Ph.D. disertation*, pages 26–32, Nov 2006.

[62] M. V. Ammosov, N. B. Delone, and V. P. Krainov. *Sov. Phys. JETP*, 64:1191, 1986.

[63] D. Bauer and P. Mulser. Exact field ionization rates in the barrier-suppression regime from numerical time-dependent schrödinger-equation calculations. *Phys. Rev. A*, 59(1):569–577, Jan 1999.

[64] David L. Bruhwiler, D. A. Dimitrov, John R. Cary, Eric Esarey, Wim Leemans, and Rodolfo E. Giacone. Particle-in-cell simulations of tunneling ionization effects in plasma-based accelerators. *Physics of Plasmas*, 10(5):2022–2030, 2003.

[65] P. B. Corkum, N. H. Burnett, and F. Brunel. Above-threshold ionization in the long-wavelength limit. *Phys. Rev. Lett.*, 62(11):1259–1262, Mar 1989.

[66] F. V. Hartemann, S. N. Fochs, G. P. Le Sage, N. C. Luhmann, J. G. Woodworth, M. D. Perry, Y. J. Chen, and A. K. Kerman. Nonlinear ponderomotive scattering of relativistic electrons by an intense laser field at focus. *Phys. Rev. E*, 51(5):4833–4843, May 1995.

[67] C. I. Moore et al. *Phys. Rev. Lett.*, 82(8):1688, 1999.

[68] A. Maltsev and T. Ditmire. Above threshold ionization in tightly focused, strongly relativistic laser fields. *Phys. Rev. Lett.*, 90(5):053002, Feb 2003.

[69] A. D. DiChiara, I. Ghebregziabher, R. Sauer, J. Waesche, S. Palaniyappan, B. L. Wen, and B. C. Walker. Relativistic mev photoelectrons from the single atom response of argon to a $1019w/cm2$ laser field. *Phys. Rev. Lett.*, 101(17):173002, Oct 2008.

[70] S. Semushin and V. Malka. High density gas jet nozzle design for laser target production. *Review of Scientific Instruments*, 72(7):2961–2965, 2001.

[71] V. Malka, J. Faure, and F. Amiranoff. Characterization of plasmas produced by laser–gas jet interaction. *Physics of Plasmas*, 8(7):3467–3472, 2001.

[72] Mitsuo Takeda, Hideki Ina, and Seiji Kobayashi. Fourier-transform method of fringe-pattern analysis for computer-based topography and interferometry. *J. Opt. Soc. Am.*, 72(1):156–160, 1982.

[73] Kjell Bockasten. Transformation of observed radiances into radial distribution of the emission of a plasma. *Journal of the optical society of america*, 51(9):943–947, 1961.

[74] Milan Kalal and Keith A. Nugent. Abel inversion using fast fourier transforms. *Appl. Opt.*, 27(10):1956–1959, 1988.

[75] G. A. Novikov et al. Large permanent magnet dipole performance. In *Proceedings of the 2001 Particle Accelerator Conf.* IEEE, 2001.

[76] Hermann Wollnik. Optics of charged particles, 1987.

[77] http://www.gmw.com. *Integrating current transfomer user's manual.*

[78] R. A. Fonseca et al. Osiris: A three-dimensional, fully relativistic particle in cell code for modeling plasma based accelerators. In *Lecture Notes in Computer Science 2329*, pages III–342. Heildberg:Springer, 2002.

[79] S. Augst, D. D. Meyerhofer, D. Strickland, and S. L. Chint. Laser ionization of noble gases by coulomb-barrier suppression. *J. Opt. Soc. Am. B*, 8(4):858–867, 1991.

[80] B. M. Penetrante et al. Ionization-induced frequency shifts in intense femtosecond laser pulses. *J. Opt. Soc. Am. B*, 9(11):2032–2040, 1992.

[81] C. E. Clayton, B. E. Blue, E. S. Dodd, C. Joshi, K. A. Marsh, W. B. Mori, S. Wang, P. Catravas, S. Chattopadhyay, E. Esarey, W. P. Leemans, R. Assmann, F. J. Decker, M. J. Hogan, R. Iverson, P. Raimondi, R. H. Siemann, D. Walz, T. Katsouleas, S. Lee, and P. Muggli. Transverse envelope dynamics of a 28.5-gev electron beam in a long plasma. *Phys. Rev. Lett.*, 88(15):154801, Apr 2002.

[82] S.P.D. Mangles et al. Laser-wakefield acceleration of monoenergetic electron beams in the first plasma-wave period. *Phys. Rev. Lett.*, 96:215001–1, 2006.